Ozone depletion, chlorine activation and water vapor observed in Spitsbergen

Dissertation zur Erlangung des Grades
Dr. rer. nat.
der Universität Bremen

vorgelegt von
Ingo Wohltmann
April 2002

Berichte aus dem Institut für Umweltphysik – Band 0
herausgegeben von:

Dr. Georg Heygster
Universität Bremen, FB 1, Institut für Umweltphysik,
Postfach 33 04 40, D-28334 Bremen
URL `http://www.iup.physik.uni-bremen.de`
E-Mail `iupsekr@uni-bremen.de`

Prüfer: Prof. Dr. Klaus Künzi, Prof. Dr. John Burrows

Contents

Used Publications

Parts of this thesis were published in

- Klein, U., Wohltmann, I., Lindner, K. and Künzi, K. F.: Ozone depletion and chlorine activation in the Arctic winter 1999/2000 observed in Ny-Ålesund. *J. Geophys. Res.*, **107**, accepted, 2002.

Abstract

This work discusses measurements of the ground based microwave Radiometer for Atmospheric Measurements (RAM), the retrieval of desired data products and their interpretation. The radiometer is operated at the Arctic station of the Network for the Detection of Stratospheric Change (NDSC) at Ny-Ålesund, Spitsbergen (78.9° N, 11.9° E). It measures water vapor at 22 GHz, ozone at 142 GHz and chlorine monoxide at 204 GHz.

The first part of this work concentrates on the data retrieval. A summary of the most recent status of the retrieval software is given as a reference and to reflect some new additions. A special focus lies on the water vapor retrieval, which proved to be unexpectedly difficult to implement.

The second part deals with the determination of ozone loss rates, chlorine activation and denitrification. A method to determine loss rates from the measurements of the RAM has been developed and improved over the last four years. Here, ozone loss calculations for the winters 1999/2000 and 2000/2001 are presented, accompanied by a comparison to other techniques, a mathematical examination of the method and an error analysis, including the effects of different diabatic heating rates, mixing, the definition of the vortex edge, altitude resolution and other aspects.

Measurements of chlorine monoxide, denitrification and reservoir gases are presented and examined in the context of the current understanding of ozone chemistry. It is shown by model comparisons that the general aspects of chemistry seem to be well understood. It is also pointed that there remain some considerable uncertainties in measurements as well as in the model assumptions.

The third part examines the possibilities of retrieving tropospheric water vapor columns from the measurements of the radiometer. When the tropospheric water vapor bias is measured at two different frequencies, the calculation of the columns is straightforward and an established method. The study here concentrates on the effects of precipitation and clouds and possibilities to correct the occurring errors.

Introduction

Microwave radiometers built in Bremen, Germany, have been measuring stratospheric trace gases for almost a decade now. Looking back, a wealth of measurements and scientific results has resulted from our research activity. First ozone measurements have already been conducted in 1992, and continuous observations began in 1994 in Ny-Ålesund, Spitsbergen (79° N, 12° E). In the following years, more and more instruments have been added. In the moment, ozone profiles, chlorine monoxide profiles, tropospheric water vapor columns and stratospheric water vapor profiles are measured. Ny-Ålesund is part of the primary Arctic station of the Network for the Detection of Stratospheric Change (NDSC), where the instruments are operated in cooperation with the Alfred Wegener Institute of Polar and Marine Research (AWI) in Potsdam, Germany, and the Institute of Environmental Physics (IUP) in Bremen. Main goal of the NDSC is the identification of changes in the ozone layer and the examination of their causes. Therefore, a continuous series of ozone measurements has been recorded at Ny-Ålesund and used to infer ozone depletion. Equally relevant are the measurements of chlorine monoxide, which is an important species in the chemistry of ozone depletion and can be used to test the understanding of the underlying chemical mechanisms. Chlorine monoxide is obtained by only half a dozen of instruments in the Arctic, with very limited spatial and temporal coverage, making observations very valuable. A similar situation exists for water vapor, which is important for the radiation balance in the stratosphere and the trend in ozone depletion.

The story is continued with new radiometers at Bremen (53° N, 8° E), Mérida, Venezuela (8° N, 71° W), and Summit, Greenland (72° N, 38° W). The radiometer in Bremen is measuring ozone at mid latitudes since 1999, while the instrument in Venezuela will be one of the first radiometers measuring trace gases in the tropics and is located in more than 4500 m altitude to reduce the influence of water vapor. The extremely dry location of Summit in the Arctic, situated in more than 3000 m altitude, is ideally suited for the observation of rarely measured species that only show up at high frequencies, where the atmosphere is nearly opaque under humid conditions. For example, the first continuous measurements of N_2O and HNO_3 in the Arctic will be carried out at Summit.

Microwave radiometers measure the thermally induced radiation of atmospheric trace gases and deduce profile information from the pressure broadened form of the emission lines. A great advantage to other instruments is the possibility to measure in the polar night and the high temporal resolution of the measurements. The instruments are also almost independent of weather conditions. Hence, a continuous measurement series for ozone and water vapor and regular observations of chlorine monoxide provide the opportunity of long term trend analyses and continuing observations of Arctic ozone loss.

Purpose of this work is the retrieval and interpretation of the numerous data products of the radiometers, with a special focus on ozone depletion. The determination of anthropogenic ozone depletion has been a key topic in atmospheric sciences in the last decade. This development was initiated in 1985, when Farman et al. discovered a strong ozone deficit in the southern polar region in spring, which was apparently caused by anthropogenic influences. In the nineties, a similar phenomenon could also be observed in the Arctic. In the following, the political and public interest induced by the harmful effects of increasing ultraviolet radiation and the impact of ozone on the climate change catalyzed a tremendous amount of scientific research activity. In an unprecedented event in environmental politics, this led to a worldwide ban on chlorofluorocarbons, which were made responsible for the ozone decline. A detailed outline of the history of ozone depletion is given in the first chapter of this thesis, which leads us to a summary of the contents of this work.

The basic principles of stratospheric physics and chemistry will be explained in the first chapter, while the second introductory chapter contains a description of the instrument and the fundamentals of radiative transfer. The third chapter

deals with the retrieval of desired data products from the measured spectra. A summary of the most recent status of the retrieval software is given as a reference and to reflect some new additions not published until yet. Special attention is given to the new water vapor retrieval, a species that proved to be unexpectedly difficult to implement. Although no validated profiles could be obtained yet, some promising developments are shown. The detailed review of the physical model and of the changes in the retrieval code hopefully will lay the foundation for a successful retrieval in the future. The development of a new retrieval for the ozone radiometer in Bremen and the chlorine monoxide radiometer in Spitsbergen shall also be mentioned here.

The fourth chapter presents calculations of ozone depletion and examines the chemistry of ozone loss. Countless studies have been carried out aiming at a better understanding of ozone depletion over the last few years. Examples are the EASOE (1991/1992) and SESAME (1994/1995) campaigns and especially the American-European joint effort SOLVE/THESEO in the winter 1999/2000, which is presented here in detail. A wide variety of different techniques has been developed to determinate ozone loss rates in the past. Many of them have been employed during the SOLVE/THESEO campaign, giving an excellent opportunity to compare different techniques and to assess their errors. A method for the determination of ozone loss rates from the measurements of the ozone radiometer in Spitsbergen is described and applied to the data from the winters 1999/2000 and 2000/2001. Cumulative losses of 1.2 ± 0.4 ppm and 0.4 ± 0.3 ppm are inferred for the two winters. The agreement between these results and the findings of other methods is shown to be good, considering the large uncertainties of all techniques. Since a detailed error analysis was missing so far for our method, it is conducted in addition to the practical comparison. Effects of altitude resolution, the choice of the observed period, the influence of the vortex edge definition, different heating rates or mixing and principal differences in the several methods are discussed. Furthermore, a mathematical examination of the method is performed, leading to the introduction of a passive profile in the ozone depletion calculations.

The computation of ozone loss rates would not be complete without a physical interpretation of the data. Measurements of chlorine monoxide, reservoir gases, nitrate species and denitrification are shown to develop a chemical scenario for the winter. Results are compared to the SLIMCAT model, which encompasses the current knowledge of stratospheric physics and chemistry (as far as computationally possible), and discrepancies are discussed. Especially, differences in chlorine activation are observed, which are attributed to uncertainties in the denitrification scheme and the formation mechanism for stratospheric clouds in the model. The surprisingly good agreement of the ozone loss rates of the measurements and the model is also examined. It is shown that the general aspects of ozone depletion are qualitatively well understood, but that there remain some quantitative uncer-

tainties. The last chapter examines the possibilities of retrieving water vapor and liquid water columns from the radiometer measurements. Since the radiometers were not explicitly built to measure this quantities, this is a nice addition to the variety of our measurements. The focus here lies on the effects of clouds and precipitation and methods of correcting occurring errors. Finally, the work is concluded with a summary of all results.

In hope for a pleasant reading,
Ingo Wohltmann

1 Physics and Chemistry of the Atmosphere

1.1 Composition of the Atmosphere

The atmosphere of the earth formed long ago from gases escaping from the interior of the earth and the biosphere. It is composed mainly of nitrogen (78.1%), oxygen (20.9%) and some noble gases (0.9%). The remainder consists of several trace gases. The most striking feature of the atmosphere is the sharp drop of pressure with altitude. It can be explained by the hydrostatic equilibrium between gravity and the pressure gradient

$$\partial p/\partial z = -\rho g \tag{1.1}$$

where p is pressure, z is altitude, ρ is the density of air and g is the gravitational acceleration. In regard to the pressure, the ideal gas law states

$$p = \rho RT/m_{\mathrm{mol}} \tag{1.2}$$

where T is the thermodynamic temperature, $R = 8.31\,\mathrm{J\,mol^{-1}\,K^{-1}}$ is the universal gas constant and m_{mol} is the mass of $N_{\mathrm{A}} = 6.022 \times 10^{23}$ molecules. Combination of Equation 1.1 and 1.2 yields the barometric law

$$p(z) = p_0 \exp(-z/H) \tag{1.3}$$

under the assumption that T is constant. p_0 is the reference pressure at sea level, which is usually set to 1013 hPa. The pressure scale height $H = RT/(m_{\mathrm{mol}}g)$ has a value of about 7 km.

The atmosphere can be divided in several layers distinguished by different physical properties, see Figure 1.1. The troposphere is the lowermost layer, marked by a negative vertical temperature gradient due to adiabatic motions, which will be explained below. Most of the weather phenomena take place in the troposphere due to the dynamically imbalanced situation connected with a negative

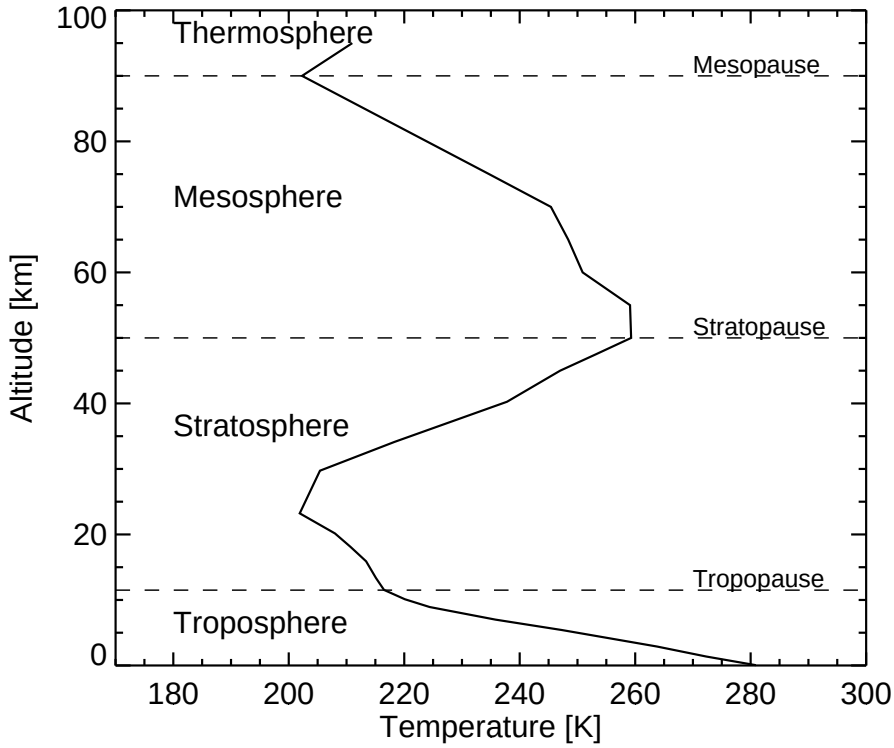

Figure 1.1: Layers of the atmosphere. The temperature profile is typical of a subarctic winter atmosphere.

temperature gradient. The troposphere already contains more than 50% of all air molecules. We will focus on the next layer of the atmosphere, the stratosphere, extending from roughly 8 km to 50 km in the polar winter. The stratosphere is marked by a positive temperature gradient caused by diabatic heating, which leads in turn to a dynamically stable situation with low vertical wind speeds. The stratosphere is dynamically and chemically isolated from the troposphere through the tropopause (defined by the World Meteorological Organization as the altitude where the temperature lapse rate first decreases below 2 K/km in a 2 km altitude range). Further layers are the mesosphere with a negative temperature gradient and the very hot thermosphere. The layers from the troposphere up to the mesosphere form the homosphere, where gases are in thermal equilibrium.

Trace gases are gases which are highly variable in time and space. Although their amounts can be very low, they usually have a great impact on the physics of the atmosphere. Their abundance can be measured in several ways. Number density gives the number of molecules per volume. Volume mixing ratio is the ratio of the number of molecules of the observed species to the number of molecules of

all species. It can be calculated from the number density n of the gas by

$$x = nk_{\mathrm{B}}T/p \tag{1.4}$$

where $k_{\mathrm{B}} = 1.38 \times 10^{-23}$ J/K is Boltzmann's constant. It is often measured in percent, parts per million (ppm) or parts per billion (ppb). Since volume mixing ratios are conserved under movements, they are normally used in most analyses. Finally, the column of a trace gas is given by the vertical integral of the number density. Ozone column is often measured in Dobson Units, where 1 DU is given by 2.69×10^{16} molecules/cm^2, corresponding to an ozone layer of 0.01 mm thickness at sea pressure. Ozone column is important for the amount of ultraviolet radiation reaching the surface of the earth.

1.2 Physics of the Atmosphere

General aspects of the physics of the atmosphere will not be repeated here, because they can be found in numerous text books. Instead, we will concentrate on some concepts used frequently in this thesis.

At first, we will introduce the concept of an air parcel. An air parcel is defined as an entity consisting of ever the same air molecules moving around in the atmosphere. If some property x of the parcel, like its velocity or pressure, is changed locally for an observer moving with the parcel (Lagrangian viewpoint) and the change is given by $\partial x/\partial t$, the change for an observer standing at a fixed position (Eulerian viewpoint) is

$$\frac{\mathrm{D}x}{\mathrm{D}t} = \frac{\partial x}{\partial t} + \frac{u}{a\cos\vartheta}\frac{\partial x}{\partial \varphi} + \frac{v}{a}\frac{\partial x}{\partial \vartheta} + w\frac{\partial x}{\partial z} \tag{1.5}$$

in spherical coordinates. u is the zonal wind here, v is the meridional wind, w is the vertical wind, ϑ is latitude, φ is longitude and a is the radius of the earth. The derivative $\mathrm{D}/\mathrm{D}t$ is called the substantive derivative. Note that by definition, the mixing ratio of an air parcel cannot be changed.

Next, we will establish a useful coordinate system that simplifies the following discussions. It consists of potential temperature instead of altitude and potential vorticity instead of horizontal coordinates. A thermodynamic process without the supply of external heat is called adiabatic. In the stratosphere, most processes can be considered adiabatic on the timescale of a few days. For longer timescales radiative heating has to be considered. Potential temperature is a quantity of an air parcel that remains constant under adiabatic conditions. It is defined as

$$\Theta = T\left(\frac{p_0}{p}\right)^{2/7} \tag{1.6}$$

where p_0 is an arbitrary reference pressure and T and p are temperature and pressure of the air parcel. Θ is the temperature the air parcel would have if it were moved adiabatically to the reference pressure level. The conservation of potential temperature expresses the fact that increasing pressure increases the temperature of an thermally isolated air parcel due to the transformation of work into heat. Since potential temperature normally increases monotonically with altitude and does not vary very rapidly in horizontal direction, it can be used instead of the z coordinate, canceling any vertical adiabatic movements. Surfaces of constant potential temperature are called isentropes. In the lower stratosphere, 25 K potential temperature correspond to about 1 km altitude difference, with the 475 K isentropic level situated around 20 km altitude. On the scale of a few days, air in the stratosphere moves only on isentropic surfaces.

It can be shown that an air parcel that is moved adiabatically and vertically from its original position will continue its movement when the actual vertical temperature decrease is higher than the diabatic temperature decrease (instability against convection) and will be forced back to its original position when the actual temperature decrease is lower than the adiabatic decrease or there is a temperature increase (stability against convection). This explains the dynamic differences between the convective troposphere and the stratosphere.

Potential vorticity is a quantity conserved under adiabatic and reversible conditions and therefore can be used as a tracer for air masses. Its advantage over chemical tracers is the fact that it can be calculated from wind, temperature and pressure, which are easily available for the whole globe. Potential vorticity is the product of the thickness of the isentropes and the curl of the wind field in an absolute coordinate system

$$P = g\frac{\partial\Theta}{\partial p}(\zeta_p + f) \tag{1.7}$$

where g is the gravitational acceleration, $\partial\Theta/\partial p$ is the change of potential temperature with pressure and the last term is the curl of the wind field, also called absolute vorticity. The absolute vorticity is composed of the planetary vorticity f and the relative vorticity ζ_p of the wind field. f is given by $2|\Omega|\sin\vartheta$, where Ω is the angular velocity of the earth. ζ_p is the curl of the wind field relative to the earth surface, which is given by

$$\zeta_p = \frac{1}{a\cos\vartheta}\left(\frac{\partial v}{\partial\varphi} - \frac{\partial(u\cos\vartheta)}{\partial\vartheta}\right) \tag{1.8}$$

The conservation of potential vorticity is connected with the fact that the angular momentum of a rotating air mass must be conserved. If the air mass is stretched in vertical direction, the angular velocity must increase. Potential vorticity is measured in units of PVU $= 10^{-6}\,\mathrm{K\,m^2\,kg^{-1}\,s^{-1}}$. It decreases from the center to the

edges of the low pressure area normally found in the Arctic winter stratosphere (which we will come back to soon) and therefore can be used as a horizontal coordinate. Sometimes, equivalent latitude is used as a coordinate instead of potential vorticity. The equivalent latitude of a potential vorticity contour is defined as the latitude it would have if the enclosed area would be circular and centered over the pole. Equivalent latitude has the advantage of being less influenced by short time fluctuations in the absolute values of potential vorticity.

Finally, let us also have a short look on the equations governing the dynamics. In equilibrium, the horizontal wind is determined by the balance of the Coriolis force with the horizontal pressure gradient

$$fu = -\frac{1}{a}\frac{\partial Z}{\partial \vartheta} \tag{1.9}$$

$$fv = \frac{1}{a\cos\vartheta}\frac{\partial Z}{\partial \varphi} \tag{1.10}$$

where Z is the geopotential altitude of a given pressure surface. Wind blows parallel to the isobares in equilibrium, so that the pressure gradient is conserved, which is called geostrophic wind. Combination of the barometric law and the equations for the horizontal wind yields

$$f\frac{\partial u}{\partial z} = -\frac{R}{aH}\frac{\partial T}{\partial \vartheta} \tag{1.11}$$

$$f\frac{\partial v}{\partial z} = \frac{R}{aH\cos\vartheta}\frac{\partial T}{\partial \varphi} \tag{1.12}$$

These are the equations of the thermal wind, connecting a horizontal temperature gradient with an increase in wind speed with altitude. Finally, the vertical wind is driven by the diabatic heating rate Q, given as the diabatically induced temperature change per time

$$w \sim Q - \frac{\partial T}{\partial t} \tag{1.13}$$

and the conservation of mass is described by the continuity equation

$$\frac{1}{a\cos\vartheta}\left(\frac{\partial u}{\partial \varphi} + \frac{\partial(v\cos\vartheta)}{\partial \vartheta}\right) + \frac{1}{\rho_0}\frac{\partial(\rho_0 w)}{\partial z} = 0 \tag{1.14}$$

with $\rho_0 \sim \exp(-z/H)$ being a mean air density.

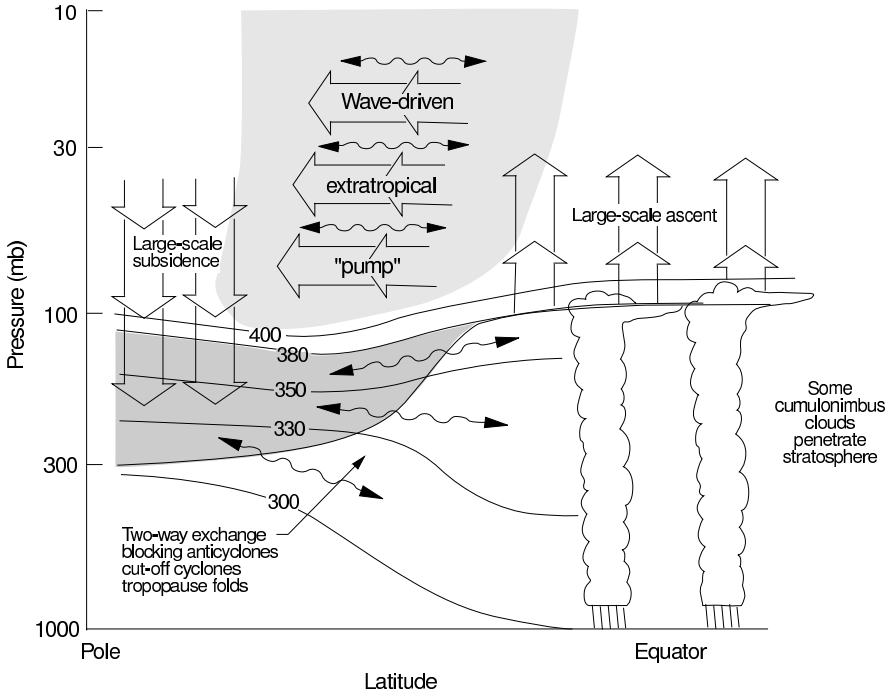

Figure 1.2: Brewer-Dobson circulation. The thin horizontal lines denote isentropic levels. See the text for a detailed explanation. Adapted from [Holton et al., 1995]

1.3 Dynamics of the Stratosphere

Compared to the troposphere, the dynamics of the stratosphere are quite simple. Due to the positive temperature gradient in the stratosphere, convection is not likely. The temperature gradient is caused by the absorption of sunlight by the ozone layer, which is virtually identical in extent with the stratosphere. The vertical movements in the stratosphere, which are very slow (some 10 m per day), are connected to diabatic processes, which in turn are caused by adiabatic movements induced by planetary waves. In the tropics there is an upwelling movement and diabatic heating in the sunlight, while at the poles there is an downwelling movement and diabatic cooling which is especially prominent at the winter pole in the dark polar night. At the sunlit summer pole, movement is virtually nonexistent. For continuity reasons a poleward motion of air develops in the winter hemisphere. This mean meridional movement is called Brewer-Dobson circulation. A sketch of this circulation is given in Figure 1.2. The overturning time for the circulation cell is about 5 years.

We will turn to the horizontal circulation now. The thermal gradient from the equator to the winter pole implies the formation of a low pressure area in the polar

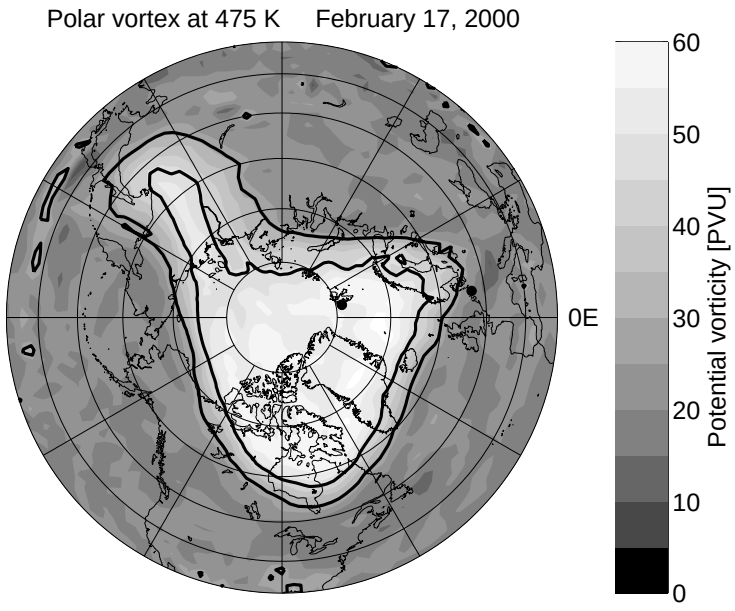

Figure 1.3: Polar vortex at February 17, 2000 at 475 K. Potential vorticity as a tracer shows the distinction between inner and outer vortex air masses. The inner and outer vortex edge is marked by thick lines. The position of Bremen and Ny-Ålesund is marked by dots. A minor warming disturbs the shape and position of the vortex.

region, called the polar vortex. At the vortex edge, a band of strong westerly winds can be found according to the equations of the thermal wind, which is called the polar night jet. In the inner vortex air is virtually isolated from air masses outside the vortex due to the nearly geostrophic air motion at the edge. An example for the appearance of the polar vortex can be found in Figures 1.3 and 1.4.

Interestingly, the Brewer-Dobson circulation is not caused by radiation in the end and it is not even purely diabatic. In the so called surf zone, which is situated between the polar vortex and the tropics, air is turbulently mixed in horizontal direction by planetary waves propagating vertically from the troposphere. The wave breaking of these eddies takes momentum out of the movements in the stratosphere and leads to a deceleration of the westerly winds prominent in these altitudes. In turn this leads to a dynamically and thermodynamically imbalanced situation. Air from the mid latitudes, which is too warm for the poles, is drawn poleward since dynamic forces are not balanced with the Coriolis force anymore. It begins to move downward for continuity reasons, and warms up adiabatically, pushing temperatures above their radiative values and driving the diabatic cooling. Strong downwelling is connected with a weak vortex, high stratospheric temperatures in polar regions and high wave activity and vice versa. Because of the

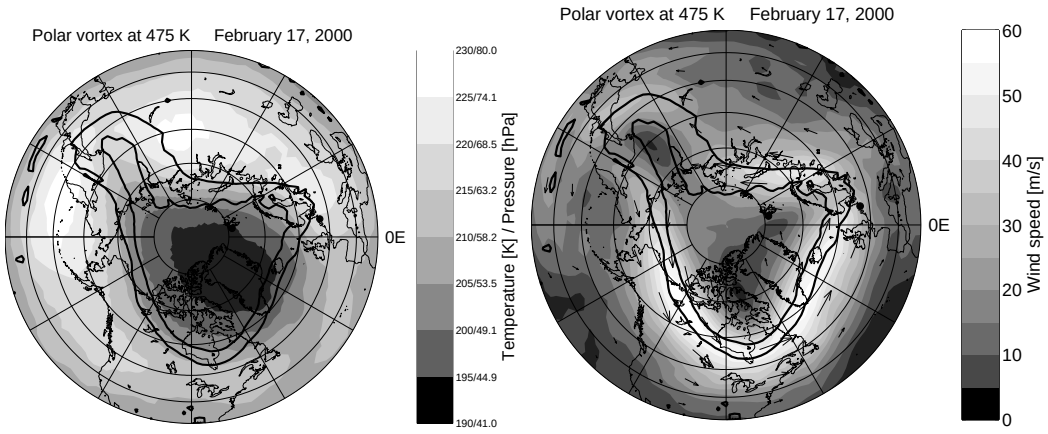

Figure 1.4: Temperature, pressure and wind for the polar vortex at February 17, 2000. Left panel: Temperature and pressure, which has the same isolines at isentropes. Right panel: Wind speed (contours) and wind direction (arrows). The inner and outer vortex edge is marked by thick lines. The position of Bremen and Ny-Ålesund is marked by dots.

distribution of land, sea and mountains that influence wave activity, the Antarctic vortex is usually much more stable than the Arctic vortex.

During particularly strong wave breaking events the momentum taken from the vortex can lead to a breakdown of the wind system. This is called a sudden stratospheric warming, because it is associated with a prominent rise in temperature inside the vortex. Often, the polar vortex can recover from a warming and build up again. But in spring, when sunlight comes back, the vortex splits up or is destroyed entirely.

It is often discussed what processes are causally connected with the formation, stability and duration of the vortex and the corresponding low temperatures, since a stable and cold vortex is connected with high ozone depletion. Suggestions include correlations with the negative radiative forcing due to increasing water vapor and decreasing ozone, wave activity of planetary waves in the troposphere, the Quasi-Biennal Oscillation of the tropical stratosphere winds in east-west direction (QBO), the North-Atlantic Oscillation (NAO) and many more. It seems certain that there is a connection between temperatures and wave activity [Newman et al., 2001], since March vortex temperatures and January wave-induced heat fluxes are highly correlated. Wave activity may be weakened due to coupling to the greenhouse effect, which could obstruct the propagation of tropospheric waves in the stratosphere. In turn, this could lead to a colder and more stable vortex in the future.

1.4 Ozone Chemistry

Although ozone has a mixing ratio of only a few ppm, it is a very important trace gas. The absorption of harmful ultraviolet radiation in the stratosphere makes life on earth just possible, and the stratosphere would not even exist without the diabatic heating of the ozone layer. Ozone forms by the photolysis of molecular oxygen:

$$O_2 + h\nu \rightarrow O + O \qquad \lambda < 242 \text{ nm} \tag{1.15a}$$

$$O + O_2 \overset{M}{\rightarrow} O_3 \tag{1.15b}$$

where M is an air molecule needed for the conservation of momentum. Similarly, it is destroyed by photolysis at greater wavelengths:

$$O_3 + h\nu \rightarrow O_2 + O(^3P) \qquad \lambda < 1100 \text{ nm} \tag{1.16a}$$

$$O_3 + h\nu \rightarrow O_2 + O(^1D) \qquad \lambda < 310 \text{ nm} \tag{1.16b}$$

The excited state $O(^1D)$ can relax to the ground state $O(^3P)$ by collision. Since ozone and oxygen atoms rapidly interchange with each other, the lifetime of ozone itself is short, while only the following reactions produce a net loss in the long-lived odd oxygen, the sum of O and O_3:

$$O + O_3 \rightarrow O_2 + O_2 \tag{1.17a}$$

$$O + O \overset{M}{\rightarrow} O_2 \tag{1.17b}$$

Reactions 1.15 to 1.17 form the Chapman cycle, which was postulated in [Chapman, 1930]. It leads to an equilibrium state for ozone mixing ratios depending on altitude and season. It turned out quickly that the Chapman reactions overestimated the ozone content of the atmosphere. This inconsistency was solved by the discovery of catalytic reactions of the form

$$X + O_3 \rightarrow XO + O_2 \tag{1.18a}$$

$$XO + O \rightarrow X + O_2 \tag{1.18b}$$

$$O + O_3 \rightarrow O_2 + O_2 \tag{1.18c}$$

The radical X can be recycled many times without being destroyed. Thus, even small amounts of the radicals can destroy much larger abundances of ozone due to the catalytic nature of the cycles. The most important catalysators X are OH [Bates and Nicolet, 1950], NO [Crutzen, 1970], Cl [Stolarski and Cicerone, 1974]

and Br [Wofsy et al., 1975]. The most significant natural catalytic cycle in the lower and middle stratosphere is the NO cycle, while the OH cycle is dominating in the upper stratosphere. The main anthropogenic cycle is the Cl cycle.

Source gases for the radicals are N_2O for NO and H_2O and CH_4 for OH. These source gases are mainly of tropospheric origin and are partially photolysed in the stratosphere. N_2O and the sum of H_2O and CH_4 are only minorly changed by the production of the radicals in the lower polar stratosphere and can therefore be used as tracers, which we will take advantage of later. Source gases for Cl and Br are man-made chlorofluorocarbons. Chlorofluorocarbons are decomposed photochemically in the stratosphere and quickly form gases like HCl or HF. Interestingly, fluor plays no role in ozone depletion, since HF is very stable and can also be used as a tracer therefore.

The catalytic cycles are decelerated by reactions of the radicals with themselves, for example:

$$\mathrm{ClO} + \mathrm{NO_2} \xrightarrow{\mathrm{M}} \mathrm{ClONO_2} \tag{1.19a}$$

$$\mathrm{BrO} + \mathrm{NO_2} \xrightarrow{\mathrm{M}} \mathrm{BrONO_2} \tag{1.19b}$$

$$\mathrm{NO_2} + \mathrm{OH} \xrightarrow{\mathrm{M}} \mathrm{HNO_3} \tag{1.19c}$$

$$\mathrm{Cl} + \mathrm{HO_2} \rightarrow \mathrm{HCl} + \mathrm{O_2} \tag{1.19d}$$

$$\mathrm{Cl} + \mathrm{CH_4} \rightarrow \mathrm{HCl} + \mathrm{CH_3} \tag{1.19e}$$

$$\mathrm{ClO} + \mathrm{HO_2} \rightarrow \mathrm{HOCl} + \mathrm{O_2} \tag{1.19f}$$

$$\mathrm{ClO} + \mathrm{NO} \rightarrow \mathrm{Cl} + \mathrm{NO_2} \tag{1.19g}$$

The chemically inactive gases $ClONO_2$ and HCl produced by some of these reactions are called reservoir gases, since they store the ozone destroying radical Cl. Other products that we will show to play a role soon are HNO_3 and the reactive HOCl.

In 1985, Farman et al. discovered a strong ozone deficit in the southern vortex in spring (Figure 1.5, upper panel). It even turned out that this deficit had existed unnoticed since the mid-seventies. The word ozone hole was coined quickly by the press and catalyzed a vivid public discussion about the harmful effects of the ultraviolet radiation normally absorbed by ozone. The strong loss of ozone in the polar spring that causes the Antarctic ozone hole cannot be explained solely by catalytic reactions. It is a matter of fact now, that the ozone is destroyed with the help of heterogenous reactions setting free chlorine from the reservoir gases on the surface of polar stratospheric clouds that form in the polar night.

First suggestions for these mechanisms were already published a year later, for example by Crutzen and Arnold [1986] or Solomon et al. [1986]. They blamed the

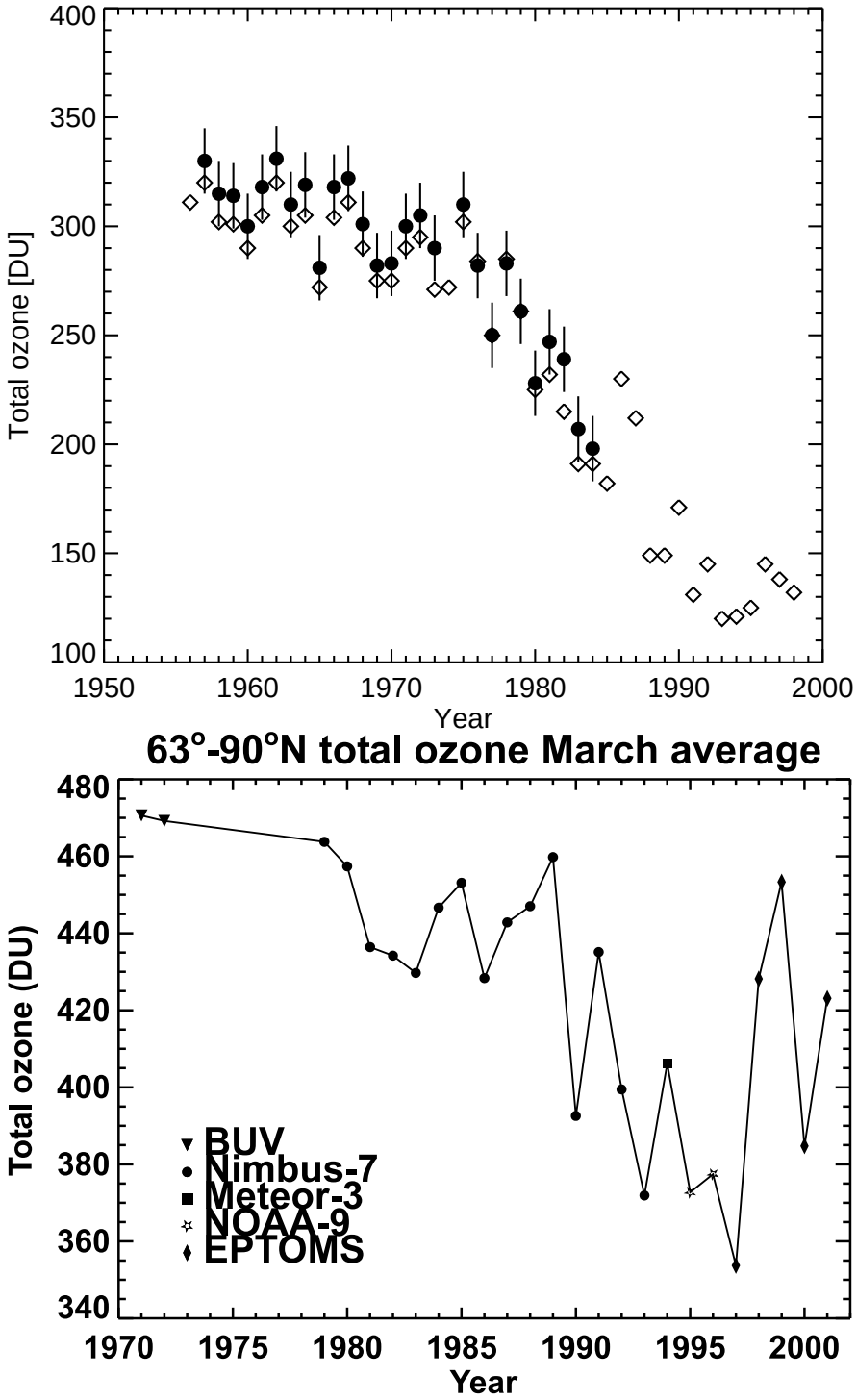

Figure 1.5: Decrease of ozone columns in the last decades. Upper panel: Average total ozone columns for October over Halley Bay, Antarctica. Dots adapted from Farman et al. [1985], diamonds from Jones and Shanklin [1995] and von König [2001]. Lower panel: Average total ozone columns between 63° and 90° N for March from different satellites. Adapted from Newman et al. [1997, 2002].

anthropogenically produced chlorofluorocarbons, which decompose into reservoir gases and further into radicals through heterogenous reactions in the stratosphere, for destroying the ozone layer. Pioneering work in this direction had already been done in the seventies by Molina and Rowland [1974]. The production of chlorofluorocarbons was stopped thereupon by international agreement documented in the Montreal Protocol [1987] and its adjustments. However, due to the slow transport in the stratosphere and the stability of chlorofluorocarbons in the troposphere, chlorine loading is expected to reach its peak just around 2000. Additionally, due to horizontal mixing in the troposphere and the Brewer-Dobson circulation, chlorofluorocarbons and their products are very uniformly distributed in the stratosphere. Ironically, chlorofluorocarbons were used widely in the industry (e. g. in refrigerators or as aerosol propellants), just because they were chemical inert and had no harmful effects on the environment and health. In the nineties, a phenomenon similar to the ozone hole, but less pronounced, could also be observed in the Arctic [Newman et al., 1997]. As can be seen in Figure 1.5, lower panel, the amount of ozone loss is highly dependent on the temperatures and vortex development here and often masked by diabatic descent.

The processes leading to the ozone hole will be discussed in some more detail now. During the polar night, when the polar vortex forms, the influx of air masses from lower latitudes is suppressed, and the lack of sunlight leads to very low temperatures in the lower polar stratosphere. Polar stratospheric clouds (also called PSCs) form here under certain temperature and pressure conditions and mixing ratios of their constituents. Typically, they can be found between 16 to 27 km, where they are generated from water vapor, gaseous nitric acid and the background sulfate aerosol. Nitric acid is mainly produced by reaction 1.19c, so that a deceleration of the natural catalytic cycles is connected with a acceleration in the heterogenous chemistry. At a threshold temperature of approximately 195 K at the 475 K isentropic level, polar stratospheric clouds of Type Ia can form, consisting of solid $HNO_3 \cdot 3H_2O$ (nitric acid trihydrate or NAT) particles with radii of about 1 μm. Solid particles can also be formed by sulphuric acid tetrahydrate (SAT) below 215 K, but these particles play no role in chlorine activation. Type Ib clouds consist of liquid ternary $H_2O/HNO_3/H_2SO_4$ solutions (STS) and form at temperatures of about 191 K. Below 188 K, polar stratospheric clouds of Type II that are composed of ice particles with radii of about 10 μm can exist.

There is still some debate regarding the formation and composition of stratospheric clouds. An overview of the most recent understanding is given by Koop et al. [1997], see also Figure 1.6. A typical formation path is the uptake of HNO_3 by liquid H_2SO_4 particles to form STS particles (path $1 \rightarrow 3 \rightarrow 5$). Ice particles can form subsequently from the STS particles, covered by NAT, SAT or a liquid STS coating (path $7 \rightarrow 9 \rightarrow 10$). Solid NAT particles can normally only form through co-condensed NAT on ice particles (path 14 or $12 \rightarrow 25$). The assumption

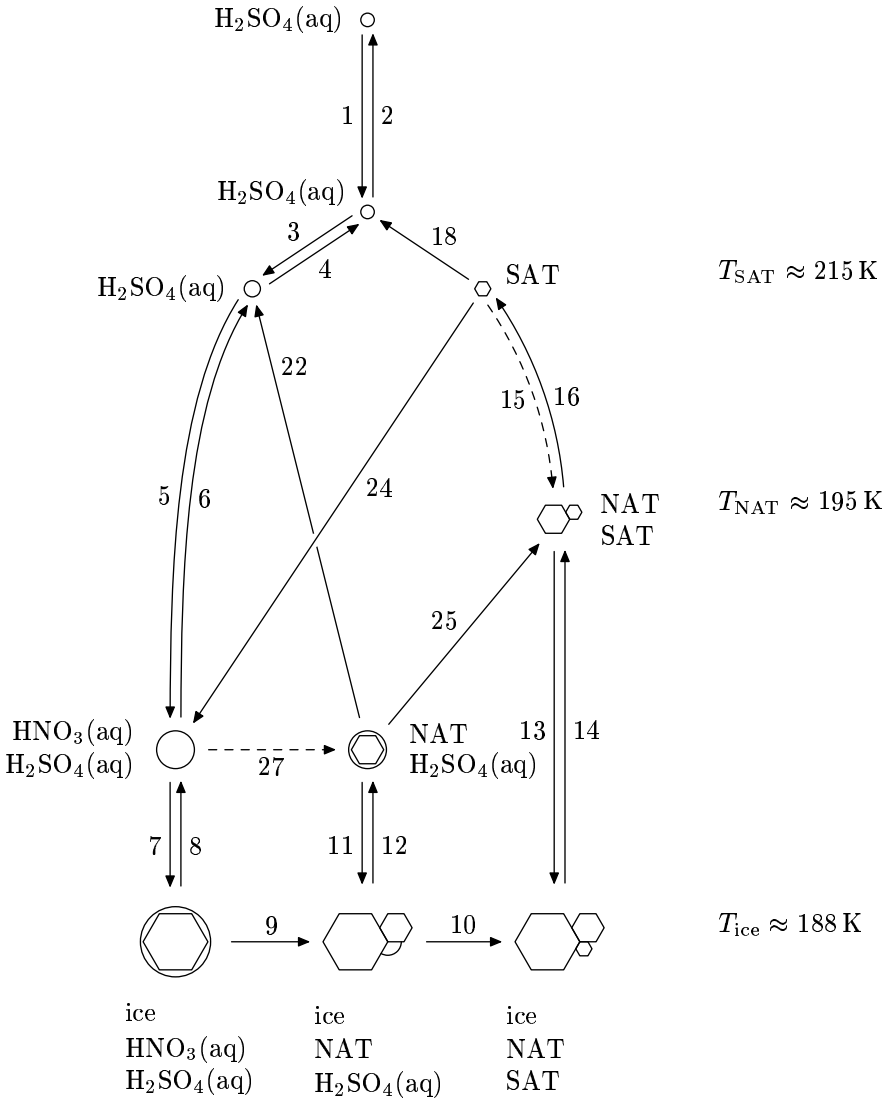

Figure 1.6: Formation of polar stratospheric clouds. Arrows show possible formation paths. Dashed paths are only possible under special circumstances. Adapted from Koop et al. [1997].

that NAT particles can only form below the frost point is unsatisfactory, because the observed extent of NAT clouds is not compatible with this supposition. Thus, some other explanations have been proposed, for example the creation of NAT through $HNO_3 \cdot 2H_2O$ (NAD). A new development is the discovery of so-called NAT rocks [Fahey et al., 2001] with radii of up to 10 μm. The formation of these particles is still not clear, but the may be formed without the help of ice particles. Another point of discussion is the influence of mesoscale clouds forming over mountain ranges in comparison to synoptic clouds. More information can be found for example in [Koop et al., 1997] or [Drdla et al., 2002].

On the surface of the polar stratospheric clouds, several reactions free chlorine and bromine from the reservoir gases:

$$ClONO_2 + HCl \rightarrow Cl_2 + HNO_3 \quad (1.20a)$$
$$ClONO_2 + H_2O \rightarrow HOCl + HNO_3 \quad (1.20b)$$
$$BrONO_2 + H_2O \rightarrow HOBr + HNO_3 \quad (1.20c)$$
$$HOCl + HCl \rightarrow Cl_2 + H_2O \quad (1.20d)$$
$$HOBr + HCl \rightarrow BrCl + H_2O \quad (1.20e)$$
$$N_2O_5 + H_2O \rightarrow HNO_3 + HNO_3 \quad (1.20f)$$
$$N_2O_5 + HCl \rightarrow ClNO_2 + HNO_3 \quad (1.20g)$$

Additionally, NO_x (the sum of NO, NO_2 and their nighttime reservoir $2\,N_2O_5$), is converted to HNO_3 and removed from the gas phase, impeding the deactivation of ClO by reaction 1.19a. The partitioning between HCl and $ClONO_2$ at the beginning of the winter is to some extent important for the timing of the activation of chlorine, since the above reactions have different time scales and also depend on the type of the cloud surface. Activation is fastest when HCl and $ClONO_2$ have the same mixing ratio, since reaction 1.20a is the most rapid one.

If the particles in the clouds are large enough, sedimentation will set in, removing NO_x from the altitude layers of the clouds. The same is true for the HNO_3 directly produced by the reaction 1.19c which could react back to NO_x through

$$HNO_3 + h\nu \rightarrow OH + NO_2 \quad (1.21a)$$
$$HNO_3 + OH \rightarrow NO_3 + H_2O \quad (1.21b)$$

The removal of NO_x by means of sedimentation, which is called denitrification, will lengthen the process of ozone depletion, because it is made more difficult for ClO to return to its reservoir gases. While denitrification is quite common in the Antarctic, it has only been observed sporadically in the Arctic. Denitrification can be connected with dehydration in case of ice particles coated with NAT, or can happen just with NAT particles, where NAT rocks become very effective due to

their high fall velocities. Denitrification without dehydration was observed several times in the Arctic, which is another hint that NAT particles do not form indirectly through ice clouds. Small NAT particles or STS particles are less likely to cause denitrification due to their lower fall velocities.

Massive ozone loss will only start when sunlight reappears in the preconditioned stratosphere enabling catalytic cycles to destroy ozone in large quantities. The ClO cycle cannot explain the ozone loss rates due to the lack of atomic oxygen. Ozone is rather destroyed by the cycle

$$2\,Cl + 2\,O_3 \rightarrow 2\,ClO + 2\,O_2 \tag{1.22a}$$
$$ClO + ClO \xrightarrow{M} Cl_2O_2 \tag{1.22b}$$
$$Cl_2O_2 + h\nu \rightarrow ClOO + Cl \tag{1.22c}$$
$$ClOO \xrightarrow{M} Cl + O_2 \tag{1.22d}$$
$$2\,O_3 + h\nu \rightarrow 3\,O_2 \tag{1.22e}$$

discovered by Molina and Molina [1987]. The chlorine radicals are photochemically produced from the chlorine species on the right side of the reactions 1.20. The chlorine monoxide originating from the reaction with ozone 1.22a is stored in the dimer Cl_2O_2 at night, and is converted to chlorine dioxide when sunlight comes back. This leads to a diurnal cycle in ClO with low mixing ratios at night. A similar cycle exists for bromine:

$$Cl + O_3 \rightarrow ClO + O_2 \tag{1.23a}$$
$$Br + O_3 \rightarrow BrO + O_2 \tag{1.23b}$$
$$BrO + ClO \rightarrow Br + ClOO \tag{1.23c}$$
$$ClOO \xrightarrow{M} Cl + O_2 \tag{1.23d}$$
$$2\,O_3 + h\nu \rightarrow 3\,O_2 \tag{1.23e}$$

The bromine cycle makes up for about a third of the depletion of the chlorine cycle despite the low abundances of bromine in the stratosphere because bromine is less tightly bound than chlorine [Solomon, 1999].

Considering all effects, the strongest ozone depletion is usually found in the altitude layers around 20 km. This happens to be just the altitude where the peak concentrations can be found. A summary of the ozone destruction cycle is shown in Figure 1.7. In early winter, most of the chlorine is stored in the reservoir gases. When temperatures decrease in the polar night, polar stratospheric clouds free

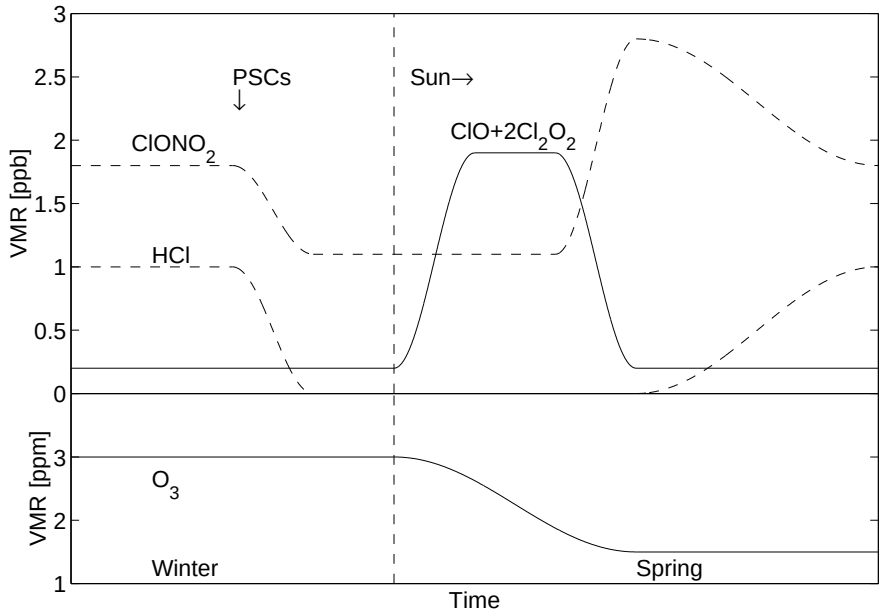

Figure 1.7: Ozone hole chemistry. Adapted from Webster et al. [1993].

chlorine from the reservoir gases. With the sun coming back in spring, ozone is destroyed by the catalytic cycles shown above. Eventually, the air warms up and the vortex is destroyed. In the following, air rich in NO_x is mixed in from mid latitudes, NO_x is set free again from the vanishing stratospheric clouds and produced photochemically by reaction 1.21a. Thus, the cycle will finally come to a stop via the reactions 1.19. Since reaction 1.19a is much faster than the reactions producing HCl, deactivation occurs mainly into $ClONO_2$, which only later in the year reaches equilibrium with HCl.

Regarding the future development of the ozone destruction, there are two diverging trends. On the one hand, the lower stratosphere was getting cooler in the last decades [Pawson and Naujokat, 1999] due to enhanced greenhouse-gas concentrations and decreasing wave activity in the surf zone, enlarging the area of polar stratospheric cloud formation and leading to a more stable vortex breaking up later in the year. A more stable vortex would not only lead to enhanced ozone depletion but also mean less downward transport and accumulation of ozone. On the other hand, the chlorine loading of the stratosphere is decreasing due to the Protocol of Montreal. Shindell et al. [1998] have used a circulation model with a very simple ozone chemistry (without denitrification) to make a long term prediction of ozone depletion in the Antarctic and the Arctic. They predict that Antarctic ozone loss will peak in 2010–2020 and and will not be detectable anymore by

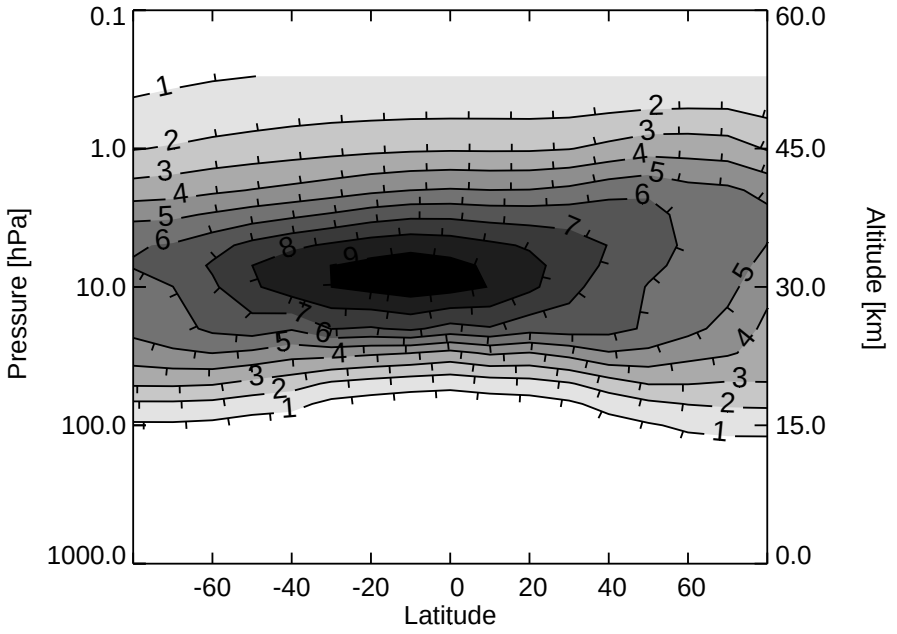

Figure 1.8: Latitudinal distribution of ozone volume mixing ratios in December. The contours show the mixing ratio in ppm. Taken from the climatology of Fortuin and Kelder [1998].

around 2050. In the Arctic, the interannual variability partially masks the trend in ozone, but the situation is roughly comparable here.

1.5 Ozone Distribution

The global ozone distribution is a result of both chemical and dynamical effects. In Figure 1.8 the mean ozone volume mixing ratios for December are shown as a function of altitude and latitude. A typical Arctic profile measured by the RAM can be found somewhat ahead in Figure 3.4, page 70. While in the upper atmosphere photochemistry is so fast that ozone concentrations are in photochemical equilibrium, transport processes are dominating in the lower atmosphere. Ozone is produced in the middle altitudes of the atmosphere. In high altitudes the lack of oxygen prevents the production of ozone, while in low altitudes the ultraviolet light needed for the photolysis has already been absorbed by ozone at higher levels. Therefore ozone forms a layer in the stratosphere. The main production area for ozone with the highest peak volume mixing ratios is situated in the tropics due to the intense radiation there. Paradoxically, the largest column amounts of ozone can be found in the high latitudes, see Figure 1.9. This is due to the

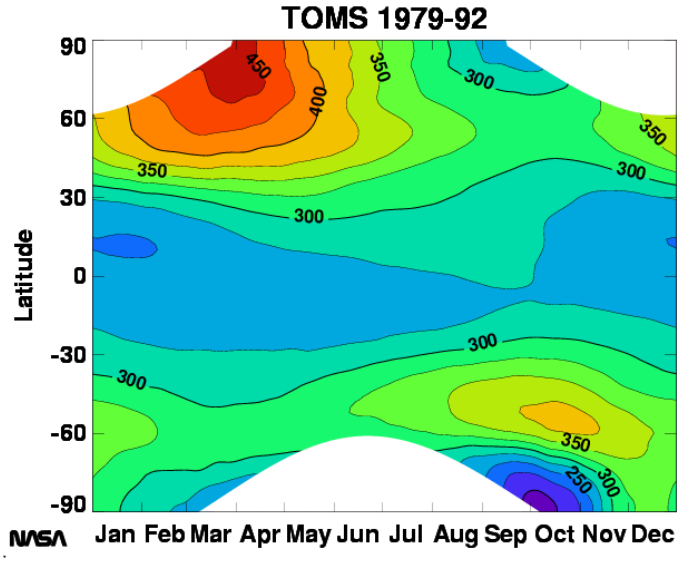

Figure 1.9: Mean annual cycle of ozone columns as a function of time and latitude measured by the TOMS instrument on board the Nimbus 7 satellite between 1979 and 1992. Contour lines show the column in steps of 25 DU.

Brewer-Dobson circulation, which very effectively carries ozone from low to high latitudes and from middle to low altitudes. This is also evident in the ozone mixing ratio profiles. While tropical ozone profiles have a prominent peak and a steep positive gradient in the lower stratosphere, Arctic ozone profiles have a less pronounced peak, but also a smaller gradient. The ozone layer also extends to lower altitudes in the polar region due to the lower tropopause. These two effects lead to higher columns, since number density (as a function of mixing ratio) falls exponentially with altitude.

Seasonal changes in the columns are very pronounced in the polar regions, but much less prominent in the tropics, as can be seen in Figure 1.9. In winter and spring, ozone columns rise due to the accumulation of ozone in the polar vortex caused by the Brewer Dobson circulation. While the columns rise to more than 450 DU in the northern vortex and have a maximum about 80° N, the columns only rise to about 350 DU in the southern vortex with a maximum about 60° S. This is due to the stronger downwelling in the weak northern vortex and the better isolation of air in the strong southern vortex. The low columns around October at the south pole mark the ozone hole. The difference between ozone columns

in southern mid latitudes and the south polar region is about 250 DU. To an extent of about 50 DU, this is a natural effect caused by the isolation of the vortex. The ozone hole chemistry can lower the columns by an additional 200 DU. In contrast, ozone depletion in the northern vortex is barely visible and superimposed by diabatic movements.

1.6 Chlorine Monoxide and Water Vapor

We will also have a short look at the other species measured by the RAM instrument. Chlorine monoxide is a trace gas with abundances in the ppb range. A typical chlorine monoxide profile measured by the RAM is shown in Figure 3.5, page 71. It has a natural peak in the upper stratosphere at about 40 km, which can be found throughout the sunlit globe and is caused by the catalytic chlorine cycle. The second peak at about 20 km is originating from the chlorine monoxide dimer cycle. It is a clear sign for ozone depletion and can only be observed in the polar spring in sunlight. Night time mixing ratios are almost zero at these altitudes.

Water vapor is very variable and can comprise up to 3% of the atmospheric composition in the troposphere. It is responsible for many weather phenomena, and essential to life on earth. Water vapor is also the most important greenhouse gas and has great influence on the radiation balance of the earth. In the troposphere, water vapor is not changed by chemistry very much and is in a rapid cycle of evaporation, transport and precipitation. The exponential decrease of water vapor with altitude is caused by condensation through adiabatic upward movements. Water vapor enters the stratosphere mainly in the tropical tropopause, which acts as a freezing trap for the vapor. Thus, stratospheric water vapor mixing ratios are much lower than in the troposphere and lie about 4 ppm. A typical stratospheric water vapor profile measured by the RAM is shown in Figure 3.2. The most important chemical reaction generating water vapor in the stratosphere is the oxidation of methane, leading to a conservation of the quantity $2\,CH_4 + H_2O$ and a minimum mixing ratio for water vapor in the lower stratosphere. In addition to that, water vapor has a role in ozone chemistry and cools the stratosphere radiatively. Thus, the observed increase of stratospheric water vapor of about 1% per year leads to colder temperatures in the vortex.

1.7 Literature

There is a wealth of literature on the topic of ozone depletion and related items, some of which will be introduced here. The bulk of the general information given here is taken from these sources. A nice overview of the history, concepts and

chemistry of ozone depletion can be found in [Solomon, 1999], which is a good paper to begin with. The extensive list of references therein is also worth a look. Overviews are also given in the reports of the WMO [WMO, 1999]. Some books worth to note are [Brasseur and Solomon, 1986] and [Wayne, 1991] for the chemical aspects and [Holton, 1992] for the dynamical aspects of stratospheric sciences.

2 Instrument

2.1 Overview

The Radiometer for Atmospheric Measurements (RAM) is a ground based microwave radiometer situated at Ny-Ålesund, Spitsbergen (78.9° N, 11.9° E). It is operated by the University of Bremen and the Alfred Wegener Institute of Polar and Marine Research (AWI) as part of the Network for the Detection of Stratospheric Change (NDSC). The instrument consists of three receivers sharing a common backend. Each receiver passively detects the thermal emission of rotational transitions of the measured species. The receivers measure a water vapor transition at 22.235 GHz, an ozone transition at 142.175 GHz and a chlorine monoxide transition at 204.352 GHz. The detected radiation is led through a quasi optics, collected by a horn antenna, down converted to an intermediate frequency, amplified and fed into an acousto-optical spectrometer. The intensity received by the spectrometer is calibrated absolutely by comparison with hot and cold black bodies. Volume mixing ratio profiles of all species are finally obtained from the pressure broadened shape of the rotational lines using the optimal estimation method.

Before we present the instruments and their several components, we will give an introduction to radiative transfer and absorption coefficients. Subsequently, the different parts of the instruments are described. We conclude the chapter with the different measurement techniques that can be used and their explanation. Additionally, we will have a short look at the BRERAM, a microwave radiometer measuring an ozone transition at 110.846 GHz at Bremen (53° N, 8° E).

General information about the RAM can be found in [Klein, 1993] and [Sinnhuber, 1995, 1999]. Chlorine monoxide measurements are also described in [Raffalski, 1998] and water vapor measurements in [Lindner, 2002]. Further information about radiative transfer, microwave spectra and measurement techniques can be found in [Janssen, 1993], [Townes and Schawlow, 1975] and [Ulaby et al., 1981, 1982, 1986].

2.2 Radiative Transfer

Microwave radiometers detect the thermal radiation originating in the atmosphere. A beam of radiation that crosses the atmosphere can be modified by absorption, scattering and emission. Scattering is negligible under fair weather conditions in the microwave region, so we will concentrate on emission and absorption here.

A body that absorbs all incident radiation is called a black body. A black body is also a perfect emitter, since a system of two identical black bodies has to stay in thermal equilibrium for symmetry reasons. Black body radiation is emitted according to Planck's law:

$$L_\nu^{\text{black}}(T,\nu) = \frac{2h\nu^3}{c^2}\frac{1}{\exp(\frac{h\nu}{k_B T}) - 1} \tag{2.1}$$

The spectral brightness L_ν is the power per solid angle, emitting area and frequency interval. It will be shown later that this is just the quantity received by the instrument. T is the thermodynamic temperature of the body, $h = 6.62 \times 10^{-34}$ Js is Planck's constant, k_B is Boltzmann's constant, ν is the frequency and $c = 3 \times 10^8$ m/s is the speed of light. For frequencies in the microwave region, $h\nu \ll k_B T$ is valid, and Planck's law is simplified as

$$L_\nu^{\text{black}}(T,\nu) \approx \frac{2\nu^2 k_B}{c^2} T \tag{2.2}$$

This is the Rayleigh-Jeans law, which has the pleasing property of being proportional to temperature. To obtain the same behavior for Planck's law, we define the brightness temperature

$$T_B(T,\nu) = \frac{h\nu}{k_B}\frac{1}{\exp(\frac{h\nu}{k_B T}) - 1} \tag{2.3}$$

which is virtually identical with T in the millimeter wave region. Now we get an exact identity for all frequencies

$$L_\nu^{\text{black}}(T,\nu) = \frac{2\nu^2 k_B}{c^2} T_B(T,\nu) \tag{2.4}$$

so that black body radiation detected by the instrument can easily be expressed in brightness temperatures.

In the microwave regime, absorption occurs when rotational states of molecules are excited by the incoming radiation. Absorption only happens at discrete frequencies corresponding to the quantum transitions of the molecules, rendering the atmosphere to a gray body with frequency dependent absorption. The absorption

coefficient $\alpha(z,\nu)$ is defined as the fraction of the radiation that is absorbed per unit interval, hence

$$dL_\nu = \alpha(z,\nu)L_\nu(z,\nu)\,dz \tag{2.5}$$

where L_ν is the spectral brightness of the beam which should not be confused with the black body radiation L_ν^{black}. dz is assumed to follow the path of the beam. The absorption coefficient is evidently proportional to the number of absorbing gas molecules, but is also dependent on the properties of the molecules, as described in the next section. A quantity related to α is the opacity, the integral of the absorption coefficient

$$\tau(z_1,z_2,\nu) = \int_{z_1}^{z_2} \alpha(z,\nu)\,dz \tag{2.6}$$

If $\tau \to 0$ the atmosphere is transparent, while $\tau \to \infty$ means that the atmosphere is opaque.

The emission coefficient of a gray body like the atmosphere is equal to the absorption coefficient according to Kirchhoff's law. If we combine Kirchhoff's law and Equation 2.5, we get the net effect of absorption and emission

$$dL_\nu = \alpha(L_\nu - L_\nu^{\text{black}})\,dz = (L_\nu - L_\nu^{\text{black}})\,d\tau \tag{2.7}$$

Integration gives the radiative transfer equation or Schwarzschild equation

$$\begin{aligned} L_\nu(z_0,\nu) &= L_\nu(z_\infty,\nu)e^{-\int_{z_0}^{z_\infty}\alpha(z',\nu)\,dz'} \\ &\quad + \int_{z_0}^{z_\infty} \alpha(z',\nu)L_\nu^{\text{black}}(T(z'),\nu)e^{-\int_{z_0}^{z'}\alpha(z'',\nu)\,dz''}\,dz' \end{aligned} \tag{2.8}$$

where z_0 and z_∞ are two arbitrary altitudes. If we extend the definition of the brightness temperature in Equation 2.4 to arbitrary radiation by replacing L_ν^{black} by L_ν, we can substitute the powers by brightness temperatures, yielding

$$\begin{aligned} T_{\text{B}}(z_0,\nu) &= T_{\text{B}}(z_\infty,\nu)e^{-\int_{z_0}^{z_\infty}\alpha(z',\nu)\,dz'} \\ &\quad + \int_{z_0}^{z_\infty} \alpha(z',\nu)T_{\text{B}}^{\text{black}}(T(z'),\nu)e^{-\int_{z_0}^{z'}\alpha(z'',\nu)\,dz''}\,dz' \end{aligned} \tag{2.9}$$

We will see soon that $T_{\text{B}}(z_0,\nu)$ is the quantity measured by the instrument. Thus, we have to know about the absorption coefficients and the temperature and pressure of the atmosphere to reconstruct the measurement. A typical spectrum of the

sky in the microwave region is shown in Figure 2.1. For a deeper understanding of the shape of the spectrum, we will need more knowledge of the absorption coefficients, which is given in the next section.

If we want to calculate with altitudes instead of integrating along the path of the beam, we have to substitute all occurrences of z with the altitude r and to replace dz by $(dz/dr)dr$. For an instrument with a pencil beam antenna looking up under the angle ϑ, the result is

$$\frac{dz}{dr} = \frac{1 + r/a}{\sqrt{\sin^2\vartheta + 2r/a + r^2/a^2}} \tag{2.10}$$

if the curvature of the earth is considered. The radius of the earth is denoted by a.

2.3 Absorption Coefficients

The information about the mixing ratio profile of the observed species is contained in the absorption coefficients. The absorption coefficient of the atmosphere can be written as

$$\alpha(z,\nu) = \sum_{ki} \alpha^*_{ki}(z,\nu) x_k(z) \tag{2.11}$$

with k indicating the molecules that form the atmosphere and i denoting the transitions of every species. x_k is the volume mixing ratio of the species and α^*_{ki} is called absorption cross section. The absorption cross section for a single transition is given by

$$\alpha^*_{ki}(z,\nu) = n(z) a_{ki} S_{ki}(z) F_{ki}(z,\nu) \tag{2.12}$$

n is the number density of air, a is the ratio of the isotope that performs the transition, S is the line strength and F is the form factor, which gives the frequency dependent term. The quantum mechanical expression for the cross section yields no clear distinction between S and F, so their definition is somewhat arbitrary. We will follow Janssen [1993] here. The frequency dependence has several causes:

- Natural line width
- Doppler broadening
- Pressure broadening
- Frequency shift

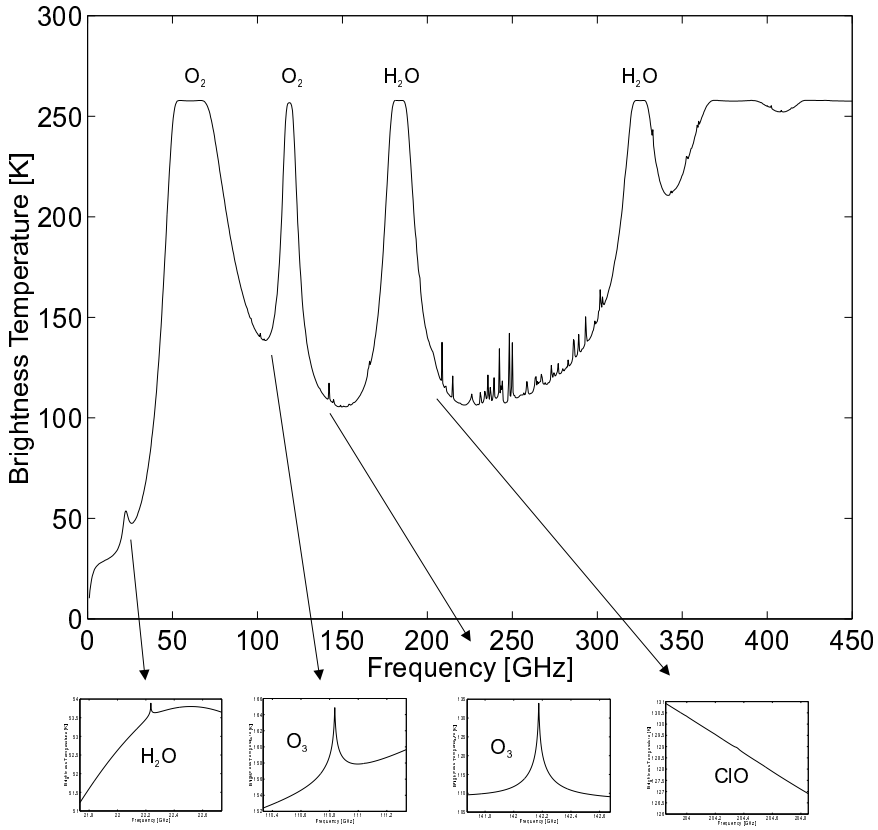

Figure 2.1: Atmospheric spectrum from 0 GHz to 400 GHz for a subarctic standard atmosphere, seen from the ground with an measurement zenith angle of 70°. Arrows show the position of the spectra measured by the 22 GHz water vapor, 110 GHz ozone, 142 GHz ozone and 204 GHz chlorine monoxide radiometers. Above 400 GHz, the atmosphere is opaque.

The natural line width is caused by the uncertainty principle and is totally negligible for rotational transitions in the microwave region. Doppler broadening is caused by the motion of the molecules of the air relative to the observer. The result for the form factor is

$$F_{\mathrm{D}}(\nu) = \frac{1}{\pi^{1/2}\gamma_{\mathrm{D},i}} \exp\left(-\left(\frac{\nu-\nu_i}{\gamma_{\mathrm{D},i}}\right)^2\right) \tag{2.13}$$

The transition frequency is denoted by ν_i. The Doppler broadening parameter $\gamma_{\mathrm{D},i}$ is given by

$$\gamma_{\mathrm{D},i} = \nu_i \left(\frac{2k_{\mathrm{B}}T}{m_k c^2}\right)^{1/2} \tag{2.14}$$

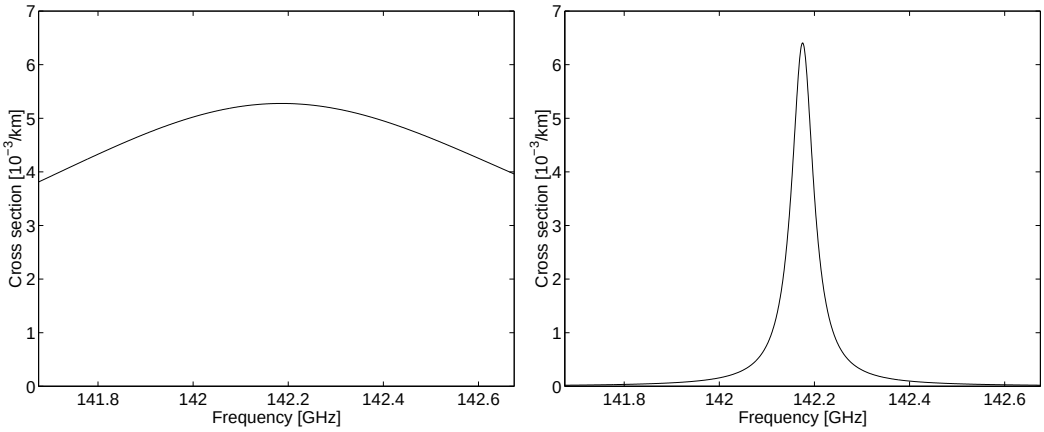

Figure 2.2: Line shape due to pressure broadening. Absorption cross sections for 10 km and 30 km altitude for ozone at 142 GHz.

It depends on the temperature T and the molecular weight m_k of the species. Pressure broadening is caused by the decrease of the lifetime of ground states and excited states of the observed molecule, originating from collisions of the molecules. The higher the pressure, the shorter is the time between collisions and the more the lifetime is decreased, leading in turn to an increase of the half width of the line according to Heisenberg's uncertainty principle. Thus, broad lines originate from low altitudes and narrow lines originate from high altitudes (see Figure 2.2). The most common approach for the line shape of the pressure broadening is the van Vleck-Weisskopf line shape

$$F_{\mathrm{C}}(\nu,\nu_i) = \frac{1}{\pi}\left(\frac{\nu}{\nu_i}\right)^2 \left(\frac{\gamma_{\mathrm{C},i}}{(\nu-\nu_i)^2+\gamma_{\mathrm{C},i}^2} + \frac{\gamma_{\mathrm{C},i}}{(\nu+\nu_i)^2+\gamma_{\mathrm{C},i}^2}\right) \tag{2.15}$$

This line shape was derived by van Vleck and Weisskopf [1945] under the approximation that the collisions are sufficiently short and strong. The pressure broadening parameter $\gamma_{\mathrm{C},i}$ is given by

$$\gamma_{\mathrm{C},i} = w_i(p-p_k)\left(\frac{T_0}{T}\right)^{x_i} + w_{\mathrm{s},i}p_k\left(\frac{T_0}{T}\right)^{x_{\mathrm{s},i}} \tag{2.16}$$

where the first term describes broadening due to oxygen and nitrogen and the second term describes self broadening due to the observed molecule itself. The parameters w_i, x_i, $w_{\mathrm{s},i}$ and $x_{\mathrm{s},i}$ have to be determined empirically. T_0 is an arbitrarily chosen reference temperature, and p and p_k are the pressures of the atmosphere and of the observed species, respectively. Near ν_i, the van Vleck-Weisskopf line

shape can be simplified:

$$F_{\mathrm{L}}(\nu,\nu_i) = \frac{1}{\pi}\frac{\gamma_{\mathrm{C},i}}{(\nu-\nu_i)^2+\gamma_{\mathrm{C},i}^2} \tag{2.17}$$

This is the Lorentz line shape, which is equivalent to the line shape of a classical oscillator. The shape of an atmospheric line near ν_i is the convolution of the Lorentz line shape and the Doppler line shape

$$F_{\mathrm{V}}(\nu,\nu_i) = \int_{-\infty}^{\infty} F_{\mathrm{L}}(\nu-\nu',\nu_i)F_{\mathrm{D}}(\nu')\,\mathrm{d}\nu' \tag{2.18}$$

and is called Voigt line shape. The integral of the Voigt line shape can only be calculated numerically, see for example [Drayson, 1976]. The line shape used for all calculations here is a combination of the van Vleck-Weisskopf line shape and the Voigt line shape, which is correct for a wide range of frequencies:

$$F(\nu,\nu_i) = \left(\frac{\nu}{\nu_i}\right)^2 (F_{\mathrm{V}}(\nu,\nu_i)+F_{\mathrm{V}}(\nu,-\nu_i)) \tag{2.19}$$

In addition to the broadening of lines, a shift in the center frequency can occur. Since this is only important for water vapor, it will be treated in Section 3.4.5. The line strength for a transition from the energy E_{i_2} to the energy E_{i_1} is given by

$$S_{ki}(T) = \frac{8\pi^3\nu_i^2\mu_i^2 g_i}{3hcQ_k(T)}\left(\exp\left(\frac{-E_{i_1}}{k_{\mathrm{B}}T}\right)-\exp\left(\frac{-E_{i_2}}{k_{\mathrm{B}}T}\right)\right) \tag{2.20}$$

where ν_i is the line frequency, μ_i is the quantum mechanical transition probability and g_i is the weight according to the nuclear spin. The partition function $Q(T)$ is in good approximation given by the product of the vibrational, rotational and electronic partition functions, thus $Q_k(T) = Q_{\mathrm{vib},k}(T)Q_{\mathrm{rot},k}(T)Q_{\mathrm{el},k}(T)$. For our instruments, $Q_{\mathrm{el},k}$ does only play a role for chlorine monoxide. Assuming $E_{i_1} - E_{i_2} \ll k_{\mathrm{B}}T$, we obtain the formula

$$S_{ki}(T) = S'_{ki}(T_0)\left(\frac{T_0}{T}\right)^{q_k+1}\frac{1}{Q_{\mathrm{vib},k}(T)}\exp\left(b_i(1-\frac{T_0}{T})\right) \tag{2.21}$$

used by Janssen [1993], where most spectral parameters were taken from. The line strength at the reference temperature T_0 is defined by $S'_{ki}(T_0) = S_{ki}(T_0)Q_{\mathrm{vib},k}(T_0)$ and is tabulated for many species. The parameter b_i is given by $(E_{i_1}+E_{i_2})/(2k_{\mathrm{B}}T_0)$. For the above formula $Q_{\mathrm{rot},k}(T) \sim T^{q_k}$ is assumed, where q_k is 0 for an atom, $1/2$

for a linear molecule and $3/2$ in any other case. The vibrational sum has to be computed from the fundamental vibrational states:

$$Q_{\mathrm{vib},k} = \prod_l \left(\frac{1}{1 - \exp(-\frac{T_{kl}}{T})} \right)^{d_{kl}} \tag{2.22}$$

The energy of the states is $E_{kl} = k_\mathrm{B} T_{kl}$ and d_{kl} is the degeneration of the states. Finally, the electronic sum for chlorine monoxide is given by

$$Q_{\mathrm{el},k} = 1 + \exp(-T_{\mathrm{el},k}/T) \tag{2.23}$$

with the electronic state energy $E_{\mathrm{el},k} = k_\mathrm{B} T_{\mathrm{el},k}$.

The most prominent line spectra in the microwave region are caused by water vapor with its strong dipole moment and by oxygen. Although oxygen has no electric dipole moment, its magnetic dipole moment and the large abundance in the atmosphere lead to rather strong lines. Nitrogen has no lines in the microwave region due to its vanishing dipole moments. Ozone exhibits a multitude of lines, but the line strengths are somewhat lower than for oxygen or water vapor due to the lower mixing ratios. In addition to the line spectra, water vapor and nitrogen continua can be found. The water vapor continuum is possibly caused by deviations of the line shape from the van Vleck-Weisskopf line shape far from the line centers, and is to some extent dependent on which lines are explicitly calculated. Thus, it can not be considered as a real continuum.

2.4 Instrument Description

2.4.1 Quasi Optics

The radiation received by the instrument originates either from the atmosphere, a hot black body, or two different cold black bodies. Radiation from the atmosphere enters the laboratory through a styrofoam window, which is transparent in the microwave region. A rotating mirror is pointed to one of the sources according to a computer controlled program and leads the radiation to a quasi optics. The purpose of the quasi optics is to focus the radiation and to restrict the received frequency range. The name quasi optics is due to the similar behavior of microwaves and visible light, apart from some features like a pronounced transverse spreading of the beam. For some more detailed information about microwave optics, see [Goldsmith, 1998]. We will concentrate on the optics of the ozone radiometer for now, since it is the most complicated one. The optics of the other instruments are analogous. An outline of the ozone quasi optics is shown in Figure 2.4.

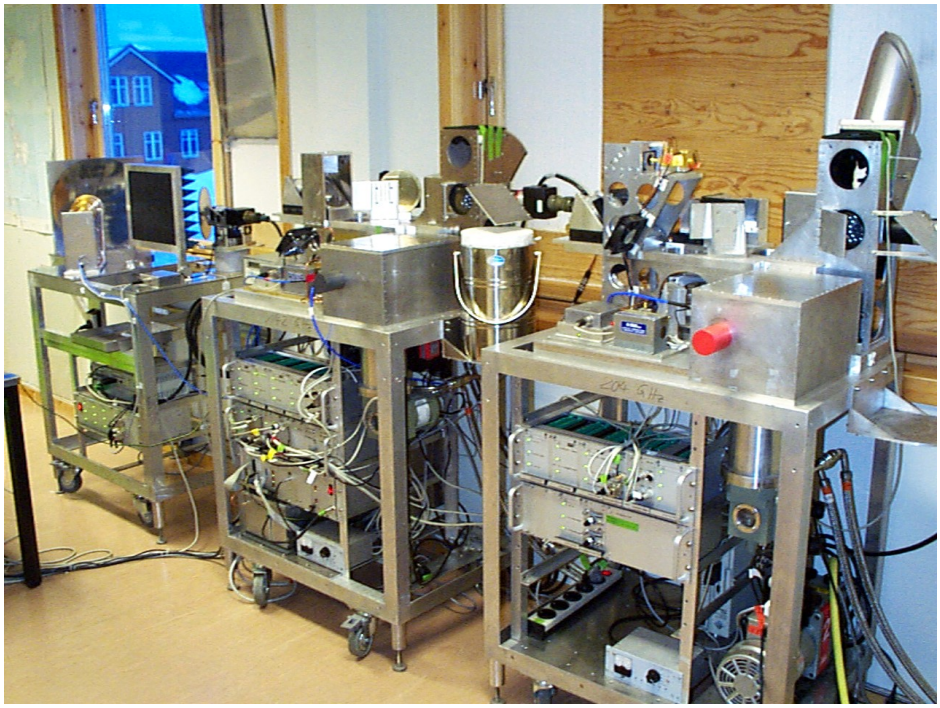

Figure 2.3: The radiometers in the laboratory in Ny-Ålesund. From left to right: The water vapor, ozone and chlorine monoxide frontend. The middle rack contains the backend.

Some of the mirrors in the optics are just used to focus and redirect the radiation, like the mirrors E0 up to E5. But some parts of the optics require a deeper investigation. The first element of interest is the dichroitic plate D. It is used to suppress unwanted frequency contributions in the radiation and consists of a metal plate with concentric holes, which lead to a frequency dependent reflection coefficient. Next, the path length modulator R3 is used to suppress Fabry-Pérot interferences in the optics by periodically changing the optical path length with a moving rooftop mirror.

The most important element is the Martin-Puplett interferometer, which is used as a bandpass filter to suppress unwanted frequency ranges. It consists of the fixed rooftop mirror R1, the movable rooftop mirror R2 and the wire grid G1. The wire grid transmits or reflects the incoming radiation depending on its polarization. It can be shown that if the path length difference between the fixed rooftop mirror and the grid and the movable rooftop mirror and the grid is not zero, radiation is transformed between the polarizations without changing the overall power. Therefore it is possible to attenuate the radiation by adding wire grids as polarization filters at the exit and the entrance of the interferometer. The wire grid G2

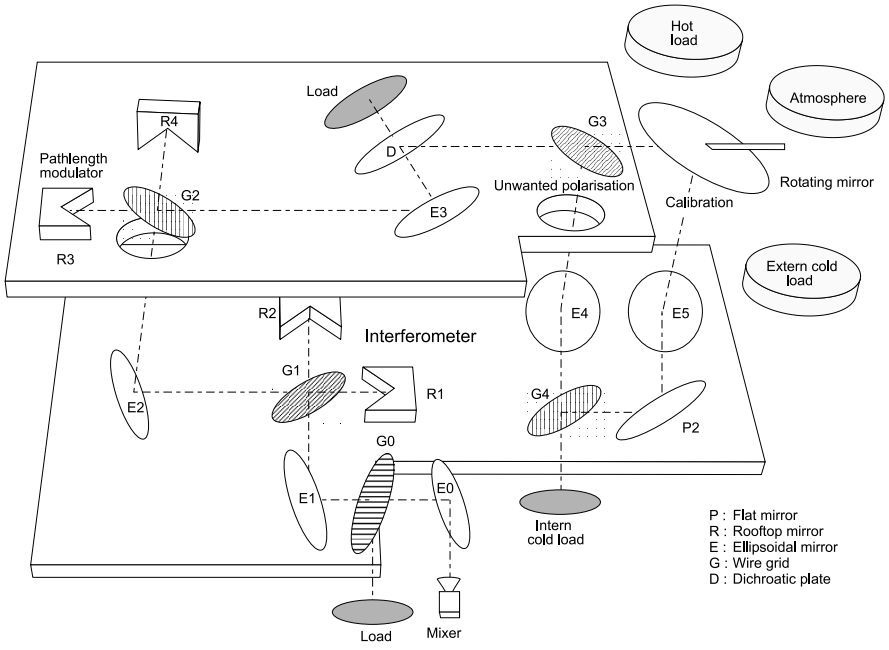

Figure 2.4: Quasi optics of the 142 GHz radiometer

forms the entrance of the interferometer, while the wire grid G0 is the exit. If δ is the path length difference, the attenuation of the incoming radiation is given by

$$D = \frac{1}{2}(1 \pm \cos(2\pi\delta\nu/c)) \tag{2.24}$$

where ν is the frequency and c is the speed of light. Depending on the relative position of the wires of the wire grids at the entrance and the exit to each other and the use of the transmitted or reflected incoming beam as a signal beam, the polarization of the signal beam is rotated by 90° or left in its original polarization. The negative sign corresponds to rotating operation, while the positive sign corresponds to non-rotating operation. The wire grids at the entrance and the exit are orientated for non-rotating operation. δ is chosen so that transmission is at a maximum for $\nu = \nu_i$ and at a minimum where the largest unwanted contribution occurs.

2.4.2 Antenna and Mixer

The power per frequency that is detected by the horn antenna (save for the effect of the interferometer) can be described as

$$P_{\text{horn}} = \frac{1}{2} A_{\text{eff}} \Omega_{\text{eff}} L_\nu \tag{2.25}$$

where A_{eff} is the effective antenna area, Ω_{eff} is the effective detecting angle and L_ν is the intensity of the radiation. The Etendu principle, which shall not be derived here, states

$$\lambda^2 = A_{\text{eff}}\Omega_{\text{eff}} \tag{2.26}$$

where λ is the wavelength. Combining the Etendu principle with the definition of the brightness temperature in Equation 2.4 gives a simple relationship between spectral power and brightness temperature

$$P_{\text{horn}} = k_{\text{B}}T_{\text{B}} \tag{2.27}$$

Since commonly used amplifiers are not able to amplify the frequencies that we wish to detect, the signal is down converted to an intermediate frequency. This is achieved by mixing the atmospheric signal with the much stronger signal of a local oscillator and passing it to a device with a non-linear response of the resulting current to the induced voltage. Such a configuration is called a heterodyne receiver. It can be shown that the relationship between the local oscillator frequency ν_{LO}, the intermediate frequency ν_{IF} and the amplified atmospheric frequencies $\nu_{\pm n}$ is

$$\nu_{\pm n} = n\nu_{\text{LO}} \pm \nu_{\text{IF}}, \quad n \in \mathbb{N}_0 \tag{2.28}$$

If the intermediate frequency and the local oscillator frequency are given, several discrete signal frequencies are amplified at the same time, giving a superposition of the spectral powers of the single frequencies. It can be shown that the spectral powers of the different frequencies are not amplified with the same efficiency. The resulting spectral power is rather

$$P = \sum_{n\in\mathbb{Z}} L(\nu_n)T_{\text{B}}(\nu_n) \tag{2.29}$$

where the T_{B} are the brightness temperatures at the different frequencies and the L are proportionality factors. The signal frequencies are called side bands, with ν_1 giving the upper side band and ν_{-1} giving the lower side band of the first order. Both side bands can be used as signal bands, with the other side band being the mirror side band. The local oscillator frequency is normally chosen near the line frequency to obtain a small intermediate frequency. The local oscillator frequencies are 14.235 GHz for water vapor, 134.175 GHz for ozone and 196.352 GHz for chlorine monoxide, corresponding to an intermediate frequency of 8 GHz at the line center. The use of the Martin-Puplett interferometer becomes clear here. It can be used to suppress at least one of the unwanted side bands, most often the mirror side band of the first order is suppressed because it is usually the strongest

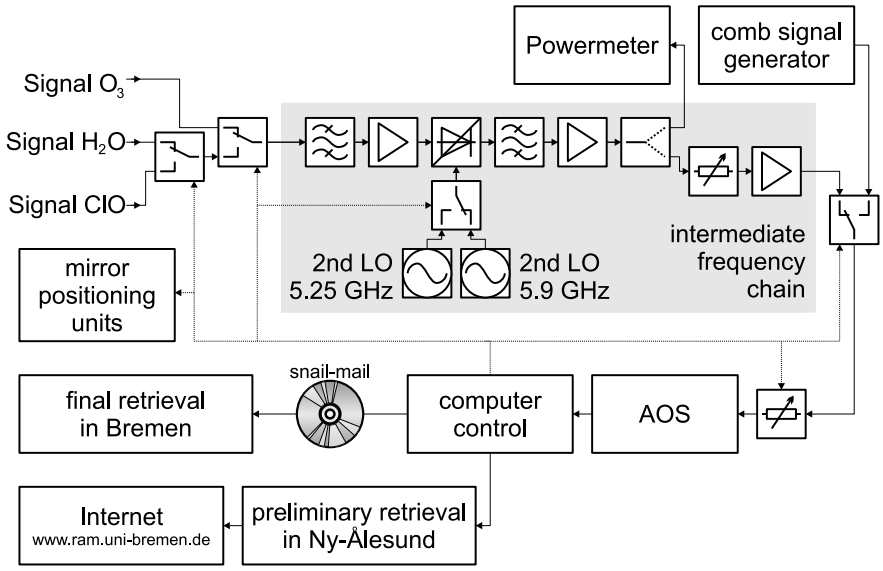

Figure 2.5: The backend of the radiometers in Ny-Ålesund

one. Since the interferometer influences the proportionality factors, they have to be written as $L(\nu_n) = \Lambda(\nu_n)D(\nu_n)$ where the Λ are constants called conversion modes and D is the band pass of the interferometer.

We will now give some implementation details. The mixer and the first amplifier are situated inside a vacuum chamber and can be cooled down to 12 K by liquid helium. This is done to lower the thermal noise in the measurement. The mixer consists of a Schottky diode situated behind the horn antenna to which the radiation of a local oscillator basing on a Gunn device is coupled by a waveguide. The zenith angle of the antenna is chosen to be 70° for ozone and is variable (but similar) for chlorine monoxide and water vapor. This is a compromise between higher attenuation of the line in the troposphere with higher zenith angles and lower intensity of the stratospheric line with lower zenith angles. The antenna pattern is assumed to be a pencil beam.

2.4.3 Intermediate Frequency Chain

The first element of the intermediate frequency chain is a bandpass filter with a bandwidth from 6.8 GHz to 8.5 GHz. After 22 dB of amplification the signal is mixed for a second time in order to transform the signal to the 1.6 GHz to 2.6 GHz range of the spectrometer. Since the signal has 1.7 GHz bandwidth and the spectrometer only 1 GHz bandwidth, the range from 6.85 GHz to 7.85 GHz and the range from 7.5 GHz to 8.5 GHz are given in turn to the spectrometer. Two local

oscillators with 5.25 GHz and 5.9 GHz that can be put into the chain alternatively by a microwave switch are used for this. Later, the two spectra are merged again. Finally the signal is led through another bandpass filter, a 33 dB amplifier, a 22 dB amplifier, a power divider (as input for a powermeter), a microwave switch and a switchable attenuator. The last microwave switch changes between the intermediate frequency chain and a comb generator used for frequency calibration. The last element of the chain is the spectrometer.

2.4.4 Acousto Optical Spectrometer

The acousto optical spectrometer decomposes the microwave radiation into its spectrum. The microwave radiation excites a transducer coupled to a crystal, which is set into acoustic oscillations. That modifies the refraction index of the crystal periodically. A laser beam penetrating the crystal is diffracted by the acoustic oscillations. The intensity of the laser beam diffracted to the angle ϑ is proportional to the intensity of the microwave radiation at the frequency $\nu = \vartheta n c_s/\lambda_l$, where c_s is the speed of sound, n is the mean refraction index and λ_l is the wavelength of the laser. The laser light is detected by a CCD array with 1728 channels. Although the gap between the channels is 0.56 MHz, the resolution of the spectrometer is only 1.6 MHz due to the scattering of laser light.

2.4.5 Bremen Radiometer

The ozone radiometer in Bremen (BRERAM) was built in 1997 and began operational measurements in 2000. It detects the rotational transition of ozone at 110.836 GHz. Optics and backend are similar to the RAM, so we will not go into detail here. Measurement quality is somewhat lower in Bremen than in Ny-Ålesund, since the measurements are more affected by water vapor here. More information on the instrument can be found in [Tuckermann, 1997] and [Hoock, 2000].

2.5 Measurement Principle

The spectral power that is received by the spectrometer is composed of two parts. The actual spectrum is superimposed on the system noise of the instrument, which is usually much larger than the detected signal. The spectral power P_a of the atmosphere can be expressed in terms of brightness temperatures, which are proportional to the spectral power:

$$P_\mathrm{a} = G(T_\mathrm{B,a} + T_\mathrm{B,sys}) \tag{2.30}$$

The measured atmospheric signal is denoted by $T_{\mathrm{B,a}}$. G is an amplifying factor and $T_{\mathrm{B,sys}}$ is the system noise temperature corresponding to the system noise $P_{\mathrm{sys}} = GT_{\mathrm{B,sys}}$. The system noise should not be confused with the actual noise that can be seen on the spectrum. It is related to the system noise by

$$\sigma \sim \frac{T_{\mathrm{B,sys}}}{\sqrt{\Delta\nu\Delta t}} \tag{2.31}$$

where $\Delta\nu$ is the frequency resolution of the instrument and Δt is the integration time. The system noise itself can be thought of as a bias signal that is even present when no radiation is measured. It originates from several sources like thermal noise in the amplifiers or termination loads in the optics.

2.5.1 Totalpower Method

The totalpower method is used by the ozone radiometers in Bremen and Spitsbergen. Some measurements have also been carried out with the water vapor radiometer, with promising results. The method depends on a sufficiently strong spectral signature. All three variables in Equation 2.30 are unknown, so that additional equations are needed. For this reason, a hot and a cold black body are measured in turn with the atmosphere:

$$P_{\mathrm{h}} = G(T_{\mathrm{B,h}} + T_{\mathrm{B,sys}}) \tag{2.32}$$

$$P_{\mathrm{c}} = G(T_{\mathrm{B,c}} + T_{\mathrm{B,sys}}) \tag{2.33}$$

The radiation $T_{\mathrm{B,h}}$ and $T_{\mathrm{B,c}}$ of the black bodies is well known, when we know their physical temperatures. Thus, we obtain a system of three equations with three unknown variables, which can easily be solved. For the atmospheric spectrum, we gain

$$T_{\mathrm{B,a}} = T_{\mathrm{B,c}} + \frac{T_{\mathrm{B,h}} - T_{\mathrm{B,c}}}{P_{\mathrm{h}} - P_{\mathrm{c}}}(P_{\mathrm{a}} - P_{\mathrm{c}}) \tag{2.34}$$

Solving for the system noise, we get

$$T_{\mathrm{B,sys}} = \frac{T_{\mathrm{B,h}} - yT_{\mathrm{B,c}}}{y-1} \quad \text{with} \quad y = \frac{P_{\mathrm{h}}}{P_{\mathrm{c}}} \tag{2.35}$$

Let us now have a look at the implementation of the totalpower method for the ozone radiometer in Spitsbergen. The hot black body is realized by a piece of foamed plastic at room temperature. The temperature, which is needed in the above formulas, is measured by a Pt-100 diode. There are two different cold black bodies. The extern cold black body consists of a dewar vessel filled with

liquid nitrogen at 77 K. The dewar is protected by a lid, so that the nitrogen cannot evaporate. Since the radiometer measures the combined temperatures of the lid and the nitrogen, the temperature of the lid is measured once per day in a calibration measurement. The intern cold black body is situated inside the vacuum chamber for the mixer and is not used in the moment. For the spectra, the hot load, the cold load and the atmosphere are measured in turn for about 1 s. The counts of the CCD are then summed up for 40 s. The totalpower formula is applied to every single measurement, and the resulting spectra are integrated until a integration time of about 200 s is reached.

2.5.2 Reference Beam Method

For the very weak lines of the chlorine monoxide radiometer and the moderately weak line of the water vapor radiometer, the reference beam technique is used. This method, which was developed by Parrish et al. [1988], has the advantage of canceling any non-linearities in the relationship between spectral power and brightness temperature. On the other hand, we loose the information about the spectral bias, because it is implicitly subtracted. The reference beam technique uses a second source of radiation which is adjusted to match the spectral power of the signal beam, but does not contain the line. Subtraction of the two spectra eliminates non-linearities, but does conserve the information that is contained in the line. In our case, the reference source is a second beam pointing in a different direction than the signal beam. The reference beam is attenuated by an absorber, usually an acryl glass plate, to suppress the line information. Additionally, a substantial amount of radiation is added by thermal emission from the acryl glass plate. The angle of the signal beam is adjusted in order to match the spectral powers of the signal beam and the reference beam.

If P_r is the spectral power of the reference beam and P_s is the spectral power of the signal beam, a derivation similar to the total power method yields

$$\frac{P_\mathrm{s} - P_\mathrm{r}}{P_\mathrm{r}} = \frac{T_\mathrm{B,s} - T_\mathrm{B,r}}{T_\mathrm{B,r} + T_\mathrm{B,sys}} \tag{2.36}$$

The system noise $T_\mathrm{B,sys}$ has to be determined in a second measurement. $T_\mathrm{B,s}$ and $T_\mathrm{B,r}$ are the brightness temperatures of the signal and reference spectra, respectively.

The line of the chlorine radiometer is so weak that the reference beam technique is not sufficient to obtain spectra where the instrumental features are smaller than the line. Thus, we take advantage of the strong diurnal variation of chlorine monoxide in the lower stratosphere and subtract night time measurements, where almost no chlorine monoxide is present in the lower stratosphere, from day time measurements [de Zafra et al., 1989]. Day time is defined as 1 hour after sunrise

to 1 hour before sunset in the stratosphere or the 2 hours around local noon when the day is too short for this condition. Night time is defined from 3 hours after sunset to 1 hour before sunrise. In dusk and dawn, chlorine monoxide is not in photochemical equilibrium and exhibits a fast change in its mixing ratio, with a rapid increase due to photolysis in the morning and a somewhat slower decrease due to the back reaction to the dimer in the evening.

3 Retrieval

3.1 Overview

The aim of the retrieval is to obtain volume mixing ratios and other desired quantities from the measured spectrum. The spectrum is supposed to be some function of the quantities we want to retrieve. Hence, we can obtain these quantities by determining the inverse of this function. Unfortunately, the inversion is a mathematically ill-posed problem in case of the radiative transfer equation. A standard approach to solve such problems is the optimal estimation method. Thus, section 3.2 deals with the general application of this method to our data.

Sections 3.3 and 3.4 describe the detailed implementation of the retrieval for the different instruments. In addition to the existing software for ozone and chlorine monoxide retrieval in Spitsbergen, some new retrieval software had to be developed for the instruments built in the last three years, namely the water vapor radiometer in Spitsbergen and the ozone radiometer in Bremen. A complete rewrite of the existing retrieval software, which resulted in a much faster, easier to use and more complete program, was also performed. All parts of the software were developed in Matlab, an interpreter language specialized in matrices and numerical mathematics. The forward models and retrieval methods for the ozone and chlorine monoxide radiometers are described in a general manner in section 3.3, together with some examples for spectra, profiles and altitude range and resolution. Section 3.4 deals with the challenges posed by the water vapor radiometer. The water vapor line is surprisingly difficult to retrieve, due to facts as the exponential decrease in mixing ratios and a complicated line form. Some methods of dealing with these problems or circumventing them are described, and first preliminary profiles are shown.

3.2 Optimal Estimation

The optimal estimation method is a convenient way to retrieve some searched parameters from given data that are a function of these parameters, especially

if the corresponding mathematical problem is underconstrained or ill-posed. A thorough description of the optimal estimation method and the general problem of data inversion can be found in [Rodgers, 2000].

We assume that the given data $\mathbf{y}$ are some arbitrary function $\mathbf{F}(\mathbf{x})$ of the searched parameters $\mathbf{x}$ and that some statistical error ε is superimposed on the data:

$$\mathbf{y} = \mathbf{F}(\mathbf{x}) + \varepsilon \tag{3.1}$$

For example, $\mathbf{x}$ may be a vector of volume mixing ratios in different altitudes and $\mathbf{y}$ may be a vector of brightness temperatures at different frequencies. Discretizing these normally continuous functions is necessary to compute a numerical solution, but it is also convenient to be able to use matrix algebra. The vector valued function $\mathbf{F}(\mathbf{x})$ is called the forward model and contains the physics of the problem, in our case the radiative transfer equation. Normally, it is only an approximation to the real physics of the problem, which may be too complex or unknown.

At first, we will examine the case of a linear forward model. We will see later that the more common case of a non-linear problem can often be treated by linearization. The linear case is given by

$$\mathbf{y} = \mathbf{F}(\mathbf{x}_0) + \mathbf{K}(\mathbf{x} - \mathbf{x}_0) + \varepsilon \tag{3.2}$$

where $\mathbf{x}_0$ is some arbitrary point for the time being. The constant matrix $\mathbf{K}$ is called weighting function matrix. If we use $\mathbf{F}(\mathbf{x}) - \mathbf{F}(\mathbf{x}_0)$ instead of $\mathbf{F}(\mathbf{x})$ and $\mathbf{x} - \mathbf{x}_0$ instead of $\mathbf{x}$, which is easily reversible, we get

$$\mathbf{y} = \mathbf{K}\mathbf{x} + \varepsilon \tag{3.3}$$

Usually we have more data than retrieved parameters. Thus, at first glance, this is an overdetermined system of equations, which can be solved by minimizing the squared difference $(\mathbf{K}\hat{\mathbf{x}} - \mathbf{y})^2$, where $\hat{\mathbf{x}}$ is the estimated solution. However, there are problems with this approach. It turns out that the matrix $\mathbf{K}$ is ill-posed in the case of the radiative transfer problem, meaning that the matrix is formally overdetermined, but that its rows are almost linearly dependent. Thus small errors in the data, introduced by noise or the truncation of numbers on the computer, lead to large errors in the result $\hat{\mathbf{x}}$. An approach to understand this is to examine the null space of $\mathbf{K}$. Underdetermined matrices have a null space. If there is a null space, there are solutions to the equations which do not contribute to the spectrum

$$\mathbf{K}\mathbf{x}_{\text{null}} = \mathbf{0} \tag{3.4}$$

and therefore can not be measured. Hence, we can add an arbitrary vector from the null space to a solution and still get the same spectrum, even if we scale the

vector with a very large number. The problem is made worse by the noise on the spectrum, which allows for even more possible solutions. This leads to large oscillations of the estimated solution around the true state of the atmosphere, if not treated properly.

The approach taken in the optimal estimation method is to provide virtual measurements to stabilize the inversion. We assume that we know at least the mean $\mathbf{x}_0$ and the covariances $\mathbf{S}_x$ of an independent measurement series, giving us some a priori knowledge on the overall appearance of our parameters $\mathbf{x}$. The definition of the covariance matrix $\mathbf{S}_x$ can be found in Appendix 3.A. $\mathbf{x}_0$ is called a priori profile and $\mathbf{S}_x$ is called a priori covariance. We now minimize the deviation of the resulting profile $\hat{\mathbf{x}}$ from the a priori profile $\mathbf{x}_0$ and the deviation of the spectrum $\mathbf{y}$ from the synthetic spectrum $\mathbf{F}(\hat{\mathbf{x}})$ at the same time

$$\chi^2 = (\hat{\mathbf{x}} - \mathbf{x}_0)^{\mathrm{T}} \mathbf{S}_x^{-1} (\hat{\mathbf{x}} - \mathbf{x}_0) + (\mathbf{F}(\hat{\mathbf{x}}) - \mathbf{y})^{\mathrm{T}} \mathbf{S}_\varepsilon^{-1} (\mathbf{F}(\hat{\mathbf{x}}) - \mathbf{y}) \tag{3.5}$$

weighting the deviations with the reciprocal of the corresponding errors. $\mathbf{S}_\varepsilon$ is the covariance matrix of the errors in the spectrum, which should be known. Minimizing χ^2 yields

$$\hat{\mathbf{x}} = \mathbf{G}(\mathbf{y} - \mathbf{K}\mathbf{x}_0) + \mathbf{x}_0 \quad \text{with} \quad \mathbf{G} = \mathbf{S}_x \mathbf{K}^{\mathrm{T}} (\mathbf{K}\mathbf{S}_x\mathbf{K}^{\mathrm{T}} + \mathbf{S}_\varepsilon)^{-1} \tag{3.6}$$

This is the optimal estimation equation for the linear case.

3.2.1 Resolution

Substituting $\mathbf{y} = \mathbf{K}\mathbf{x} + \varepsilon$ in Equation 3.6 gives a relation between the true profile $\mathbf{x}$ and the estimated profile $\hat{\mathbf{x}}$:

$$\hat{\mathbf{x}} = \mathbf{A}\mathbf{x} + (\mathbf{I} - \mathbf{A})\mathbf{x}_0 + \mathbf{G}\varepsilon \tag{3.7}$$

where $\mathbf{A}$ is the so called averaging kernel matrix

$$\mathbf{A} = \mathbf{G}\mathbf{K} \tag{3.8}$$

Let us have a look at the rows of this matrix. We look first at the altitudes where enough information about the mixing ratios is hidden in the spectrum. Here, the rows of the averaging kernel matrix often have a Gaussian shape with a peak at the altitude of the retrieved mixing ratio, see Figure 3.1. Thus, the retrieved volume mixing ratio at a given altitude is a weighted mean of the volume mixing ratios in a finite layer. In addition to this, a constant contribution of the a priori profile is added. However, this contribution is usually small in the altitude range considered here. The term $\mathbf{G}\varepsilon$ describes the error in the profile due to errors in the spectrum.

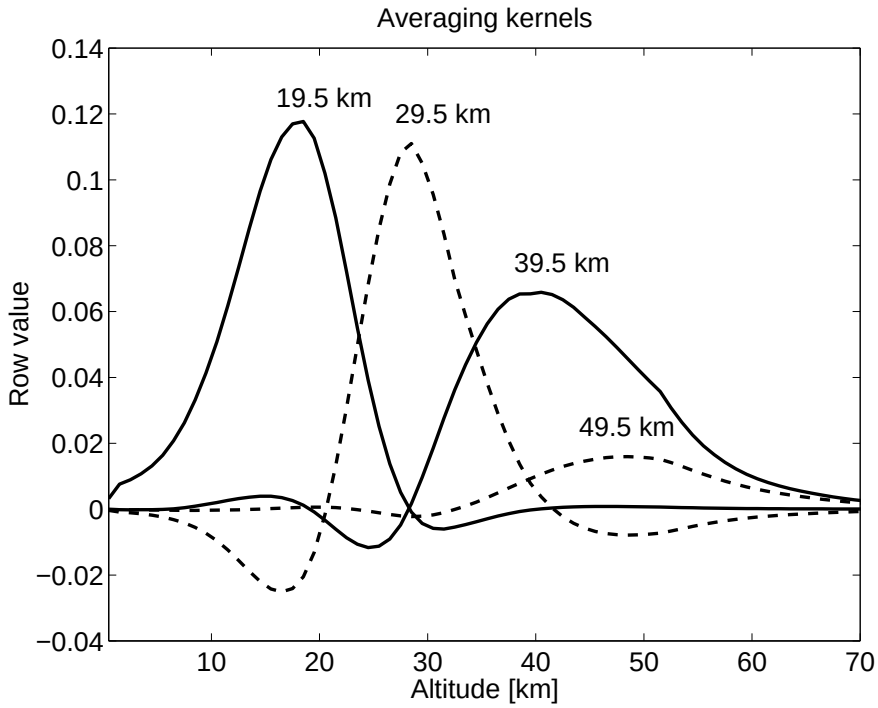

Figure 3.1: Averaging kernels. Typical row values of four different rows (for ozone at 142 GHz). The indices of the rows are indicated by the altitude annotated above the curves.

The shape of the averaging kernels is a measure for the altitude resolution of the retrieval. The broader the kernels are, the worse is the resolution. A straightforward way to define altitude resolution is the response of the retrieval to two delta function peaks in the true profile. The smallest distance where these functions can be distinguished in the estimated profile is the altitude resolution. It is given by the half width of the rows of the kernels. A very similar result is obtained by taking the reciprocal of the diagonal elements of the averaging kernels, since the peak values are a measure for the degrees of freedom per level. Altitude resolution in Figures 3.2 to 3.5 and Tables 3.1 to 3.2 is estimated with this method.

There are altitudes where there is no sufficient information in the spectrum to retrieve mixing ratios. In this altitude range, the second term of Equation 3.7 becomes significant and the estimated profile approaches the a priori values. The altitude range of the retrieval is determined by the sum of the row elements of the kernel. If the sum is near unity, the first term in Equation 3.7 is dominant and the a priori has no contribution. If it is near zero, the profile is dominated by the a priori. Limiting factors for the altitude range are noise, instrumental effects and

the observed bandwidth for low altitudes and Doppler broadening and spectral resolution for high altitudes.

A related topic is the signal-to-noise ratio of the measurement. If we compare the intensity of the line to the measurement noise, we see that small lines are more difficult to retrieve than large lines. It is easier to distinguish the information inherited in the line shape from the noise when the line is larger. Thus, altitude resolution and range are a function of the signal-to-noise ratio. We will see later how we can keep the signal-to-noise ratio at a constant level, which is desirable.

Finally, if we want to compare an independent high resolution measurement to our estimated profile, we have to apply Equation 3.7 to the independent measurement. We obtain a smoothed version of the measurement in our altitude resolution.

3.2.2 Errors

Errors in the estimated profile can be divided in errors originating from the spectrum propagating into the profile, errors in the forward model and errors due to the restricted altitude resolution. We have already seen that the error originating from the spectrum is given by the covariance matrix

$$\mathbf{S}_1 = \mathbf{G}\mathbf{S}_\varepsilon\mathbf{G}^{\mathrm{T}} \tag{3.9}$$

All statistical errors shown in the following were calculated according to this formula. The altitude resolution error has only to be considered if one compares an independent measurement that has not been treated with Equation 3.7 to the estimated profile. If the independent measurement has been adjusted to our altitude resolution, this error is of no interest. It is given by

$$\mathbf{S}_2 = (\mathbf{I}-\mathbf{A})\mathbf{S}_\mathrm{x}(\mathbf{I}-\mathbf{A})^{\mathrm{T}} \tag{3.10}$$

We will not consider this error source in the following since all independent measurements have been convoluted to our altitude resolution. The errors in the forward model can be divided into errors due to simplifications or unknown physics and into errors due to parameters of the model that are not exactly known. The latter error is given by

$$\mathbf{S}_3 = (\mathbf{G}\mathbf{K}_\mathrm{b})\mathbf{S}_\mathrm{b}(\mathbf{G}\mathbf{K}_\mathrm{b})^{\mathrm{T}} \tag{3.11}$$

where $\mathbf{b}$ is the vector of the parameters of the model. $\mathbf{S}_\mathrm{b}$ is the covariance matrix of the parameters, and $\mathbf{K}_\mathrm{b}$ is given by $\partial\mathbf{F}/\partial\mathbf{b}$, which is defined by $K_{\mathrm{b},ij} = \partial F_i(\mathbf{x})/\partial b_j$. Errors in the forward model are difficult to calculate analytically. Thus, we will not present them here and shown errors are a lower limit. However, a study of these errors for an older version of the forward model can be found in [Wohltmann, 1999]. If the error from the spectrum and all the forward model errors from

the old model are combined, the resulting error is much larger than the discrepancies actually observed in comparison with ozone sondes. This is a hint that the covariance matrices $\mathbf{S}_\varepsilon$ and $\mathbf{S}_b$ are quite conservative estimates of the errors and could be minimized in some cases.

3.2.3 Nonlinearities

In general, no linear relationship between $\mathbf{x}$ and $\mathbf{y}$ is given. It is possible to adapt the optimal estimation method to non-linear problems by means of two different methods:

- Newton method: This approach is suitable for slightly non-linear problems.
- Levenberg-Marquardt method: This method is applicable for moderate non-linear problems.

Both methods are iterative. For each of the methods, we linearize $\mathbf{F}(\mathbf{x})$ by expansion to a Taylor series at an appropriate point $\mathbf{x}_0$:

$$\mathbf{y} = \mathbf{F}(\mathbf{x}) + \varepsilon = \mathbf{F}(\mathbf{x}_0) + \mathbf{K}(\mathbf{x} - \mathbf{x}_0) + O(\mathbf{x}^2) + \varepsilon \tag{3.12}$$

The weighting function matrix

$$\mathbf{K} = \frac{\partial \mathbf{F}}{\partial \mathbf{x}}(\mathbf{x}) \tag{3.13}$$

is now dependent on $\mathbf{x}$. Its elements are defined by $K_{ij} = \partial F_i(\mathbf{x})/\partial x_j$. For the Newton method, the model $\mathbf{F}(\mathbf{x})$ is expanded at a point $\hat{\mathbf{x}}_n$ in the n-th iteration and the weighting functions are calculated as

$$\mathbf{K_n} = \frac{\partial \mathbf{F}}{\partial \mathbf{x}}(\hat{\mathbf{x}}_n) \tag{3.14}$$

The estimated $\hat{\mathbf{x}}_{n+1}$ of the next iteration is computed by

$$\begin{aligned} \hat{\mathbf{x}}_{n+1} &= \mathbf{G}_n[(\mathbf{y} - \mathbf{K}_n\mathbf{x}_0) + \mathbf{K}_n\hat{\mathbf{x}}_n - \mathbf{F}(\hat{\mathbf{x}}_n)] + \mathbf{x}_0 \\ \mathbf{G}_n &= \mathbf{S}_x\mathbf{K}_n^T(\mathbf{K}_n\mathbf{S}_x\mathbf{K}_n^T + \mathbf{S}_\varepsilon)^{-1} \end{aligned} \tag{3.15}$$

Compared with Equation 3.6 an extra term giving the difference between the exact and linearized forward model occurs. As an initial point $\hat{\mathbf{x}}_0 = \mathbf{x}_0$ is chosen. The iteration is quit when $\hat{\mathbf{x}}_n$ does not change anymore.

The Levenberg-Marquardt method uses different approaches depending on the distance to the minimum. If the minimum is near, the formula gives the Newton method. If the minimum is far away, the steepest descent method is used, which

steps down a little distance along the steepest gradient of the χ^2 function. A control parameter γ switches continually between the methods:

$$\hat{\mathbf{x}}_{n+1} = \hat{\mathbf{x}}_n + [\mathbf{K}_n^{\mathrm{T}}\mathbf{S}_\varepsilon^{-1}\mathbf{K}_n + (1+\gamma)\mathbf{S}_{\mathrm{x}}^{-1}]^{-1} \\ [\mathbf{K}_n^{\mathrm{T}}\mathbf{S}_\varepsilon^{-1}(\mathbf{y} - \mathbf{F}(\hat{\mathbf{x}}_n)) - \mathbf{S}_{\mathrm{x}}^{-1}(\hat{\mathbf{x}}_n - \mathbf{x}_0)] \tag{3.16}$$

giving the Newton method for $\gamma \to 0$ and the steepest descent method for $\gamma \to \infty$. The value of γ is changed in every iteration step dependent on χ^2:

- If $\chi^2_{n+1} > \chi^2_n$, γ is multiplied by a factor > 1 and $\hat{\mathbf{x}}_{n+1}$ is not updated.
- If $\chi^2_{n+1} < \chi^2_n$, γ is divided by a factor > 1 and $\hat{\mathbf{x}}_{n+1}$ is updated.

Again, the iteration is quit if $\hat{\mathbf{x}}_n$ converges. Since it is not sure that the initial point is near the absolute minimum of χ^2, it is possible to hit only a local minimum with the Levenberg-Marquardt method.

3.3 Retrieval

We will now give an overview over the different retrieval methods and forward models actually used for the four radiometers discussed here. The retrievals have many features in common, so we will not split this section by radiometers, but describe the different features and make special remarks for single radiometers, if necessary. We will begin with some common features like spectrum covariances and a priori values in subsection 3.3.1. The forward models are described in subsection 3.3.2. Table 3.1 and 3.2 give a summary where which feature is used, and Figures 3.2 to 3.5 show some examples for profiles, spectra and altitude resolution for all radiometers. Finally, we introduce a new algorithm to achieve comparable signal-to-noise ratios in the spectra in subsection 3.3.3. The new water vapor retrieval is described in some more detail in section 3.4, where we present a full forward model and a simplified model leading to first results.

3.3.1 General Features

The first choice to be made is which iteration method should be used. All retrievals except for the full water vapor retrieval use the Newton iteration, because they are only slightly non-linear. For the full water vapor model, the Levenberg-Marquardt method has to be used. We have also tried a simple approach for water vapor with the Newton method using only the innermost channels of the spectrum and the totalpower spectra. The next issue is choosing the parameters that should be retrieved and the parameters that should be constant or calculated in the forward

Model	22 GHz (full)	22 GHz (simple)
Method	Levenberg-Marquardt	Newton
Integration	Reference	Totalpower
A priori	Sondes (troposphere), climatology (stratosphere)	
Spectrum covariance	Noise, baseline	Noise, baseline
Altitude resolution	–	15–20 km
Altitude range	–	20–42 km
Line form	Van Vleck Weisskopf, mirror line	Van Vleck Weisskopf
Line broadening	Self, Foreign, Doppler	Foreign, Doppler
Line shift	Self, Foreign (retrieved)	–
Continuum	Cruz-Pol	–
Troposphere	Direct calculation	Two layer
Tropospheric bias	–	retrieved
Cosmic radiation	calculated	–
Window	calculated	–
Sidebands	only band pass	only band pass
Standing waves	retrieved	retrieved
Offset	optional	–
Slope	optional	retrieved
Absorber plate	calculated/retrieved	–
Spectrum convolution	calculated	calculated

Table 3.1: Retrieval models

model. Retrieved parameters include the mixing ratios (all models), the brightness temperature of the tropospheric bias (all totalpower measurements), amplitudes of standing waves (all models), slope (optionally) and offset (optionally). The mixing ratios are retrieved on a 1 km grid reaching from 0.5 to 100.5 km. For simplicity, the same grid is used for the retrieval and the radiative transfer calculation. Again, the water vapor retrieval is an exception. Here, we use a finer grid in the radiative transfer in the moist troposphere, since the opacity of the layers should be small to obtain a correct integration.

Input parameters that are constant or calculated in the forward models are pressure and temperature, the wave numbers of the standing waves, instrument parameters (like local oscillator frequency, path length difference of the interferometer, relative conversion modes, hot and cold load temperatures), line parameters, measurement angle, window transmission, outdoor temperature and some others.

Model	110 GHz	142 GHz	204 GHz
Method	Newton	Newton	Newton
Integration	Totalpower	Totalpower	Reference
A priori	Sondes	Sondes	Model
Spectrum covariance	Noise, T, ν, baseline	Noise, T, ν, baseline	Noise, baseline
Altitude resolution	12–14 km	9–12 km	10–15 km
Altitude range	20–44 km	12–46 km	14–45 km
Line form	Van Vleck Weisskopf	Van Vleck Weisskopf	Van Vleck Weisskopf
Line broadening	Foreign, Doppler	Foreign, Doppler	Foreign, Doppler
Troposphere	Two layer	Two layer	Parrish
Tropospheric bias	retrieved	retrieved	–
Cosmic radiation	calculated	calculated	–
Window	calculated	calculated	–
Sidebands	only band pass	6 bands	only band pass
Standing waves	retrieved	retrieved	retrieved
Offset	–	–	retrieved
Slope	retrieved	retrieved	retrieved
Absorber plate	–	–	calculated
Second LO	–	optional	–
Spectrum convolution	calculated	calculated	calculated

Table 3.2: Retrieval models II

Temperature and Pressure

Pressure and temperature are taken from analyses of the National Center for Environmental Prediction (NCEP) and the European Center for Medium Range Weather Forecast (ECMWF). Data gaps in the NCEP data are filled up with ECMWF data. Temperature in the upper atmosphere is taken from a climatology and pressure is calculated from the hydrostatic equilibrium here.

Joined Channels

The optimal estimation method involves the inversion of a matrix of dimension $n \times n$, where n is the number of frequency channels. Since this is a very time consuming operation, it is efficient to reduce the number of frequency channels

before the inversion. Thus, we average the spectrometer channels into frequency bins that are very small in the line center, where most of the information is stored, and get larger at the line wings. All following operations are performed with the reduced spectrum. After the inversion the last forward spectrum is interpolated back to the original frequency grid to enable a comparison with the measured spectrum.

Spectrum Covariance

The spectrum covariance should comprise all errors that are apparent in the spectrum. Considered error sources are noise, and for the totalpower spectra, errors in the temperature measurements and frequency calibration errors. The noise on the spectrum is calculated from the variation of the brightness temperatures in adjacent channels. The result should be comparable to the temporal variation in one channel, which mathematically defines the noise. The noise in a joined channel is given by

$$\sigma = \frac{1}{\sqrt{N}} \frac{1}{\sqrt{2}} \left(\frac{1}{N-1} \sum_{k=1}^{N-1} y_{k+1} - y_k \right)^{1/2} \tag{3.17}$$

where N is the number of spectrometer channels in a joined channel and y_k is the k-th spectrometer channel. The factor $1/\sqrt{2}$ accounts for the combination of the two measurements y_k and y_{k+1}. Frequency and temperature calibration errors are derived by an error analysis of the totalpower or reference beam formulas. Finally, a constant value is added to the diagonal of the spectrum covariance to account for leftover statistical and unknown systematic error sources. Although this ad hoc error is unsatisfactory, it is necessary for the convergence of the optimal estimation method.

A Priori Values

The mean and covariance of an independent measurement series are needed to calculate the a priori profile and covariance. Where no measurement series is available, a climatology has to be used. The tropospheric part of the a priori profile and covariance of the water vapor radiometer is inferred from relative humidities measured by several 100 sondes launched in Ny-Ålesund. In the stratosphere, a climatology from the HALOE (Halogen Occultation Experiment) and MLS (Microwave Limb Sounder) instruments on board the UARS satellite is used [Randel et al., 1998]. The a priori values of the ozone radiometer in Spitsbergen were derived from the mean and standard deviation of measurements of ozone sondes launched in Ny-Ålesund. For the radiometer in Bremen, no local sonde measurements are available. It is planned to use a weighted mean of sondes launched in

nearby places like Hohenpeissenberg, Germany, or Uccle, Belgium, here. In the moment, a climatology is used. The a priori profile of the ozone radiometers is further modified by calculating the altitude of the tropopause and setting mean and covariance to tropospheric values below this altitude. The chlorine monoxide a priori profile is derived from a climatology for the upper peak of the profile. The a priori for the lower stratosphere is set to zero to avoid any bias in the retrieved mixing ratios.

3.3.2 Forward Model Features

Aim of the forward model $\mathbf{F}(\mathbf{x})$ is an accurate simulation of the spectrum measured by the instrument. We not only have to consider the atmospheric spectrum, but also the integration method (e. g. the totalpower method) and instrumental features. If we have taken into account all effects that can cause a detectable change in the spectrum, we obtain a single complicated function $\mathbf{F}(\mathbf{x})$. We will describe all parts of this function in the next subsections.

Related to the forward model is the calculation of the weighting functions $\mathbf{K} = \partial\mathbf{F}/\partial\mathbf{x}$. All derivatives needed for the weighting functions are calculated analytically. Most retrievals calculate the derivatives numerically, since calculating the derivatives manually can be quite tedious. However, it has only to be done once and speeds up the retrieval enormously.

Spectral Lines

For all lines, the Van Vleck Weisskopf line shape is used, see Equation 2.19. The mirror line is only considered for water vapor, since it is truly negligible for the other spectra. Line intensities are calculated according to Equation 2.21. Most of the line parameters needed are taken from [Janssen, 1993]. Table 3.3 to Table 3.6 give an overview over the parameters used.

As has been stated already, the Voigt line shape can only be calculated numerically. Since Matlab is an interpreter language, speed is an important issue. It turned out that the algorithm of Drayson [1976], which was used formerly to compute the Voigt line shape, was unacceptably slow. Therefore a new algorithm developed by Humlicek [1979] and optimized for speed by Kuntz [1997] was chosen. It computes the following expression

$$F_{\mathrm{V}}(\nu,\nu_i) = \frac{\sqrt{1/\pi}}{\gamma_{\mathrm{D}}} K\left(\frac{\nu-\nu_i}{\gamma_{\mathrm{D}}}, \frac{\gamma_{\mathrm{C}}}{\gamma_{\mathrm{D}}}\right) \tag{3.18}$$

where the function K is given by

$$K(x,y) = \mathrm{Re}\left(\frac{i}{\pi}\int_{-\infty}^{\infty}\frac{\exp(-t^2)}{(x+iy)-t}\right) \tag{3.19}$$

The main advantage of the algorithm is that all frequencies can be calculated independently, allowing Matlab to perform some optimizations.

For the 22 GHz water vapor radiometer, only one line has to calculated. The models for the ozone radiometers at 110 GHz and 142 GHz both consider two lines. For the chlorine monoxide radiometer, it turned out to be sufficient to perform the forward calculation only for a cluster of nine lines of the main isotope of chlorine monoxide centered at 204 GHz. In the old model, more lines were considered.

Radiative Transfer

The power received by the instrument is described by the Schwarzschild equation 2.9. The integral is simplified by transforming it to an integral over the transmission χ, where χ is given by

$$\chi(z,\nu) = \exp\left(-\int_{z_0}^{z}\alpha(z',\nu)\,\mathrm{d}z'\right) \tag{3.20}$$

so that the Schwarzschild equation gives

$$T_{\mathrm{B,strat}}(z_0,\nu) = -\int_{\chi(z_0,\nu)}^{\chi(z_\infty,\nu)} T_{\mathrm{B}}^{\mathrm{black}}\left(T\left(z(\chi')\right),\nu\right)\mathrm{d}\chi' \tag{3.21}$$

The integral is discretized with the trapezoid formula. While the application of the trapezoid formula to the forward model is quite easy, the evaluation of the weighting functions is significantly more difficult. A detailed treatment can be found in [von König, 2001]. The integration itself relies on a recursive algorithm, which considerably speeds up computation time, see [Sinnhuber, 1999]. Finally, the curvature of the earth is considered by Equation 2.10.

Tropospheric Absorption

The atmospheric spectrum of all radiometers is composed of a tropospheric bias and the observed lines from the stratosphere. The tropospheric bias, which is almost frequency independent, originates from line wings of adjacent lines and from

Property	Value
Frequency ν_i	22.23508 GHz
Wavelength λ_i	1.35 cm
Pressure broadening w	2.81 MHz/hPa
Pressure broadening x	0.69
Self broadening w_s	13.2 MHz/hPa$^{(1)}$ 13.49 MHz/hPa$^{(2)}$
Self broadening x_s	$1^{(1)}$
Frequency shift d	-0.9 MHz/hPa$^{(1)}$ -1.035 MHz/hPa$^{(2)}$
Reference temperature T_0	300 K
Line strength S at T_0	0.1272×10^{-17} m^2 Hz
Line strength property b	2.143
Fundamental modes T_l	2294 K, 5262 K, 5404 K
Isotopic ratio a	0.9973
Molecular weight m	18 u

Table 3.3: Properties of the water vapor transition at 22 GHz, from [Janssen, 1993], except for $^{(1)}$[Mrowinski, 1970], $^{(2)}$[Liebe and Dillon, 1969]

Property	Value	Value
Frequency ν_i	109.55933 GHz	110.83604 GHz
Wavelength λ_i	2.7 mm	2.7 mm
Pressure broadening w	2.22 MHz/hPa	2.37 MHz/hPa
Pressure broadening x	0.76	0.73
Reference temperature T_0	300 K	
Line strength S at T_0	0.1032×10^{-16} m^2 Hz	0.3724×10^{-16} m^2 Hz
Line strength property b	0.911	0.093
Fundamental modes T_l	1008 K, 1499 K, 1587 K	
Isotopic ratio a	0.9928	
Molecular weight m	48 u	

Table 3.4: Properties of the ozone transition at 110 GHz, from [Janssen, 1993]

Property	Value	Value
Frequency ν_i	142.17504 GHz	144.91936 GHz
Wavelength λ_i	2.1 mm	2.1 mm
Pressure broadening w	2.50 MHz/hPa	2.29 MHz/hPa
Pressure broadening x	0.70	0.76
Reference temperature T_0	300 K	
Line strength S at T_0	0.7388×10^{-16} m^2 Hz	0.2772×10^{-16} m^2 Hz
Line strength property b	0.231	0.438
Fundamental modes T_l	1008 K, 1499 K, 1587 K	
Isotopic ratio a	0.9928	
Molecular weight m	48 u	

Table 3.5: Properties of the ozone transition at 142 GHz, from [Janssen, 1993]

Property	Value
Frequency ν_i	204.2701 GHz – 204.3626 GHz
Wavelength λ_i	1.5 mm
Pressure broadening w	3.49 MHz/hPa
Pressure broadening x	0.75
Reference temperature T_0	300 K
Line strength S at T_0	0.9252×10^{-18} m^2 Hz – 0.8542×10^{-15} m^2 Hz
Line strength property b	0.084
Fundamental mode T_l	1212 K
Electronic mode T_e	458.3 K
Isotopic ratio a	0.7559
Molecular weight m	51 u

Table 3.6: Properties of the chlorine monoxide transition at 204 GHz, from [Janssen, 1993]

continuum emission terms. The stratospheric lines are additionally attenuated by the tropospheric species. If we assume that the bias temperature is constant over the frequency range of the instrument, we can write

$$T_{\mathrm{B,atm}} = T_{\mathrm{B,strat}} \chi_{\mathrm{trop}}(T_{\mathrm{B,trop}}) + T_{\mathrm{B,trop}} \tag{3.22}$$

We will refer to this formula as a two layer model. $T_{\mathrm{B,trop}}$ is the tropospheric bias, $T_{\mathrm{B,strat}}$ the stratospheric emission and

$$\chi_{\mathrm{trop}} = \exp\left(- \int_0^{z_{\mathrm{T}}} \alpha(z', \nu)\, dz' \right) \tag{3.23}$$

is the tropospheric transmission, where z_{T} is the altitude of the tropopause. Since the bias is not completely independent of frequency, an additional slope is fitted to the spectra. The tropospheric transmission is in good approximation a function of the bias temperature. Thus, it is calculated from the bias temperature in the forward model.

The bias temperature is used as a retrieved parameter in the ozone models and the simple water vapor model for several reasons. On the one hand, it can easily be retrieved, because it is more or less the brightness temperature at the lowermost frequency channel. On the other hand, it is needed to calculate some other parameters in the model (most importantly the tropospheric transmission, but also the higher side bands). One could argue that the bias temperature could be set to the temperature of the leftmost channel before the retrieval, but in general this temperature will not be identical with the bias temperature due to standing waves or higher side bands.

The tropospheric transmission, which is needed to scale the line, is calculated as a function of the bias. For the determination of this function, atmospheric spectra and absorption coefficients have been calculated from the temperature, pressure and water vapor data of several 100 sondes launched at Ny-Ålesund. Calculations were performed by the general microwave forward model of the Institute of Environmental Physics, ARTS [Bühler et al., 2002]. The resulting tropospheric transmissions were plotted versus the computed bias temperatures and fitted to a polynomial. Since bias temperature and transmission are both a function of temperature, pressure and water vapor profile, it is quite surprising in the first moment that the scatter in the relationship between them is small enough to fit a polynomial. However, if the temperature of the troposphere $T_{\mathrm{B}}^{\mathrm{black}}$ and α are assumed to be constant, which is approximately true, it is easy to show that

$$\chi_{\mathrm{trop}} = 1 - T_{\mathrm{B,trop}} / T_{\mathrm{B}}^{\mathrm{black}} \tag{3.24}$$

The water vapor and chlorine monoxide models treat the troposphere differently. The full water vapor retrieval computes the mixing ratios of the troposphere explicitly from the information in the spectrum. Thus, no scaling of the stratospheric line is needed, because it is already included in the radiative transfer calculation. The chlorine monoxide retrieval uses the method of Parrish et al. [1988] to calculate the pure stratospheric line before the retrieval. A detailed description of the method is given in the water vapor model description in section 3.4.3 (with an additional explanation why this method is not applicable for water vapor).

Cosmic Radiation

Cosmic background radiation behaves like black body radiation with a temperature of 2.7 K and propagates through the atmosphere. It is simply added to the stratospheric radiation:

$$T_{\mathrm{B,strat}} \rightarrow T_{\mathrm{B,strat}} + T_{\mathrm{B,cosmic}} \tag{3.25}$$

It has been assumed here that the stratospheric transmission is near 1.

Window

The styrofoam window of the laboratory attenuates the atmospheric radiation and emits its own black body radiation:

$$T_{\mathrm{B,a}} = \chi_{\mathrm{w}} T_{\mathrm{B,atm}} + (1-\chi_{\mathrm{w}}) T_{\mathrm{B,w}} \tag{3.26}$$

Here, χ_{w} is the transmission of the window and $T_{\mathrm{B,w}}$ its temperature. The temperature is calculated as the mean of outdoor and room temperature. The transmission of the window is set to 0.99.

Higher Side Bands

As we have seen, the power received by the mixer is composed of different frequency bands superimposed on each other. In most cases, the radiation of the higher side bands is expected to be negligible. However, at least for the ozone radiometer in Spitsbergen, this is not the case [Langer, 1995]. The first three lower and upper side bands are therefore explicitly considered:

$$P = \sum_{n=\pm1,\pm2,\pm3} L(\nu_n) T_{\mathrm{B}}(\nu_n) \tag{3.27}$$

The power P is additionally divided by k_{B} to obtain the corresponding brightness temperature. The proportionality factors are given by $L(\nu_n) = \Lambda(\nu_n) D(\nu_n)$, where

the Λ are the conversion modes and D is the band pass of the interferometer. Thus the conversion modes, the path length difference of the interferometer and the local oscillator frequency have to be known. Conversion modes are taken from Langer [1995] and the path length difference is measured at the instrument. The brightness temperatures in the higher bands are calculated as a function of frequency and the bias temperature of the spectra. Again, spectra of all side bands were calculated by the general forward model ARTS, for a set of several 100 sondes. The resulting brightness temperatures were plotted versus the computed bias temperature and fitted to a polynomial for all intermediate frequencies. This polynomial is then used in the forward model to obtain the brightness temperatures.

Even if all higher side bands have a conversion mode of zero, which is assumed for the water vapor and chlorine monoxide radiometers and the ozone radiometer in Bremen due to a lack of measurements, at least the band pass of the interferometer has to be considered:

$$P = \Lambda(\nu_1) D(\nu_1) T_{\mathrm{B}}(\nu_1) \tag{3.28}$$

In case of the ozone radiometer in Bremen, it has to be remarked that the lower side band ν_{-1} is used for the signal. Thus, frequencies are descending from high to low through the channels, which has to be taken into account when multiplying the interferometer bandpass.

Standing Waves

Multiple reflections occurring between the various optical elements can cause interference effects in the spectra. For small reflection indices, the attenuation in the spectral power can be expressed by a cosine according to the well known formula of Fabry-Pérot:

$$P = P_0 \left(1 - \frac{2 r_1 r_2}{(1 - r_1 r_2)^2} + \frac{2 r_1 r_2}{(1 - r_1 r_2)^2} \cos(4\pi n d \nu / c) \right) \tag{3.29}$$

Here, the incoming power P_0 is attenuated to P. r_1 and r_2 are the reflection indices of the optical elements. n is the refraction index of air, d is the distance of the reflecting elements, ν the frequency of the radiation and c the speed of light. The wave length Λ of the standing wave can be expressed by the distance of the two elements causing the wave:

$$d = \frac{c}{2n\Lambda} \tag{3.30}$$

Standing waves in the forward model are expressed by a linear combination of a sine and a cosine to account for an eventual phase shift Φ:

$$C \cos(2\pi\nu/\Lambda + \Phi) = A \cos(2\pi\nu/\Lambda) + B \sin(2\pi\nu/\Lambda) \tag{3.31}$$

Retrieved parameters are A and B. The wave length of the standing wave Λ has to be known in advance. While standing waves with a short wavelength are easily detectable and orthogonal to the measurement, standing waves with wave lengths similar to the bandwidth of the radiometer can pose great problems, since they influence the mixing ratios and cannot readily be seen.

Offset and Slope

The slope originating from the frequency dependent part of the tropospheric emission should be a function of the bias temperature. However, some effects can cause an offset or a slope that cannot be calculated from known parameters. Examples are a change of weather conditions during a reference beam measurement or rain. Hence, a slope and an offset can be fitted optionally in the forward models. However, since slope and offset can disturb the retrieval of other parameters, they should be used with care.

Frequency Resolution

The frequency resolution of the instrument is coarser than the frequency difference between the channels of the spectrometer, as a result of the finite width of the laser beam. The distribution of the power that leaks into neighboring frequency channels has a Gaussian shape. This has to be considered in the forward model. Mathematically, the resulting spectrum is a convolution of the original spectrum and the Gaussian curve:

$$(s \otimes g)(\nu) = \int_{-\infty}^{\infty} s(\nu - \nu') g(\nu') \, \mathrm{d}\nu' \tag{3.32}$$

Here, s is the spectrum and g the Gaussian curve. In the forward model, the convolution is performed directly by approximating the integral by a sum. The standard approach to use the convolution theorem and a Fourier transformation is slower here, because the Gaussian curve is only significantly different from zero for about 10 channels. The convolution of the spectrum implies a convolution of the weighting functions, which is only done where the convoluted spectrum is significantly different from the original spectrum for performance reasons.

Opacity of Absorber Plate

The opacity of the absorber plate can be retrieved optionally in the water vapor and chlorine monoxide models. Since its retrieval is not orthogonal to the retrieval of other parameters, it should be used with care. The opacity of the plate can easily be measured by observing the cold load with and without the plate in the path of

the beam. Opacity has been measured in the past, but instead of the cold load, the atmosphere was taken as the radiation source, without measuring its brightness temperature but estimating it from ground temperature. The errors introduced by this method were so large, that the retrieval has been given the possibility to retrieve the opacity, until new measurements of the cold load are available.

Second Local Oscillator

The second local oscillator in the intermediate frequency chain is not only passing the signal side band to the spectrometer, but also the second lower side band, due to a design flaw. Although the conversion mode of this side band is so small that no superimposed spectrum could be detected on the final spectrum for the spectrometer normally in use, a replacement spectrometer used for some months showed clearly a mirror image of the ozone line. For this reason, a mirror spectrum derived from the forward calculation of the line can be added to the forward spectrum. The added spectrum is scaled by a retrieved factor. In the moment, this is only implemented for the ozone radiometer in Spitsbergen, since it turned out that the effect on mixing ratios was rather small.

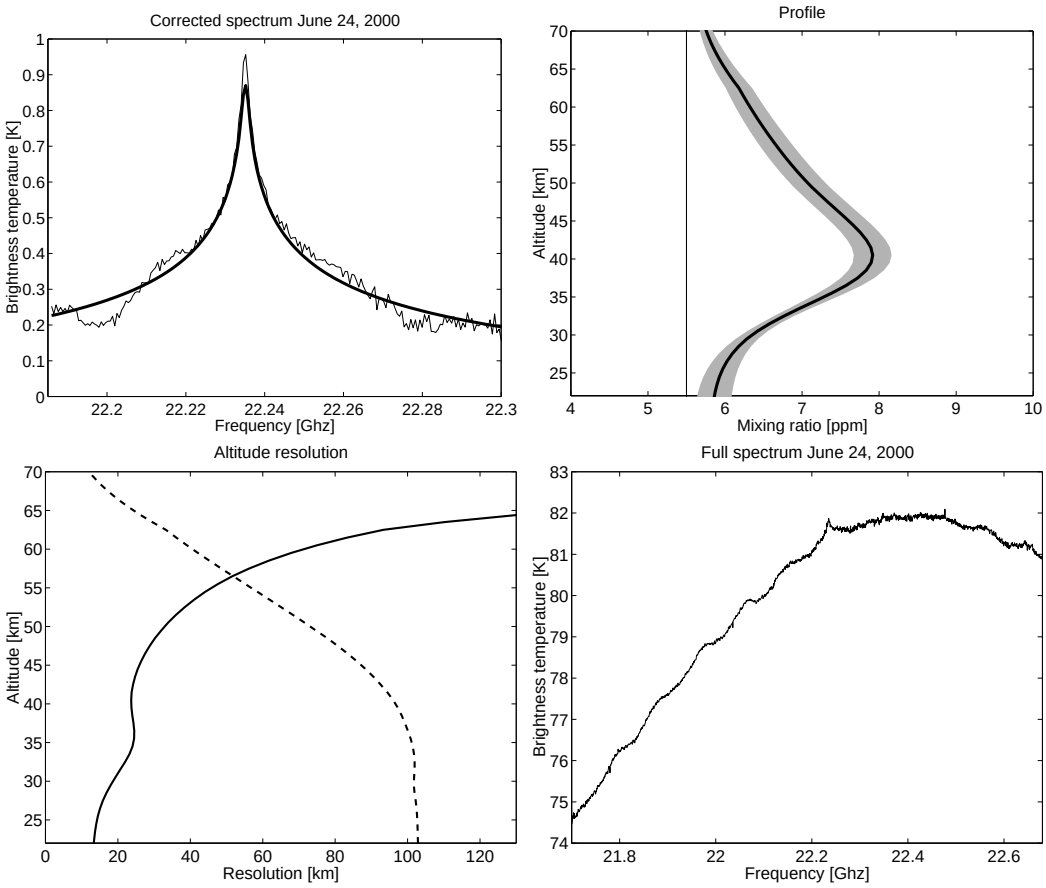

Figure 3.2: Water vapor spectrum and profile. Upper left: Innermost 200 channels of the measured spectrum, corrected for the troposphere (thin line), and forward calculation (thick line). Upper right: Retrieved profile (thick line, with error bars) and a priori profile (thin line). Lower left: Altitude resolution (solid line) and sum of the averaging kernel rows (dashed line), multiplied by 100. Lower right: Full measured spectrum.

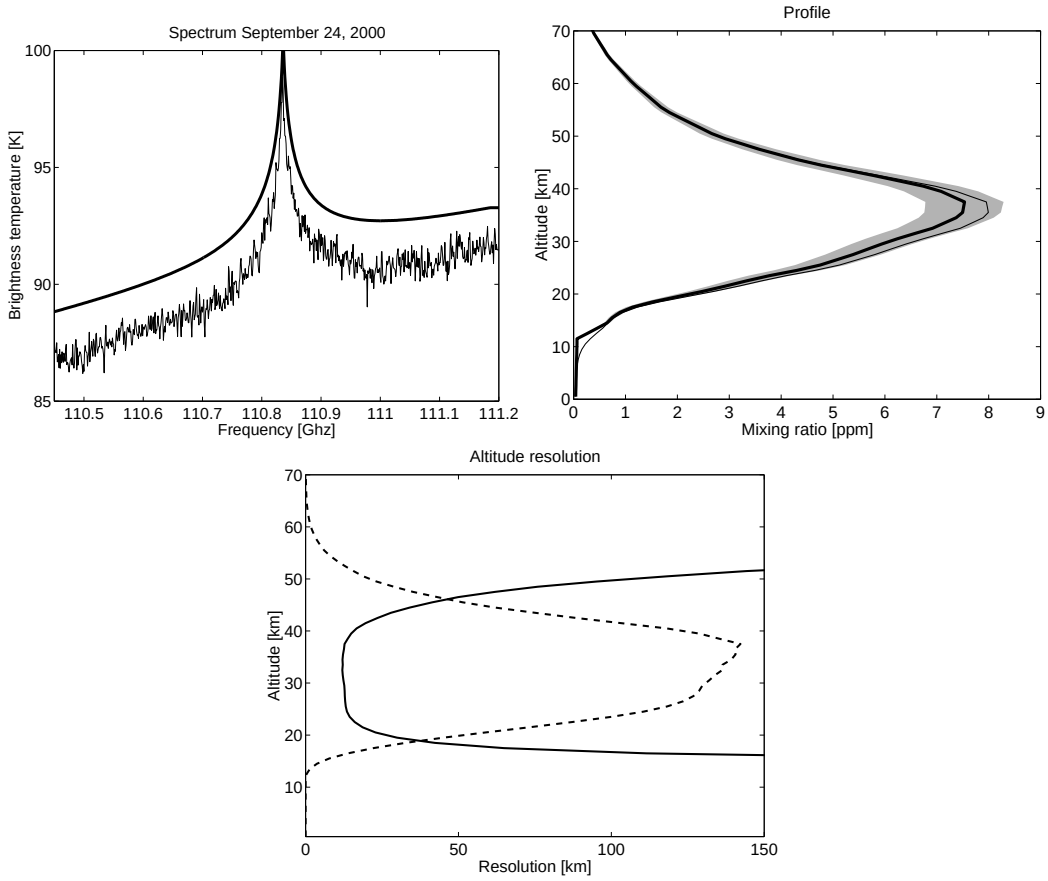

Figure 3.3: Ozone spectrum and profile for the 110 GHz radiometer. Upper left: Measured spectrum (thin line) and forward calculation (thick line). Upper right: Retrieved profile (thick line, with error bars) and a priori profile (thin line). Below: Altitude resolution (solid line) and sum of the averaging kernel rows (dashed line), multiplied by 100.

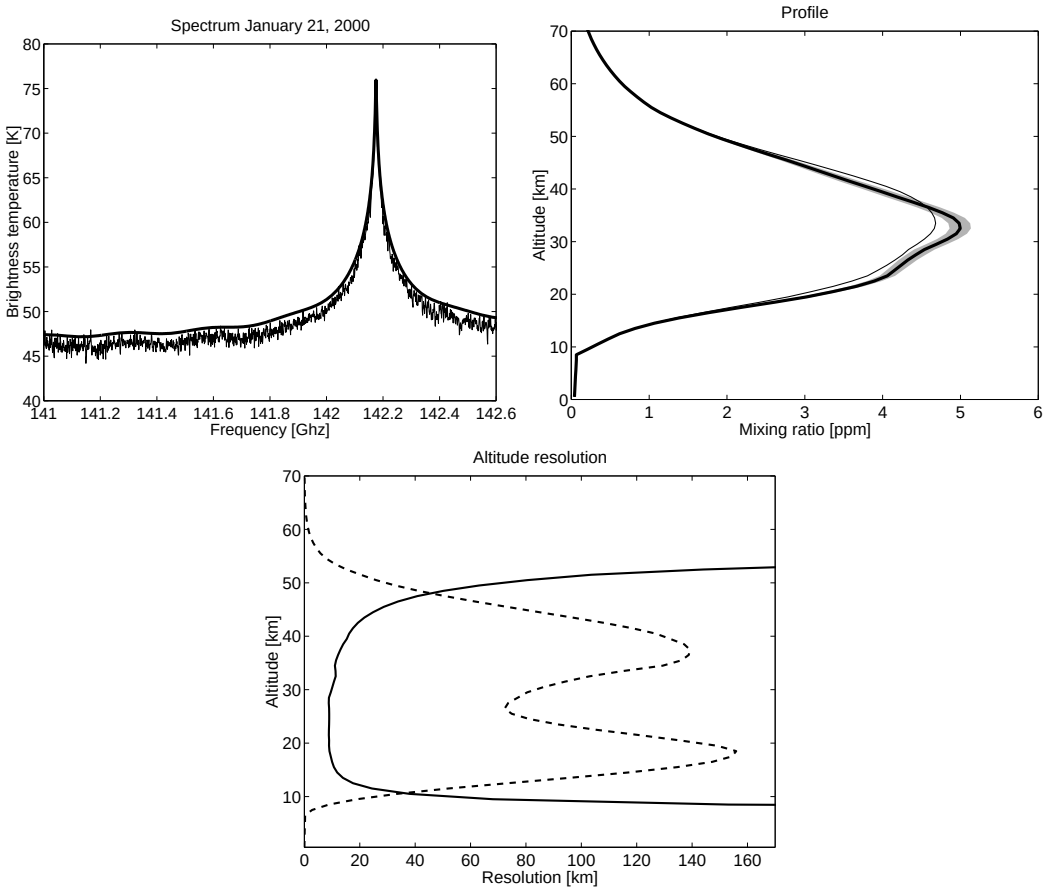

Figure 3.4: Ozone spectrum and profile for the 142 GHz radiometer Upper left: Measured spectrum (thin line) and forward calculation (thick line). Upper right: Retrieved profile (thick line, with error bars) and a priori profile (thin line). Below: Altitude resolution (solid line) and sum of the averaging kernel rows (dashed line), multiplied by 100.

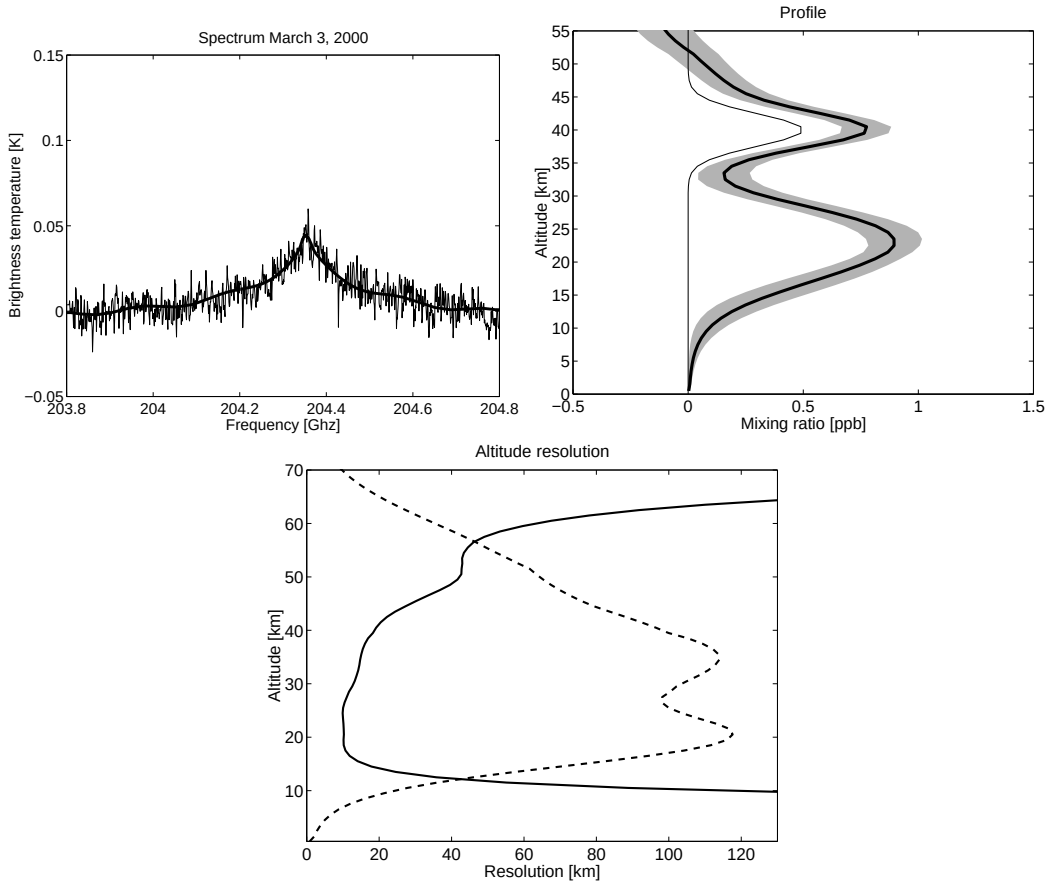

Figure 3.5: Chlorine monoxide spectrum and profile Upper left: Measured spectrum (day-night difference, thin line) and forward calculation (thick line). Upper right: Retrieved profile (thick line, with error bars) and a priori profile (thin line). Below: Altitude resolution (solid line) and sum of the averaging kernel rows (dashed line), multiplied by 100.

3.3.3 Moist Weather Conditions

A new algorithm has been developed to treat spectra that were measured under moist weather conditions, as they often occur in the Arctic summer. One of the disadvantages of the optimal estimation method is the dependence of the profile quality on weather conditions. The a priori contribution is rising for bad weather conditions, while the altitude resolution is going down. It would be desirable to get profiles with the same properties regardless of the situation. Based on an algorithm developed by Langer [1999], a new method has been implemented successfully in the ozone retrievals.

The idea of the algorithm is to increase the information content of the spectra at the expense of the integration time. In bad weather conditions, the signal-to-noise ratio decreases due to the increasing attenuation of the line by tropospheric water vapor. While the noise remains unchanged, the line is declining. If the spectra are integrated to keep their signal-to-noise ratio constant, the averaging kernels and hence the altitude resolution and a priori contribution do not change anymore.

If the forward model is strictly linear, it is possible to give an intuitive expression for the resulting profile. It can easily be shown, that the profile $\bar{\mathbf{x}}$ resulting from the inversion of the mean $\bar{\mathbf{y}}$ of the spectra is a mean over the profiles corresponding to the discrete spectra:

$$\mathbf{K}\mathbf{x}_i = \mathbf{y}_i \Rightarrow \mathbf{K}\bar{\mathbf{x}} = \bar{\mathbf{y}} \tag{3.33}$$

The discrete spectra and profiles are denoted with $\mathbf{y}_i$ and $\mathbf{x}_i$. In the following we assume a simple model of our spectrum:

$$T_\mathrm{B} = \chi_\mathrm{trop} T_\mathrm{B,strat} + T_\mathrm{B,trop} + \sigma \tag{3.34}$$

where $T_\mathrm{B,strat}$ is the ozone spectrum, χ_trop is the transmission of the troposphere, $T_\mathrm{B,trop}$ is the tropospheric bias and σ is the measurement noise. Since we know χ_trop and $T_\mathrm{B,trop}$ in advance, we can linearize the spectrum by

$$T_\mathrm{B,mean} = \frac{T_\mathrm{B} - T_\mathrm{B,trop}}{\chi_\mathrm{trop}} = T_\mathrm{B,strat} + \frac{\sigma}{\chi_\mathrm{trop}} \tag{3.35}$$

Although the forward model is linear now, the measurement noise has been amplified by χ_trop^{-1}. If we compute the mean

$$\bar{T}_\mathrm{B,mean} = \frac{1}{\sum_i t_i} \sum_i T_{\mathrm{B,strat},i} t_i + \frac{1}{\sum_i t_i} \sqrt{\sum_i \left(\frac{\sigma_i t_i}{\chi_{\mathrm{trop},i}} \right)^2} \tag{3.36}$$

with t_i as the integration time of measurement i, the number of measurements we need to obtain a tolerable signal-to-noise ratio grows unacceptably large. Thus,

we use another approach. We assume that the ozone mixing ratio does not change significantly during the integration time we need for a tolerable signal-to-noise-ratio. If we correct the spectra only for the bias

$$T_{\mathrm{B,mean}} = T_{\mathrm{B}} - T_{\mathrm{B,trop}} = T_{\mathrm{B,strat}}\chi_{\mathrm{trop}} + \sigma \tag{3.37}$$

and calculate a weighted mean with transmission as a weighting factor

$$\bar{T}_{\mathrm{B,mean}} = \frac{\frac{1}{\sum_i t_i}\sum_i T_{\mathrm{B,strat},i}\chi_{\mathrm{trop},i}t_i + \frac{1}{\sum_i t_i}\sqrt{\sum_i (\sigma_i t_i)^2}}{\frac{1}{\sum_i t_i}\sum_i \chi_{\mathrm{trop},i}t_i} \tag{3.38}$$

the result is as desired. The expression reduces to $\bar{T}_{\mathrm{B,mean}} = T_{\mathrm{B,strat}}$ when we assume a constant mixing ratio, and noise is much less amplified.

3.4 Water Vapor, Spitsbergen

In addition to the existing retrieval software for ozone and chlorine monoxide, a forward model and inversion algorithm had to be developed for the new water vapor radiometer. Although the 22 GHz line is one of the more prominent lines in the microwave spectrum, it turned out to be quite difficult to develop a proper retrieval algorithm. In fact, it was not possible to retrieve any reliable information from the full spectra yet. However, a simplified approach using only the inner 200 channels of the spectrum turned out to be promising and gave first preliminary results. Here we used totalpower spectra that were measured as a test on June 24, 2001. The full model was only operated with the reference beam spectra so far.

3.4.1 A Simple Approach

We will see in the next sections that the retrieval of the full water vapor spectrum is a challenging and error-prone task. However, most of the problems are negligible when we only regard the part of the line originating from the stratosphere. Therefore, we have created new spectra from the innermost 200 channels (corresponding to about 100 MHz) of the original spectra. Pressure broadening allows the retrieval of profile information down to 20 km for these spectra. The tropospheric bias is considered by application of the two layer model, which was also used for the ozone spectra. Additionally, a slope and standing waves are retrieved. Line calculation is the same as for the full model, with the exception of frequency shift and self broadening. Instead of the logarithmic mixing ratios described later, the usual mixing ratios are used. A constant mixing ratio of 5.5 ppm is taken as a priori profile.

We have used the only 19 totalpower spectra ever measured with the water vapor radiometer to test the model. In a first step, we retrieve a profile for every single of the spectra, all measured with about 1 hour of integration time on June 24, 2001. The scatter between the profiles is unrealistic, probably caused by a standing wave with a wave length of some 10 MHz, which is just about the typical half width of the line in the stratosphere. Therefore, we apply a second step. Here, we average all totalpower spectra after scaling them with the atmospheric transmission retrieved in the first step and subtracting the slope and bias temperature. This procedure should give the average stratospheric line, see section 3.3.3. The profile obtained from this line is shown in Figure 3.2, together with a single original spectrum and the integrated and corrected spectrum. It is evident that the standing wave is still not suppressed, thus the profile has to be considered preliminary. A comparison with profiles in e. g. [Nedoluha et al., 1995] or [Peter, 1998] shows that the general shape of the profile is reasonable, but that the mixing ratios seem to be overestimated.

3.4.2 Logarithmic Retrieval

We will come to the full model now. The main drawback for the inversion is the exponential decrease of the water vapor mixing ratio with altitude. Mixing ratios may vary between 3 ppm and several 1000 ppm. Therefore all calculations are carried out with the logarithm of the mixing ratio. This is a very effective way of canceling large artificial oscillations in the profile, because negative mixing ratios are explicitly forbidden. Thus, the large contribution in brightness temperature of a large positive oscillation in the profile cannot be canceled out by a large negative oscillation in the radiative transfer equation. Although the inversion would not yield any sensible results without logarithmic mixing ratios, they lead to some other unwanted problems, which are explained in the following.

Every occurrence of the mixing ratio $\mathbf{x}$ in the forward model has to be replaced with $\exp(\mathbf{l})$, where $\mathbf{l}$ is the logarithm of the mixing ratio as the new retrieved parameter. Obviously, this causes the forward model to become very non-linear. Consequently, the Levenberg-Marquardt method has to be used by the inversion, leading to slow convergence and non optimal solutions. The weighting functions have to be modified as well, $\partial\mathbf{F}(\mathbf{x})/\partial\mathbf{x}$ has to be replaced by

$$\frac{\partial\mathbf{F}(\mathbf{x})}{\partial\mathbf{x}}\frac{\partial\mathbf{x}}{\partial\mathbf{l}} = \frac{\partial\mathbf{F}(\exp(\mathbf{l}))}{\partial(\exp(\mathbf{l}))}\exp(\mathbf{l}) \tag{3.39}$$

The a priori profile and the a priori covariance have to be converted to the logarithm. This is straightforward when an independent measurement series is available. However, it is much more difficult to convert a given mean and covariance

from a climatology to their logarithmic equivalents. First of all, a probability distribution has to be assumed. We have two possibilities here. We can assume a normal distribution for the mixing ratios. If the covariance is large in comparison to the mean, the normal distribution has non negligible probabilities for negative values, which is unphysical. Unfortunately, this is just the case for water vapor, implying that the water vapor mixing ratios are not normally distributed. The second possibility is to assume a lognormal distribution for the mixing ratios, so that the logarithm of the mixing ratios is normally distributed. It is shown in Appendix 3.B that if the mean is much larger than the standard deviation, $(\mathbf{x}_0)_i \gg \sqrt{(\mathbf{S}_\mathrm{x})_{ii}}$, the logarithmic mean is the logarithm of the old mean for both cases

$$\mathbf{l_0} \approx \ln \mathbf{x_0} \tag{3.40}$$

Under the same assumptions as above, the logarithmic covariance turns out to be correlated with the relative error $(\mathbf{r})_i = \sqrt{(\mathbf{S}_\mathrm{x})_{ii}}/(\mathbf{x}_0)_i$. With this definition, the covariance is given by

$$(\mathbf{S}_\mathrm{l})_{ii} = (\mathbf{r})_i^2 \tag{3.41}$$

We are in the lucky situation that sonde measurements of water vapor are available in the troposphere. Thus, the tropospheric mean and covariance have been calculated by taking the logarithmized mixing ratios of several 100 sondes. In the stratosphere, a climatology from HALOE and MLS data has been used for the mean. The covariance has been taken from the last tropospheric value.

In principle, we get similar problems when we try to convert the errors which result from the optimal estimation method back from the logarithmic values to the normal values. In the moment, we have found no proper way to do this.

3.4.3 Reference Beam Spectra

We have chosen a direct approach for computing the forward model of the water vapor measurements. Following Equation 2.36, $(P_\mathrm{s} - P_\mathrm{r})/P_\mathrm{r}$ is taken as the measurement vector, where P_r is the power of the reference beam and P_s is the power of the signal beam. Thus, the forward calculation has to compute $(T_{\mathrm{B,s}} - T_{\mathrm{B,r}})/(T_{\mathrm{B,r}} + T_{\mathrm{B,sys}})$, where $T_{\mathrm{B,s}}$ is the brightness temperature of the signal beam, $T_{\mathrm{B,r}}$ is the brightness temperature of the reference beam and $T_{\mathrm{B,sys}}$ is the system noise temperature. The original approach chosen by Parrish et al. [1988] and many others to invert the reference beam spectra is to compute the pure stratospheric line before the retrieval and to invert only this line. This is done by the use of two simplifications.

The first one is the introduction of a two layer model. Since the spectral bias is not known, the attenuation of the stratospheric line by tropospheric water vapor

is not known either. It can only be deduced by additional information, like the measurement angle or the line shape of the parts originating from the troposphere. In Parrish et al. [1988], it is assumed that the attenuating species is only situated in the troposphere, while the observed species is only situated in the stratosphere. This is true for chlorine monoxide or ozone, for example. Now the measurement angle is a function of the tropospheric water vapor content and hence of the attenuation of the line. If $T_{\mathrm{B,s}}(z_0)$ is the measured brightness temperature of the signal beam and $T_{\mathrm{B,r}}(z_0)$ is the measured brightness temperature of the reference beam, the Schwarzschild equation gives

$$T_{\mathrm{B,s}}(z_0) = T_{\mathrm{B}}(z_{\mathrm{T}})e^{-\tau(\vartheta_{\mathrm{s}})} + T_{\mathrm{B}}(\vartheta_{\mathrm{s}}) \tag{3.42}$$

$$T_{\mathrm{B,r}}(z_0) = \left(T_{\mathrm{B}}(z_{\mathrm{T}})e^{-\tau(\vartheta_{\mathrm{r}})} + T_{\mathrm{B}}(\vartheta_{\mathrm{r}})\right)e^{-\tau_{\mathrm{d}}} + T_{\mathrm{d}}(1-e^{-\tau_{\mathrm{d}}}) \tag{3.43}$$

Here, $\tau(\vartheta)$ is the tropospheric opacity as a function of the measurement angle, $T_{\mathrm{B}}(\vartheta)$ is the tropospheric brightness temperature, $T_{\mathrm{B}}(z_{\mathrm{T}})$ is the stratospheric brightness temperature originating from above z_{T}, τ_{d} is the opacity of the absorber plate, T_{d} is the temperature of the plate, ϑ_{s} is the angle of the signal beam and ϑ_{r} is the angle of the reference beam. Now we assume that the system noise is much larger than the signal $T_{\mathrm{B,r}} \ll T_{\mathrm{B,sys}}$ and that the bias in the signal beam equals the bias in the reference beam $T_{\mathrm{B}}(\vartheta_{\mathrm{s}}) = T_{\mathrm{B}}(\vartheta_{\mathrm{r}})e^{-\tau_{\mathrm{d}}} + T_{\mathrm{d}}(1-e^{-\tau_{\mathrm{d}}})$. The second assumption is valid, because the measurement angle has been chosen just to match this requirement. However, it is assumed that the bias is more or less independent of frequency, so that the sign of equality is valid for all frequencies, since the emission from the plate is frequency independent. The stratospheric line can now be computed by

$$T_{\mathrm{B}}(z_{\mathrm{T}}) = \frac{T_{\mathrm{B,sys}}}{e^{-\tau(\vartheta_{\mathrm{s}})} - e^{-\tau_{\mathrm{d}}}e^{-\tau(\vartheta_{\mathrm{r}})}} \frac{P_{\mathrm{s}} - P_{\mathrm{r}}}{P_{\mathrm{r}}} \tag{3.44}$$

Unfortunately, the two assumptions from above are not valid for water vapor. The system noise is in the order of magnitude of the signal, and the bias is not frequency independent.

Another issue is the two layer model. Obviously, the two layer model is not very well suited for water vapor spectra because observed and attenuating species are the same. In principle, it would be possible to divide the profile in stratospheric water vapor and tropospheric water vapor without any approximations. However, there is no clear distinction between the attenuating and the emitting layer, making it somewhat arbitrary where z_{T} is situated. Indeed, there is no need at all to introduce two layers. It is much more convenient to include the volume mixing ratios of all altitudes in the forward model instead of parameterizing the tropospheric attenuation by one parameter and including only the stratospheric mixing

ratios. The tropospheric attenuation is included implicitly in the integral of the Schwarzschild equation and is still determined mainly by the measurement angle, of which this integral is a function.

One may argue that there is not enough information in the spectrum for tropospheric mixing ratios. That can be solved by parameterizing the mixing ratios with one parameter, so that only one parameter is retrieved, but the forward model can calculate the tropospheric mixing ratios out of this parameter. For example, if we assume that the water vapor content decreases exponentially in the troposphere up to an altitude z_T where the mixing ratio is x_T:

$$x = x_T \exp(-A(z - z_T)) \tag{3.45}$$

we could retrieve the scaling factor A and calculate the mixing ratios from it. In general, we have to use less retrieved parameters in the troposphere than the number of layers that are considered in the integral of the radiative transfer equation. Since the opacity of the troposphere is quite large, we have to use a very fine grid in the troposphere to avoid errors in the integration. However, the inversion is rendered unstable if we use much more retrieved parameters than independent information is available.

The second simplification of Parrish et al. allows the integration of spectra measured under different angles. Since the air mass factor dz/dr in Equation 2.10 does only vary by about 1% within 10 km, it can be replaced by the constant air mass factor in a given altitude, provided mixing ratios are only significantly different from zero around the chosen altitude. If self absorption is negligible, the air mass factor can now be placed outside of the integral in the radiative transfer equation 2.9. Hence, it is possible to scale the line as if it were measured in zenith direction. Subsequently, the scaled spectra can simply be averaged. However, this approach is not possible for the direct forward model, since the considered altitude range is larger and self absorption is not negligible here. Either there are enough measurements under the same angle, or the retrieval has to invert spectra measured under different angles in parallel. This would mean to put all spectra in the measurement vector $\mathbf{y}$ in parallel, multiplying the dimension of most matrices and vectors in the retrieval. Disadvantages are increased memory usage and computation time.

3.4.4 Continua and Line Wings

Since the troposphere is calculated explicitly in the forward model, and also because continua have a non negligible frequency dependence within the bandwidth of the radiometer, continua and wings of adjacent lines have to be considered in the retrieval. We follow the approach of Cruz-Pol et al. [1998] here. We assume

a contribution due to unconsidered water vapor lines in the microwave region, a water vapor continuum (the difference between a forward model with all known water vapor lines and a measurement) and a contribution due to an oxygen line cluster at 60 GHz. The oxygen line cluster is considered by calculating 33 oxygen lines. The line shape of oxygen lines is given by

$$F = \frac{1}{\pi}\left(\frac{\nu}{\nu_i}\right)^2\left(\frac{\gamma_{C,i}+Y_i(\nu-\nu_i)}{(\nu-\nu_i)^2+\gamma_{C,i}^2}+\frac{\gamma_{C,i}-Y_i(\nu+\nu_i)}{(\nu+\nu_i)^2+\gamma_{C,i}^2}\right) \tag{3.46}$$

where Y_i is the so called line coupling constant. It is given by

$$Y_i = p\left(\frac{T_0}{T}\right)^{0.8}\left(y_i+\left(\frac{T_0}{T}-1\right)v_i\right) \tag{3.47}$$

where y_i and v_i are empirical parameters and T_0 is a reference temperature. The water vapor continuum term is described by

$$\alpha = \left(C_s p_k^2\left(\frac{T_0}{T}\right)^{10.5}+C_f p_k(p-p_k)\left(\frac{T_0}{T}\right)^3\right)\nu^2 \tag{3.48}$$

where p_k is the water vapor partial pressure and C_f and C_s are empirical parameters taken from Liebe [1989]. The water vapor lines which were explicitly computed by Liebe [1989] are considered by multiplying the continuum term with a factor of 1.2.

3.4.5 Frequency Shift and Self Broadening

The 22 GHz line has a pronounced frequency shift. Different water vapor pressures cause the center of the line to move to different frequencies. The Van Vleck Weisskopf line shape is modified by

$$F_C(\nu) = \frac{1}{\pi}\left(\frac{\nu}{\nu_i}\right)^2\left(\frac{\gamma_{C,i}}{(\nu-\nu_i')^2+\gamma_{C,i}^2}+\frac{\gamma_{C,i}}{(\nu+\nu_i')^2+\gamma_{C,i}^2}\right) \tag{3.49}$$

with

$$\nu_i' = \nu_i - \Delta\nu_i \tag{3.50}$$

where $\Delta\nu_i$ is the frequency shift [Townes and Schawlow, 1975]. The frequency shift originates from phase shifts of the radiation induced by collisions. The equation for the frequency shift parameter $\Delta\nu_i$ has a certain similarity to the equation

for the pressure broadening parameter. The exponent of the temperature dependent part is directly coupled to the exponent x_s from the pressure broadening parameter [Pickett, 1980]:

$$\Delta\nu = d_i p_k \left(\frac{T_0}{T}\right)^{\frac{1}{4}+\frac{3}{2}x_s} \tag{3.51}$$

The parameter d_i has to be determined empirically. Some measurements have been conducted around 1970 here [Liebe and Dillon, 1969; Mrowinski, 1970]. The frequency shift of Mrowinski [1970], which is valid between 2.6×10^{-2} hPa and 40 hPa, has been used for the forward model.

It has also been examined if there is a frequency shift due to oxygen and nitrogen. Liebe and Dillon [1969] assume that the foreign shift is negligible compared to the self shift. A possibility to verify this is the retrieval of the foreign shift with the optimal estimation method. This approach has been implemented and successfully tested by von König [2001] for several lines in the 600 GHz range. While the modification of the forward model is very easy, the derivatives with respect to $\Delta\nu_i$ in the weighting functions become quite complex. Therefore they have been computed numerically in von König [2001]. For this thesis they have been calculated analytically for the first time. However, due to the persistent problems in inverting the full spectra, no reliable frequency shift could be retrieved yet.

In addition to the foreign broadening considered in the ozone and chlorine monoxide models, self broadening has to be modeled in the water vapor model, which is especially important in the troposphere. Self broadening leads to a dependency of the absorption cross sections on the mixing ratios, which considerably complicates the derivatives in the weighting functions.

3.A Covariance Matrices

Assume a measurement series with N quantities, each measured M times, given by the vectors $\mathbf{x}_i$ ($i = 1,\ldots,M$) and its elements x_{ik} ($k = 1,\ldots,N$). Then, the covariance matrix of the vector is given by

$$\mathbf{S}_\mathrm{x} = \begin{pmatrix} \sigma_{11}^2 & \sigma_{12}^2 & \cdots & \\ \sigma_{21}^2 & \ddots & & \\ \vdots & & \ddots & \\ & & & \sigma_{NN}^2 \end{pmatrix} \tag{3.52}$$

The variances σ_{kk}^2 are given by

$$\sigma_{kk}^2 = \frac{1}{M-1}\sum_{i=1}^{M}(x_{ik} - \bar{x_k})^2 \tag{3.53}$$

while the covariances σ_{kl}^2 are given by

$$\sigma_{kl}^2 = \frac{1}{M-1}\sum_{i=1}^{M}(x_{ik} - \bar{x_k})(x_{il} - \bar{x_l}) \tag{3.54}$$

where the mean $\bar{x_k}$ is

$$\bar{x_k} = \frac{1}{M}\sum_{i=1}^{M} x_{ik} \tag{3.55}$$

3.B Logarithmic Distribution

In principle, it is possible to convert mean and covariance of a normal distribution to their logarithmic equivalents. However, it turns out that the occurring integrals are only analytically solvable under the assumption that the mean is much greater than the variance $\mu \gg \sigma$. This assumption is not only needed for the integrals, but also to avoid a non negligible probability for unphysical negative values in the distribution.

The normal distribution is given by

$$f(x) = \frac{1}{\sqrt{2\pi}\sigma_x}\exp\left(-\frac{1}{2}\left(\frac{x-\mu_x}{\sigma_x}\right)^2\right) \tag{3.56}$$

where μ_x is the mean of the distribution, σ_x is the standard deviation and $f(x)$ is the mixing ratio. Application of the logarithm yields

$$f(l) = C \exp\left(-\frac{1}{2}\left(\frac{\exp l - \mu_x}{\sigma_x}\right)^2\right) \tag{3.57}$$

with a yet unknown normalizing constant C and $x = \exp l$. The domain for x and the corresponding domain for l have to be restricted to avoid divergence of the following integrals. This restriction is equivalent to the exclusion of unphysical outliers and negative values. We assume a domain of $x = \mu_x - n\sigma_x, \ldots, \mu_x + n\sigma_x$, with a sufficiently small integer n, corresponding to $l = \ln(\mu_x - n\sigma_x), \ldots, \ln(\mu_x + n\sigma_x)$. However, n should not become too small either, because we assume it can be replaced by infinity in some of the following integrals. First of all, we have to calculate the normalizing constant C:

$$C^{-1} = \int_{\ln(\mu_x - n\sigma_x)}^{\ln(\mu_x + \sigma_x)} \frac{f(l)}{C}\,\mathrm{d}l = \int_{\ln(\mu_x - n\sigma_x)}^{\ln(\mu_x + n\sigma_x)} \exp\left(-\frac{1}{2}\left(\frac{\exp l - \mu_x}{\sigma_x}\right)^2\right)\,\mathrm{d}l \tag{3.58}$$

With $z = \frac{\exp l - \mu_x}{\sigma_x}$

$$C^{-1} = \int_{-n}^{n} \exp\left(-\frac{1}{2}z^2\right) \frac{1}{z + \mu_x/\sigma_x}\,\mathrm{d}z \tag{3.59}$$

Introducing $\mu_x \gg \sigma_x$, we get

$$C = \frac{1}{\sqrt{2\pi}} \frac{\mu_x}{\sigma_x} \tag{3.60}$$

Next, we compute the logarithmic mean $\int f(l) l\, dl$:

$$\begin{aligned} \mu_l &= \frac{1}{\sqrt{2\pi}} \frac{\mu_x}{\sigma_x} \int_{\ln(\mu_x - n\sigma_x)}^{\ln(\mu_x + n\sigma_x)} \exp\left(-\frac{1}{2}\left(\frac{\exp l - \mu_x}{\sigma_x}\right)^2\right) l\,\mathrm{d}l \\ &= \frac{1}{\sqrt{2\pi}} \frac{\mu_x}{\sigma_x} \int_{-n}^{n} \exp\left(-\frac{1}{2}z^2\right) \frac{\ln(z\sigma_x + \mu_x)}{z + \mu_x/\sigma_x}\,\mathrm{d}z \end{aligned} \tag{3.61}$$

Again, we use $\mu_x \gg \sigma_x$:

$$\mu_l \approx \frac{1}{\sqrt{2\pi}} \frac{\mu_x}{\sigma_x} \ln \mu_x \frac{\sigma_x}{\mu_x} \int_{-n}^{n} \exp\left(-\frac{1}{2}z^2\right)\,\mathrm{d}z = \ln \mu_x \tag{3.62}$$

Similarly, we get the covariance

$$\sigma_l^2 = \frac{1}{\sqrt{2\pi}}\frac{\mu_x}{\sigma_x}\int_{\ln(\mu_x-n\sigma_x)}^{\ln(\mu_x+n\sigma_x)} \exp\left(-\frac{1}{2}\left(\frac{\exp l-\mu_x}{\sigma_x}\right)^2\right)(l-\mu_l)^2\,\mathrm{d}l$$
$$= \frac{1}{\sqrt{2\pi}}\frac{\mu_x}{\sigma_x}\int_{-n}^{n} \exp\left(-\frac{1}{2}z^2\right)\frac{\left(\ln(z\sigma_x+\mu_x)-\ln\mu_x\right)^2}{z+\mu_x/\sigma_x}\,\mathrm{d}z \tag{3.63}$$

where we already have taken advantage of $\mu_l = \ln\mu_x$. Introducing the relative error $r = \sigma_x/\mu_x$ yields

$$\sigma_l^2 = \frac{1}{\sqrt{2\pi}}\frac{\mu_x}{\sigma_x}\int_{-n}^{n} \exp\left(-\frac{1}{2}z^2\right)\frac{\left(\ln(1+zr)+\ln\mu_x-\ln\mu_x\right)^2}{z+\mu_x/\sigma_x}\,\mathrm{d}z \tag{3.64}$$

Finally, assuming $\mu_x \gg \sigma_x$ and $\ln(1+zr) \approx zr$, we get

$$\sigma_l^2 = \frac{1}{\sqrt{2\pi}}r^2\int_{-n}^{n} \exp\left(-\frac{1}{2}z^2\right)z^2\,\mathrm{d}z = \frac{1}{\sqrt{2\pi}}r^2\frac{2\sqrt{\pi}}{4/\sqrt{2}^3} = r^2 \tag{3.65}$$

Another approach would be to assume a lognormal distribution for the mixing ratios

$$f(x) = C\exp\left(-\frac{1}{2}\left(\frac{\ln x-\mu_l}{\sigma_l}\right)^2\right) \tag{3.66}$$

so that the logarithm of the mixing ratio is normal distributed. The result for the mean and the covariance is exactly the same in this case.

4 Ozone Depletion

4.1 Overview

The determination of anthropogenic ozone depletion has been a key topic in atmospheric sciences in the last decades. There is still a vivid interest in this topic, particularly due to the wide coverage in the press and in politics connected with the increased risk of skin cancer and the impact on climate change. Hence, countless studies have been carried out in the last years aiming at a better understanding of the mechanisms of ozone depletion.

A severe depletion of stratospheric ozone has been observed every year over Antarctica in late winter and spring in these studies since the mid eighties. A similar but not quite as pronounced ozone depletion has also been detected over the northern polar region in the past winters. The greatest effort so far to quantify the ozone loss in the Arctic was the SOLVE/THESEO campaign in 1999/2000, a joint effort of numerous American and European institutes and universities, yielding a multitude of simultaneous measurements of the key species of ozone chemistry [Newman et al., 2002]. A wealth of publications resulted from the campaign, rendering this winter to one of the best examined examples of ozone depletion. The winter of 1999/2000 proved to be a prime example for severe depletion. The polar vortex developed in early December and remained strong and stable until March. Temperatures were exceptionally cold and enabled the formation of polar stratospheric clouds in large areas of the vortex. Cloud formation was accompanied by high chlorine activation, and extensive denitrification was measured for the first time in the Arctic vortex.

This chapter is split into two parts. The calculation of ozone loss rates is treated in the first part, while the reasons for the loss are examined in the second part. We will have a look at the computation of ozone loss rates first. A variety of different techniques has been developed over the past decade to determine ozone loss rates. The main task of all these methods is the separation of dynamically induced and chemically induced changes in the measured ozone mixing ratios. A short outline of the several possibilities to deal with this problem shall be given now:

- The Match technique uses a Lagrangian approach. An air parcel is probed by a sonde at a given time and location and its path is followed by trajectory calculations. When the air parcel passes another launch facility, it is probed for a second time. Differences in the observed ozone concentration at a given isentrope, corrected for diabatic descent from a radiative transfer model, are due to chemical loss.

- Other methods use the correlation of a tracer and ozone to separate between dynamical and chemical ozone variations. Changes in the ratio of a dynamic tracer such as N_2O or HF and ozone can only be caused by chemical ozone loss or mixing because tracer and ozone follow the same dynamics.

- Several techniques use vortex averaged ozone mixing ratios from different instruments. Diabatic subsidence is again accounted for by a radiative transfer model.

- The last possibility is to use modeled passive ozone compared to actual measurements.

Vortex averaged ozone loss rates can also be derived from the measurements of the RAM instrument. Although the observations are carried out at a single location, it is feasible to obtain vortex means from the ozone measurements by assuming that the vortex is sufficiently homogenous, so that the temporal mean of the measurements can be converted to a spatial mean. As usual, diabatic descent is calculated by a radiative transfer model. This method was first proposed and applied by Sinnhuber [1999]. First results covered the winter 1996/1997 [Sinnhuber et al., 1998], followed by calculations for the winter 1997/1998 [Langer et al., 1999]. A modified and improved version of the ozone depletion software was used for Klein et al. [2002], which treated the winter 1999/2000. This chapter is an extended and updated version of this paper. Additionally, first results are presented for the winter 2000/2001. We will concentrate on the 475 K isentropic level at about 20 km altitude here. This is not only the altitude where the strongest loss rates are usually observed, but it is also the sole altitude range, where our method is applicable with acceptable error bars due to some altitude resolution features.

In the following, we will give an overview over the next sections. In the sections 4.2 and 4.3, we deal with the method in general and with the details of its implementation, giving information about the calculation of loss rates and cumulative loss, the radiative transfer model, the vortex edge calculation and the treatment of altitude resolution. Section 4.4 gives an overview over the meteorological situation in which the measurements took place. Results of the ozone depletion calculations are presented in section 4.5. The accuracy of the techniques used for the determination of ozone loss rates is an important and disputed

topic. Thus, we perform a detailed comparison to other measurements and the SLIMCAT model, accompanied by an in-depth examination of error sources and a mathematically stringent error analysis. Comparison and error analysis can be found in sections 4.6 and 4.7. In section 4.8 we have a short look on the general picture and present results for other isentropic levels than the 475 K level and high resolution measurements.

Another focal point is the chemistry of the ozone depletion. Measurements of chlorine monoxide, reservoir gases, nitrate species and denitrification are shown to develop a chemical scenario for the winter. Chlorine monoxide measurements of the RAM have already been investigated for earlier winters in the past in [Raffalski et al., 1998] and [Klein et al., 2000]. In section 4.9 we present the measurements of chlorine monoxide conducted in 1999/2000 and their interpretation. The evolution of chlorine monoxide and other important trace gases is shown in the course of the winter and results are compared to the SLIMCAT model, which is representing the current understanding of ozone chemistry. Some obvious discrepancies are discussed further. Especially, differences in chlorine activation are observed, which are attributed to uncertainties in the denitrification scheme and the formation mechanism for stratospheric clouds in the model. Since denitrification played an important role in 1999/2000, it is discussed in detail in section 4.10. The surprisingly good agreement of the ozone loss rates of the measurements and the model is examined in section 4.11. Finally, section 4.12 gives an overview over the results for the winter 2000/2001.

4.2 Method

The observed ozone change at a given altitude is a superposition of dynamic changes and chemical loss. In order to obtain the chemical loss, it is necessary to separate chemical variations from dynamic variations. The latter are caused by horizontal, adiabatic and diabatic motions, which can be treated separately inside the vortex:

- Horizontal change: Air inside the polar vortex is expected to be well mixed and isolated from mid latitude air masses. Thus the vertical ozone distribution at Ny-Ålesund is assumed to be representative for air masses inside the vortex (as long as Ny-Ålesund is situated inside the vortex). To account for horizontal inhomogeneities, the ozone data are temporally averaged.

- Adiabatic change: The adiabatic change is taken into account by calculating all changes at a given isentropic level.

- Diabatic change: Diabatic heating rates are calculated using a radiative transfer model. In combination with the known vertical gradient of ozone,

this can be used to calculate the ozone change due to descent or ascent relative to the isentropes.

These assumptions allow us to determine vortex averaged ozone loss rates from observations at a single location. Vortex averages are required not only for ozone, but also for the input parameters of the radiative transfer model. Thus the vortex edge has to be calculated and the data have to be averaged appropriately. Care has to be taken that no exchange of air over the vortex edge is occurring, which can be examined with different methods [Sobel et al., 1997].

The chemical change $\partial x/\partial t$ of the volume mixing ratio x at a given isentrope could now be obtained using a simple equation:

$$\frac{\partial x}{\partial t} = \frac{\mathrm{D}x}{\mathrm{D}t} - \frac{\partial x}{\partial \Theta}\frac{\partial \Theta}{\partial T}Q \tag{4.1}$$

$\mathrm{D}x/\mathrm{D}t$ denotes the observed change, $\partial x/\partial\Theta$ is the vertical gradient of the ozone mixing ratio with respect to potential temperature, $\partial\Theta/\partial T$ is the change of potential temperature with temperature and Q is the calculated heating rate. Note that this is just a substantive derivative neglecting horizontal motions solved for $\partial x/\partial t$.

It can be shown that the calculation of the cumulative ozone loss by simply integrating Equation 4.1 would lead to erroneous results (see Appendix 4.A). Alternatively, we have created an ozone tracer from the RAM data that represents the profile that would have been observed without any chemical processes. This passive profile is computed by taking an initial profile and subsiding it by

$$\frac{\partial z}{\partial t} = \frac{\partial z}{\partial \Theta}\frac{\partial \Theta}{\partial T}Q \tag{4.2}$$

in every altitude where the profile is defined and interpolating it on the original grid again. $\partial z/\partial\Theta$ is the derivative of altitude with respect to potential temperature. Hence, heating rates are not only needed at the isentropic level where the ozone loss rates are obtained, but in all altitudes where the passive profile is defined. The subsided profile is convoluted with the averaging kernels to realign it with the altitude resolution (see Appendix 4.B). The observed and passive ozone profiles are averaged over a period of 5 days. Eventually, the chemical loss $\hat{\mathbf{c}}$ can be computed by subtracting the passive profile $\hat{\mathbf{p}}$ from the observed profile $\hat{\mathbf{x}}$:

$$\hat{\mathbf{c}} = \hat{\mathbf{x}} - \hat{\mathbf{p}} \tag{4.3}$$

The cumulative loss and the ozone loss rates are rendered comparable by calculating the loss rates directly from the cumulative loss and ignoring Equation 4.1. The chemical change is calculated by taking the difference between the cumulative losses from 12.5 days before and 12.5 days after the considered day and

dividing it by 25 days. The same is done for the passive profiles and the observed ozone mixing ratio to obtain the diabatic and observed change. The long period of 25 days used for the loss rate calculations is due to the amplification of measurement noise in the derivative of the mixing ratio.

4.3 Implementation

Additional data are needed apart from the ozone observations to perform the loss rate calculations. Temperature, geopotential altitude, wind and potential vorticity are obtained from the analysis of the European Center for Medium-Range Weather Forecast (ECMWF) on a $2.5^\circ \times 2.5^\circ$ grid in longitude and latitude. All data is available at 12 pressure levels, except for potential vorticity, which is given at isentropic levels. The data are used for the calculation of the vortex edge and as an input for the radiative transfer model.

Carbon dioxide and water vapor, which are needed by the radiative transfer model, have to be modeled due to a lack of measurements. Carbon dioxide has a mixing ratio of about 360 ppm, which is spatially constant but permanently rising due to anthropogenic pollution. Water vapor is derived from the temperature field and a climatology. In the troposphere, a constant relative humidity of 70% at ground level decreasing linearly to 8% at 12 km is assumed. This relationship has been deduced from the mean humidity of sondes launched at Ny-Ålesund. The water vapor mixing ratio is calculated from the product of the relative humidity and the saturation pressure, which is a function of temperature. The breakpoint between troposphere and stratosphere is taken from the tropopause level given in the ECMWF temperature data. In the stratosphere a climatology derived from data of the HALOE and MLS instruments on board the UARS satellite is used [Randel et al., 1998]. Water vapor is a considerable error source for every method using calculated cooling rates, since it is known so badly. In the future, water vapor profiles from the 22 GHz radiometer could be used, but in the moment these data are not reliable enough.

The calculation of the vortex edge is crucial because the observed air masses have to be well isolated from mid latitudes and homogenous. A fixed potential vorticity value is often taken as the edge contour. In theory, there is no exchange of air over the edge of a potential vorticity contour, if all processes are adiabatic and reversible. However, the choice of the potential vorticity value tends to be quite arbitrary and there are certainly irreversible and diabatic processes. Thus we use a more accurate method. The edge of the vortex is calculated using the potential vorticity gradient with respect to equivalent latitude [Nash et al., 1996]. As a reminder, the equivalent latitude of a potential vorticity contour is defined as the latitude it would have if the enclosed area would be circular and centered

over the pole. The maxima of the second derivative of the potential vorticity with respect to equivalent latitude are taken as the inner and outer edge of the vortex. The calculation is stabilized by multiplying the first derivative with the potential-vorticity-mapped wind strength. Finally, the equivalent latitude of the edge is averaged over 5 days to eliminate unrealistic scatter.

Ozone data are averaged over 5 days. Days with Ny-Ålesund outside the vortex are discarded. This converts the temporal mean of the ozone mixing ratio to a spatial mean over the inner vortex. Consecutive days with a weak gradient at the beginning and the end of the observed time period are excluded because air from mid latitudes could be advected inside the vortex and alter the mixing ratios. If there are days with a weak gradient scattered throughout the observed period, the method is not applicable. Alternatively, methods of calculating transport across the vortex edge could be used, but usually the error bars of these methods are too large for meaningful results.

Input data for the radiative transfer model are averaged over the area inside of the inner vortex edge. For the heating rate calculations the radiative transfer model MIDRAD by Shine [1987, 1991] is used. The code of this model appears in almost every study where heating rates are needed, and all methods presented here involve some more or less recent version of MIDRAD, sometimes with special adaptions. The thermal infrared absorption and emission due to carbon dioxide, water vapor and ozone is calculated for a frequency range from 0 cm^{-1} to 3000 cm^{-1} with an expression similar to the radiative transfer equation 2.9. The expression is giving the net radiative flux as the difference of the upward and downward flux. If F is the net irradiance (the integral of the spectral brightness over all solid angles and frequencies), the heating rate Q can be calculated by

$$Q = \frac{g}{c_p}\frac{\partial F}{\partial p} \tag{4.4}$$

where g is the gravitational acceleration and c_p is the specific heat capacity at constant pressure. The model parameterizes the absorption lines by a narrow band model by Malkmus with a spectral resolution of 10 cm^{-1} in order to reduce computation time. Line data are taken from the HITRAN catalogue. The short wave absorption due to ozone and water vapor is computed by the DISORT program. A detailed description of the model can be found in [Sinnhuber, 1999]. In order to reduce computation time further, the calculations are carried out as zonal means with input data averaged over longitudes inside the inner vortex edge. The resulting heating rates are averaged over all latitudes inside the polar vortex. The model uses an albedo of 0.9, assuming that the surface is covered with ice and snow. Clouds are not considered in the calculations.

4.4 Meteorological Situation

The winter of 1999/2000 was one of the coldest winters in the stratosphere in the last 20 years [Manney and Sabutis, 2000], fitting well into a general cooling trend in the stratosphere [Pawson and Naujokat, 1999]. This is evident in a plot of the vortex minimum temperatures of the last winters, see Figure 4.1. Temperatures dropped below the formation temperature for NAT clouds throughout December, January and February at the 475 K isentropic level. In January, even the formation of ice clouds was possible, which is quite unusual for the Arctic. The potential area where the formation of polar stratospheric clouds was possible is presented in Figure 4.2 for the 475 K and the 550 K level. The area for NAT clouds is depicted in light gray and the area for ice clouds is shown in dark gray. NAT temperatures have been calculated according to Hanson and Mauersberger [1988] from the water vapor climatology and with a HNO_3 mixing ratio of 10 ppb. Ice temperatures were calculated with the Magnus formula [Roedel, 1994]. The area of the vortex is shown for comparison. Measurements of the satellite instrument POAM III and of the ground based lidar in Ny-Ålesund show that the potential polar stratospheric cloud area is a good estimator for the real occurrence of these clouds in this winter [Bevilacqua et al., 2002; Rex et al., 2002].

In Figure 4.3, the evolution of the polar vortex is displayed. The contours represent the potential vorticity at a given equivalent latitude and date. The black dots mark the position of Ny-Ålesund in terms of equivalent latitude and the thick lines denote the inner and the outer edge of the vortex. In early December, the vortex edge is not shown due to a weak gradient prohibiting the calculation of the edge. The polar vortex formed during the first days of December 1999 at the 475 K level and remained discernible until early April. Vortex development was comparable to other cold winters and resulted in a stable and isolated vortex, with a relatively slow build-up in December disturbed only by some minor warmings. In January to April warmings occurred between mid January and early February (warming above ice temperatures), in mid March and in early April (break up of the vortex). Beginning on March 17, the vortex split up into two parts, leaving Ny-Ålesund outside the vortex. Ny-Ålesund was situated well inside the vortex from early December on until this moment. Thus the period of usable results for the ozone depletion calculations extends from December 11, 1999 to March 16, 2000.

Although there was some filamentation, no intrusion of extra vortex air occurred that remarkably altered the mixing ratios after December. We have carried out reverse domain filling calculations that indicate that the vortex air was well isolated from mid latitude air for the investigation period from January on. Since this is only a qualitative statement for established methods of transport detection

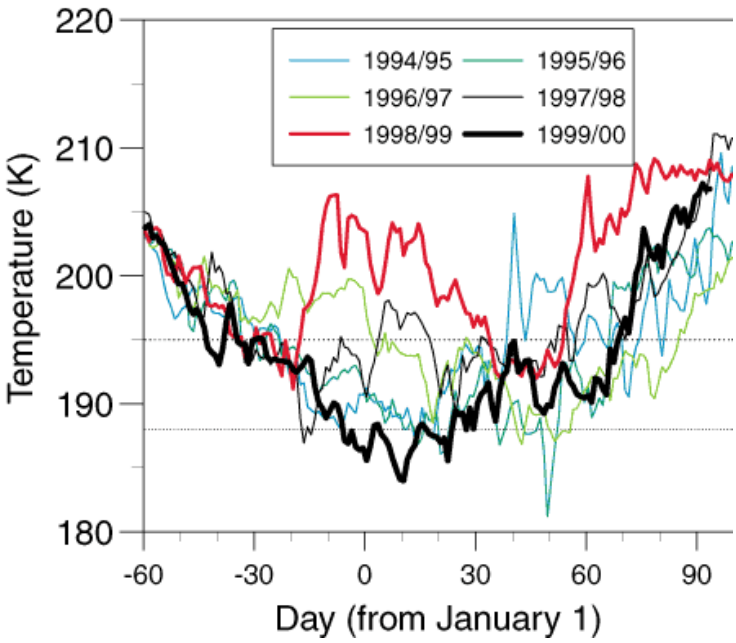

Figure 4.1: Minimum temperatures at the 46 hPa pressure level (about 475 K). Lines show the formation temperatures for NAT (upper line) and ice clouds (lower line). Adapted from Sinnhuber et al. [2000].

like contour crossing or local gradient reversal [Sobel et al., 1997], further evidence is needed.

Richard et al. [2001] use tracer correlations to show that no mixing across the vortex edge occurred. If two or more chemically conserved tracers with non-linear compact relationships between their mixing ratios show no deviations from the initial early vortex relationship throughout the winter, we can draw the conclusion that no large isentropic mixing event between vortex and outer vortex air occurred. It has been assumed that the outer vortex relationship is significantly different from the inner vortex relationship here. Richard et al. conclude from in-situ measurements of the NASA ER-2 aircraft and OMS balloon measurements of N_2O, CO_2 and CFC-11 that the vortex was relatively well isolated from January to March. It has to be noted that sometimes mixing may be difficult to detect from tracer relations [Plumb et al., 2000], so we cannot exclude mixing categorically here.

Rex et al. [2002] show by comparison of Match loss rates and vortex averaged loss rates from sondes that no significant mixing occurred. In Match, care is taken to avoid areas of small scale mixing [Rex et al., 1999]. If there was entrainment of extra vortex air, the vortex averaged loss would be altered, but not the loss inferred

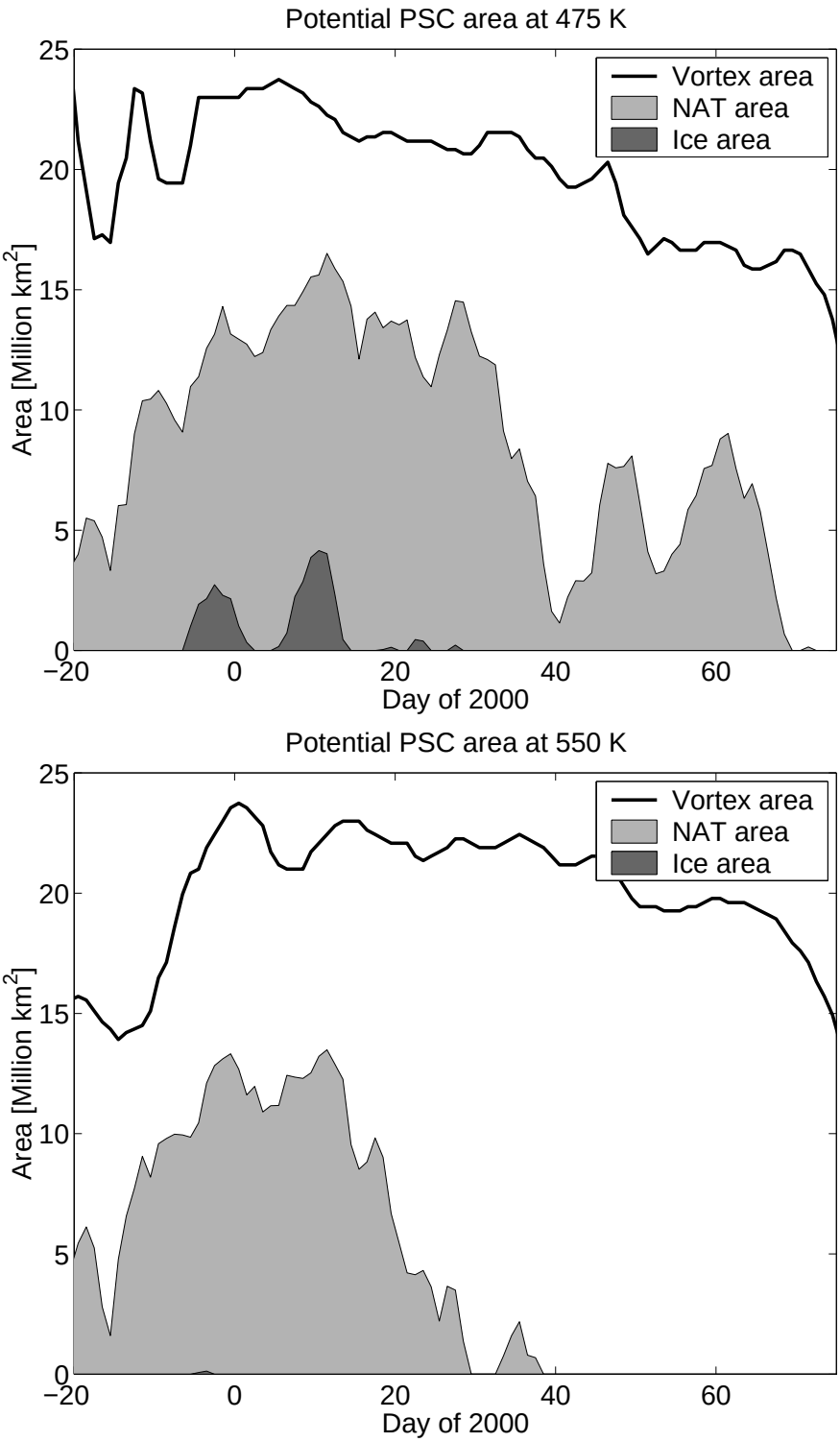

Figure 4.2: Potential PSC area. in 1999/2000. Upper panel: Temporal evolution of the area of temperatures below the formation temperature of NAT (light gray) and ice (dark gray) at the 475 K level inside the vortex. The area of the vortex is shown for comparison. Lower panel: Same for the 550 K level.

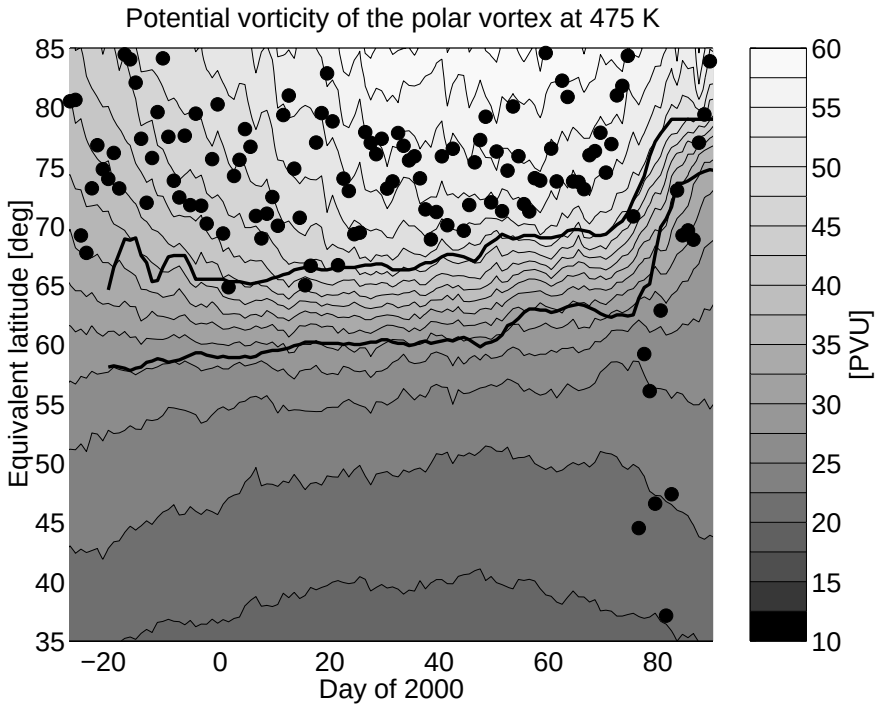

Figure 4.3: Vortex evolution in 1999/2000 at the 475 K level. Contours represent the potential vorticity at a given equivalent latitude and date. The black dots mark the position of Ny-Ålesund in terms of equivalent latitude and the thick lines denote the inner and the outer edge of the vortex.

from Match. The loss profiles agree very well for the period from early January to late March, showing that no substantial mixing happened (see also Figure 4.15).

In Figure 4.4, the evolution of the heating rates is shown. The upper panel presents the heating rate profile as a function of pressure for an arbitrarily chosen day. The dashed line shows the heating due to short wave radiation (mainly by ozone in the stratosphere and water vapor in the troposphere) and the thick solid line shows the cooling due to long wave radiation (mainly by carbon dioxide in the stratosphere and water vapor in the troposphere and stratosphere). Long wave cooling and short wave heating lead to a net cooling rate (thin line). In the lower stratosphere, heating and cooling almost cancel out, which is connected with large error bars in the net cooling rates. It is evident that the net cooling rates, and thus the subsidence of air, increase considerably with altitude. This effect influences the passive profiles of the ozone depletion calculations, as we will see soon. The lower panel shows the temporal evolution of the heating rates. While the long wave cooling stays almost constant in the course of the winter, the short wave

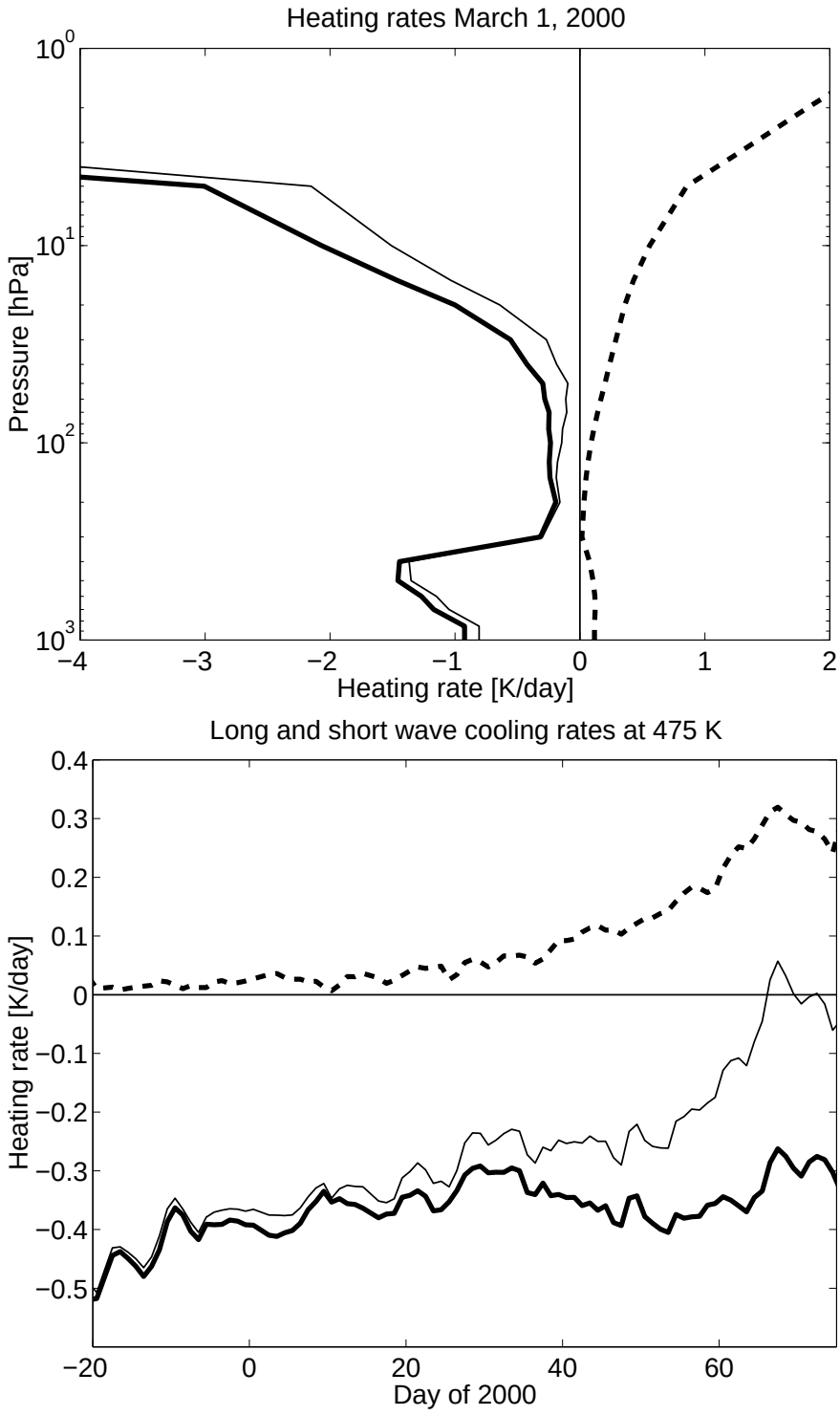

Figure 4.4: Heating rates. Long wave cooling is shown by a solid line, short wave heating is shown by a dashed line and net heating rates are shown as a thin line. Upper panel: Heating rates at March 1, 2000 as a function of pressure. Lower panel: Temporal evolution of the heating rates in the winter 1999/2000 at the 475 K level.

heating gets stronger due to the increase in sunlit hours in the vortex. The result is a decrease in the net cooling of the vortex, leading to strong descent in December, which is steadily decreasing to zero in March.

4.5 Ozone Depletion in 1999/2000

The observed ozone volume mixing ratio at the 475 K level is presented in Figure 4.5. Following an increase until the end of January, the volume mixing ratio begins to decrease significantly (thick line). Due to the limited vertical resolution of the RAM and the ozone loss occurring in a rather narrow layer, the observed decrease is underestimated in comparison with high resolution measurements at this altitude. In fact, values as low as 1.5 ppm have been observed by sondes in the considered time period. However, sondes adjusted to the vertical resolution of the RAM (dots) show very good agreement. The SLIMCAT calculations (thin line) will be discussed later.

In Figure 4.6 we present the results of the vortex averaged ozone loss calculations. The ozone change due to diabatic descent of air masses through the 475 K level decreases in the course of the winter (thin line), and leads to an increase in the ozone volume mixing ratio due to the positive vertical ozone gradient at these altitudes. The diabatic change has to be subtracted from the observed mixing ratios (thick line) to obtain the chemical loss rates (dashed line). Chemical loss rates of about 10 ppb/day in December and January, which were completely masked by the descent of ozone rich air from above, are leading to an increase in the observations. Interestingly, much less chemical loss is expected in December and January, since the sunlit times in the vortex are much too short to cause significant chlorine activation and stratospheric cloud formation has not set in. We will come back to this issue later. In February and March ozone loss reached rates of up to 25 ppb/day, causing the observed decline of the ozone volume mixing ratio. Note that these loss rates are averaged over an altitude range corresponding to the RAM vertical resolution and are temporally averaged over 25 days and tend to be lower than the actual loss rates at this altitude.

The shaded area denotes the estimated accuracy of the calculations. The shown errors are calculated assuming a statistical error of 0.14 ppm in the RAM measurements. Additionally, an autocorrelation time of the ozone time series of 0.5 days is supposed. The error of the heating rates is set to 0.1 K. While the error of the RAM measurements is well known, the error in the heating rates can only be estimated. This will be discussed in more detail in section 4.7. A detailed error analysis is given in Appendix 4.C.

It can be seen that the loss rates in December and, to a lesser extent, in January are statistically significant. There are several possible explanations for these re-

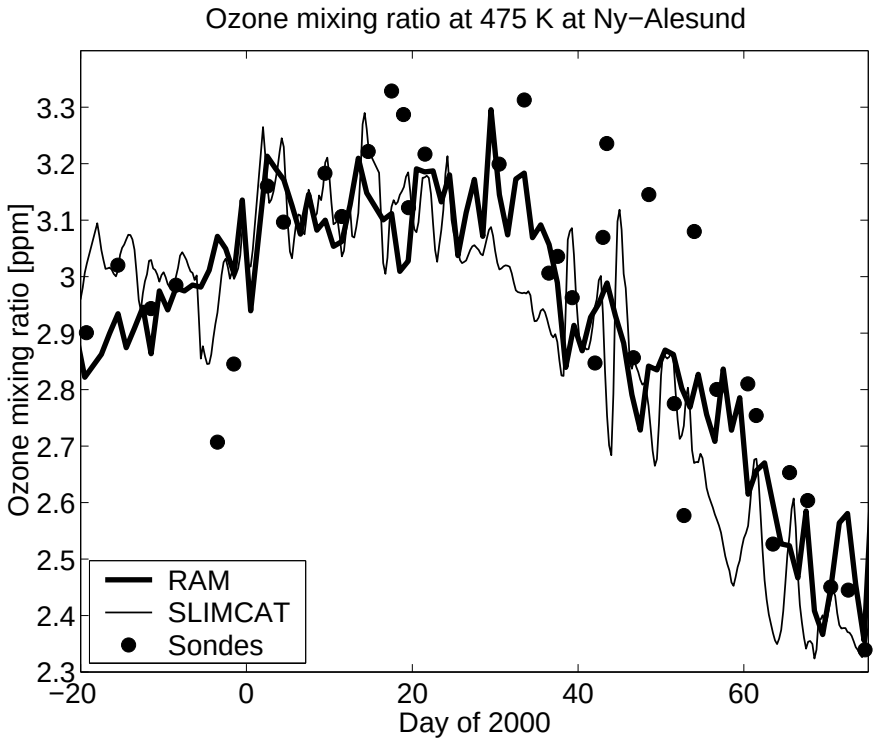

Figure 4.5: Ozone mixing ratio at the 475 K isentropic level in the winter 1999/2000. Measurements of the ozone radiometer (diurnal means, thick line) and of sondes (dots) at Ny-Ålesund, and SLIMCAT model results (thin line).

sults. Since some transport across the vortex edge occurred in December [Richard et al., 2001], mixing ratios could have been changed by the intrusion of mid latitude air. Another explanation is an overestimation of the cooling rates. The heating rates of SLIMCAT underestimate our cooling rates by more than 0.2 K/day in December and January, which is outside of the assumed error bars, see also Figure 4.10. As already stated, a detailed discussion of the accuracy of the heating rates can be found in section 4.7. As a third possibility, the inferred chemical loss rates may be true. If so, the loss cannot be explained by chlorine activation, since measurements of chlorine monoxide show very low mixing ratios in December (see section 4.9) and stratospheric cloud occurrence was only sporadic. High chemical ozone loss rates in dark areas of the vortex that cannot not be explained by the current understanding of ozone chemistry were observed in several studies so far, for example by Becker et al. [1998]. Thus, unknown chemistry may be the reason for the discrepancies. However, a final conclusion cannot be reached here without further evidence.

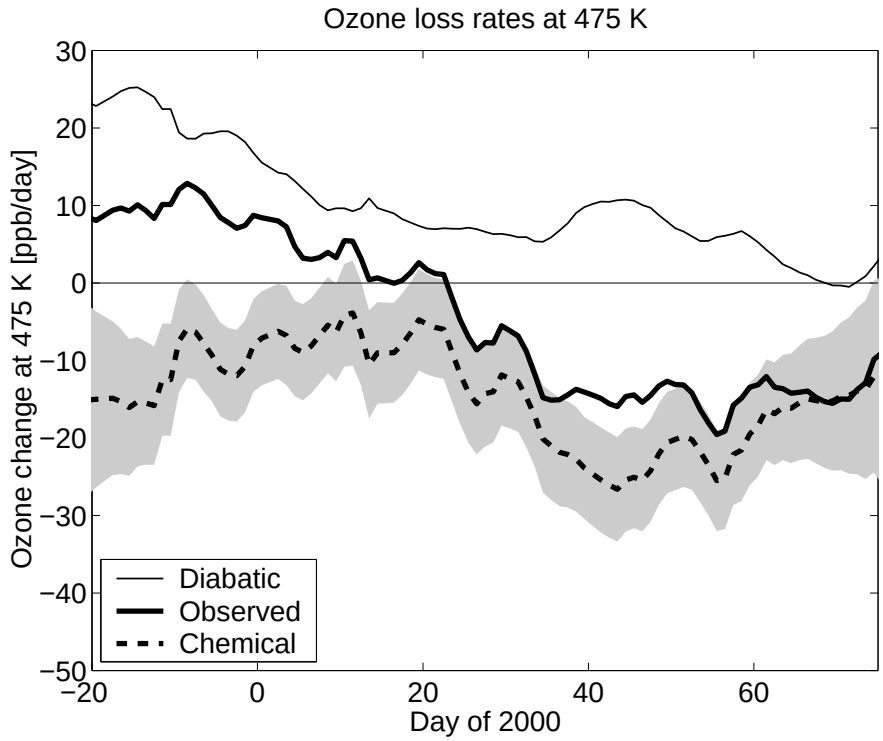

Figure 4.6: Ozone loss per day at the 475 K isentropic level in 1999/2000. The thick line shows the ozone change per day observed by the radiometer, the thin line shows the change due to diabatic descent inferred from the passive profile, the dashed line shows the chemical change (with error bars), given by the difference of the above changes. All changes are 25 day means. The passive profile has been corrected for natural ozone production.

We will now address the cumulative loss. In Figure 4.7 the volume mixing ratio of December 11, 1999, reduced by the cumulative chemical loss obtained from the RAM calculations, is shown for the 475 K level. December 11 is taken as an initial point since the passive profile was initialized on this day. The cumulative loss adds up to 1.2 ± 0.4 ppm (41%) at the end of the winter. This is one of the highest losses ever observed by the RAM, comparable to the cumulative loss of 1.4 ± 0.4 ppm (53%) inferred in the winter 1996/97. The large error bars of the cumulative loss result mainly from the error in the heating rates, which is assumed to be systematic. SLIMCAT and GOME results will be discussed in the next section.

Since ozone loss only occurs in sunlight, the ozone loss rates per sunlit hour are also worth a look, see Figure 4.8. The sunlit hours have been calculated assuming that the vortex edge inferred from the potential vorticity analysis does not

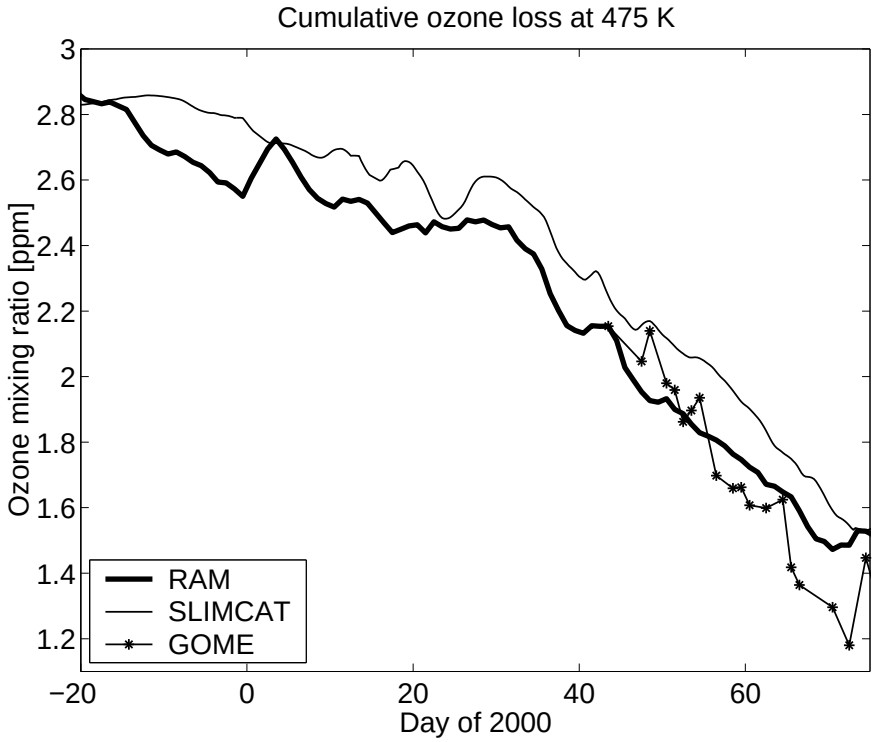

Figure 4.7: Cumulative loss at the 475 K isentropic level in 1999/2000. Shown is the volume mixing ratio of December 11, 1999 reduced by the cumulative loss obtained by the ozone radiometer (thick line) and the SLIMCAT model (thin line). The GOME results (line with asterisks) use February 13, 2000 as an initial value. The passive profile used for the cumulative loss calculations has been corrected for natural ozone production.

change in the course of 24 hours. The sunlit times of every grid point in the vortex were calculated by performing one revolution of the earth and counting the sunlit hours of the points. The sunlit times of all points have been averaged spatially then. In addition, a 25 day running mean has been applied to render the sunlit hours comparable to the averaged loss rates. The evolution of the sunlit hours can be found in Figure 4.9. In December and January, the loss rates per sunlit hour range from 2 ppb/sunlit hour to 4 ppb/sunlit hour. The large error bars in this period are a result of the scaling of the original loss rates with the inverse of the sunlit hours. In addition to the errors of the loss rates we have to take into account an error due to the trajectories of the measured air parcels. Air parcels could have received systematically more or less sunlit hours than indicated by the vortex mean. This error is reduced if the number of sunlit hours is rising (it is less than 4 hours until the end of January). In February, loss rates per sunlit hours

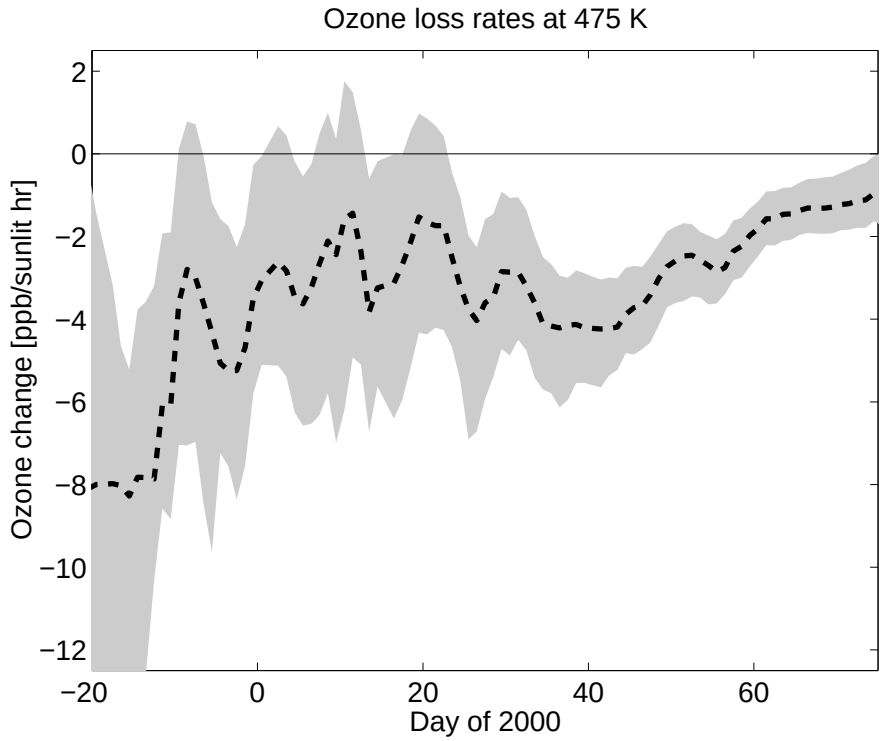

Figure 4.8: Ozone loss per sunlit hour at the 475 K isentropic level in 1999/2000. The shaded area denotes the error bars.

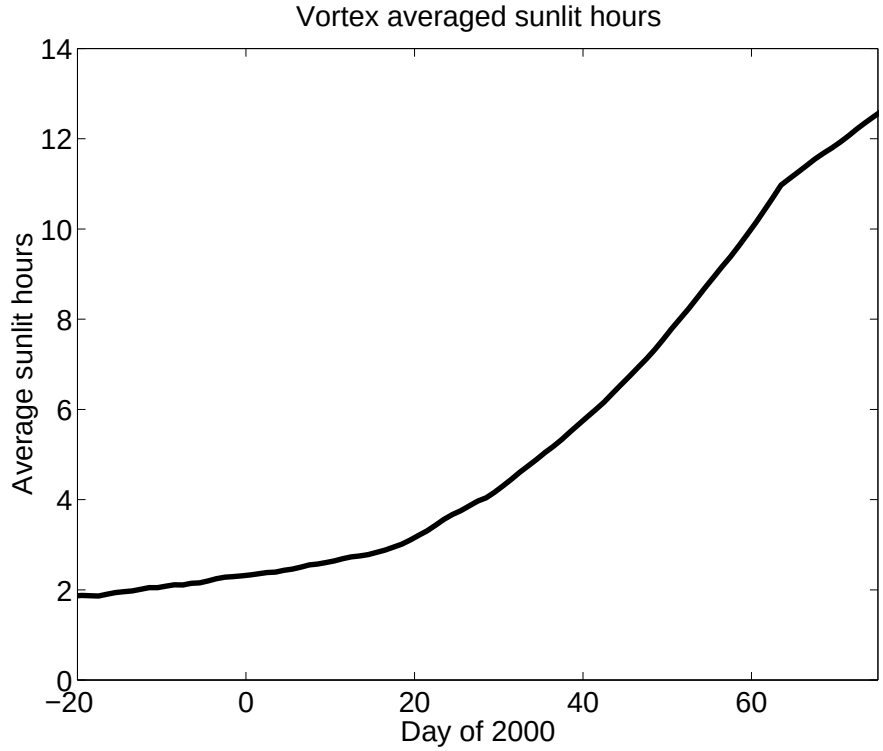

Figure 4.9: Vortex averaged sunlit hours at the 475 K isentropic level in 1999/2000.

reach a maximum of 3 ppb/sunlit hour, declining slowly to 1 ppb/sunlit hour in March. The high loss rates per day in March are due to the long sunlit times of the air parcels. The loss rates per sunlit hour are even decreasing in March due to the warmer temperatures. Results in January are inconclusive, since they are relatively low, but the potential area for stratospheric clouds was at a maximum then. However, the various inherent errors (high dependence of loss rates on the temperature and sunlit history of the air parcels observed, influence of altitude resolution, large error bars of the loss rates), make a quantitative comparison difficult. A trajectory analysis of the measured air parcels could bring some more insight here. Due to the same reasons, we have made no quantitative comparison of chlorine monoxide mixing ratios and loss rates.

4.6 Comparison with Other Techniques

In the winter 1999/2000, numerous techniques have been applied to estimate ozone depletion. Since there are several independent methods, a comparison should give a good estimate of the accuracy we can expect, which is important for two reasons: The errors of all methods are quite large and, in some cases, cannot be calculated analytically. We examine three of the four major methods mentioned in the introduction:

- The Lagrangian technique Match
- Tracer measurements
- Vortex averaged loss

In addition to that, we test our knowledge about the underlying physics with a chemical model. RAM results are compared to seven methods basing on measurements and one model in detail in the next subsections: to Match, to tracer measurements using ASUR data, Mark IV data, HALOE data or MIRA data, to vortex averaged loss calculations with sonde data or GOME data and to the SLIMCAT 3D chemical transport model. All profiles obtained by these methods are convoluted to the vertical resolution of the RAM in order to gain meaningful and comparable results. Where possible, comparable time scales have been chosen. While the beginning of the examined time period is not crucial due to the relatively low loss rates in December and January, all measurement periods were chosen to end around March 15. Further issues, which we will examine in detail in the next subsections, are the observed regions and principal differences in the methods.

4.6.1 Match

Match probes an air parcel with an ozone sonde at a given time and location and follows its path by trajectory calculations. When the air parcel passes another sonde launch site within a radius of 400 km, it is probed for a second time. The difference in the observed ozone mixing ratio at a certain isentropic level, corrected for the diabatic descent, is due to chemical loss. The descent rates used by Match are taken from the SLIMCAT model. The Match technique directly measures ozone loss in a Lagrangian way in contrast to all other methods, which depend on a sufficiently homogenous vortex. Care is taken in Match to avoid air masses that are not well conserved, for example by examining the divergence of nearby trajectories or by discarding trajectories with a large potential vorticity change. Further information can be found in [Rex et al., 1997, 1999, 2002].

The Match loss adds up to 1.0 ± 0.25 ppm at the 475 K level when convoluted to the vertical resolution of the RAM, in nice agreement with the RAM results. The loss is integrated between January 5, 2000 and March 16, 2000. The period is comparable to the RAM time frame, since little loss occurred between December 11, 1999 and January 5, 2000. Match results were available between 400 K and 550 K. Below and above these levels, no loss is assumed in order to perform the convolution needed for the comparison (see Appendix 4.D). The vortex edge is chosen to be 36 PVU, which is sligthly more extensive than our edge definition, but should yield no large difference. According to Rex et al. [2002], less ozone loss occurred at lower equivalent latitudes in this winter, so results may have a low bias in comparison to RAM. Since the cooling rates of SLIMCAT are lower than the rates of the RAM model (Figure 4.10), application of the RAM cooling rates to Match should lead to a higher cumulative loss, another low bias of the Match results.

4.6.2 Tracer Measurements

ASUR

The Airborne Submillimeter Radiometer ASUR is a microwave radiometer measuring in the 600 GHz range [von König et al., 2000]. While the measurement principle is identical to our instrument, observations have to be carried out above the tropopause due to the strong water vapor absorption in this frequency range. In the winter 1999/2000, the instrument was deployed at the NASA DC-8 aircraft for 23 flights. The first deployment lasted from November 30, 1999 to December 16, 1999, the second lasted from January 14, 2000 to January 29, 2000 and the third lasted from February 27, 2000 to March 15, 2000. The aircraft was based at Kiruna, Sweden (68° N, 20° E). Measured species comprise ozone, N_2O, HNO_3, ClO, HCl and some others. Profiles are derived from the spectra with the optimal estimation method. Altitude resolution for ozone and N_2O is about 6–10 km. The altitude range is 16–40 km for N_2O and 16–50 km for ozone. The data of ASUR need not to be convoluted due to the similar altitude resolution.

In Bremer et al. [2002], ASUR measurements of the chemically conserved tracer N_2O are used to mark air parcels. If the ozone mixing ratio at the same tracer mixing ratio level is compared at the begin and the end of the winter, the difference represents the ozone loss at this level, because tracer and ozone follow the same dynamics. Bremer et al. report a loss of 1.0 ± 0.1 ppm between the first deployment in December and last deployment in March at the 100 ppb N_2O level (approximately 470 K), which is in nice agreement with our method within the error bars. The calculations use the mean profiles of the deployments and the time period is comparable to our measurements.

We will add some general remarks in regard to tracer methods here. Care has to be taken that no mixing of extra vortex air occurs in the considered time period [Plumb et al., 2000]. While large scale mixing of extra vortex air was negligible in this winter from January on [Richard et al., 2001], other types of mixing can not be excluded categorically. However, horizontal mixing due to spatial differences of the descent rates inside the vortex should not have been significant in 1999/2000 [Ray et al., 2002]. Another issue is the choice of the initial profiles of tracer and ozone, which is somewhat arbitrary. While the ASUR measurements are using vortex means, the following methods use single profiles, which can introduce errors of about 20% [Rex et al., 2002; Harris et al., 2002]. Initial profiles need to be measured late enough to allow for a stable vortex, but early enough to avoid any ozone loss. Ozone loss should be negligible in the 1999/2000 winter if the profile was obtained around December, but some mixing occurred in that time period. According to Müller et al. [2002], mixing should have led to an underestimate of ozone loss here. Additionally, tracer measurements usually involve only two measurement dates, so loss rates can not be deduced.

Mark IV

The Mark IV balloon interferometer is an FTIR spectrometer measuring in the 650 cm^{-1} to 5650 cm^{-1} region [Toon, 1991]. Since it measures over 30 species at the same time, its data will appear in several other applications in the following. The vertical resolution of the measurements is about 2 km. The interferometer was launched two times on board of the OMS balloon gondola, on December 3, 1999 (sunset) and on March 15, 2000 (sunrise). The launch site was Esrange, Sweden, near Kiruna. Additionally, ground measurements took place between the launches. The first launch took place inside the developing vortex, while the second launch happened on the day the vortex broke up. Potential vorticity was at 54 PVU this day, but until the next day, it dropped to 26 PVU. Since we cannot be sure that only vortex air was sampled, we have also examined data of the OMS balloon launch from March 5, where only in situ measurements took place.

N_2O is used again as a chemically conserved tracer. The loss is calculated between the launch in December and the launches at March 5 or March 15. Results are convoluted to our altitude resolution. Surprisingly, both measurements show very low losses. While the measurement on March 5 shows a loss of 0.5 ppm, the measurement on March 15 yields 0.4 ppm at the 475 K level. The first result may be explained by the high loss rates between March 5 and March 15. Comparison with Match results for March 5 shows agreement within the error bars, although the OMS results are situated at the lower end of the error range. The March 15 measurements were obviously disturbed by extra vortex air, which is also apparent in the measured denitrification, see section 4.10.

HALOE and Mark IV

In Müller et al. [1996, 2002], the chemically conserved tracer HF is used to mark air parcels. The ozone and HF measurements are taken from the HALOE solar occultation instrument on board the UARS satellite. The initial tracer profile used is an HF profile derived from measurements of the Mark IV instrument on December 3, 1999. HALOE data have been taken from measurements between March 11, 2000 and March 14, 2000 around 65° N. Results were available between 380 K and 550 K, and were treated like the Match data for the convolution. The vertical resolution of HALOE is 2–3 km for ozone and 4.5 km for HF. The HALOE loss adds up to 1.3 ± 0.4 ppm at the 475 K level. The vortex edge was set to 50 PVU for the selection of the HALOE measurements. This is roughly comparable to the vortex edge according to the Nash criterion at March 14. A discussion of the possible effect of the restricted latitude range of HALOE measurements can be found in [Hoppel et al., 2002] for a similar problem of the POAM instrument. Here, an additional uncertainty of 0.1 ppm is estimated. Another issue is the restriction of HALOE measurements to sunlit areas, which may slightly enhance the observed ozone loss. Ozone loss may also be enhanced by the longer time period in comparison to the RAM. Nevertheless, the agreement of both methods is good within the error bars.

MIRA and FTIR at Kiruna

Kopp et al. [2002] have used data from the ground based microwave radiometer MIRA and an FTIR instrument. Both instruments were located at Kiruna. The altitude range for MIRA is 17–55 km, with an altitude resolution of 7 km for ozone and 12 km for N_2O. The altitude range for FTIR ozone is 5–35 km with a resolution of 7.5 km and the altitude range for FTIR N_2O is 0–30 km with a resolution of 10 km, so the data need not to be convoluted to our altitude resolution.

N_2O or HF from the FTIR instrument have been used as a tracer with similar results. Ozone loss has been calculated from vortex averaged measurements. The early winter profile was deduced from measurements between January 22 and February 3 and the spring profile was deduced from measurements between March 4 and March 12. With ozone from MIRA, the loss adds up to 1.4 ± 0.4 ppm at 475 K, while ozone from the FTIR shows 1.1 ± 0.2 ppm loss. Agreement with the RAM method is good again. The shorter time period may lead to a low bias of the MIRA/FTIR data. The vortex edge is chosen to be 42 PVU, which is similar to our edge definition in the considered time periods.

4.6.3 Vortex Averaged Measurements

Sondes

Vortex averaged sonde profiles have been calculated by Rex et al. [2002]. Ozone sondes are launched at several sites all over the Arctic. Sondes launched inside the polar vortex have been binned into 10 day bins here and averaged. Heating rates were again taken from SLIMCAT. The inferred loss profile is very similar to the Match profile (Figure 4.15), so that the convoluted loss should be very similar to the convoluted Match loss. Since the agreement is so excellent, we do not need to compare the data directly and can refer to the Match results here.

GOME

GOME is an ultraviolet and visible light spectrometer on board the ERS-2 satellite measuring in nadir geometry [Hoogen et al., 1999]. Ozone depletion is determined by a method developed by Eichmann et al. [1999]. There are several similarities in the GOME and RAM methods: Ozone profiles are obtained by using the optimal estimation method. The calculation of the vortex averaged ozone depletion is similar to the RAM approach, including the use of exactly the same MIDRAD radiative transfer code. However, there are some important differences: The ground pixel area observed by GOME is about 960×100 km^2 and there are no measurements during the polar night. This limits the comparison to the period after early February. In addition to this, GOME uses no passive profile and simply integrates the loss rates. GOME altitude resolution is about 6–10 km. Thus, measurements need not be convoluted due to the similar vertical resolution. However, a comparison of GOME data to high resolution sonde profiles shows surprisingly good agreement, a fact that may introduce errors in the comparison.

The cumulative loss obtained by GOME after February 13, 2000 (line with asterisks) is shown in Figure 4.7. Loss rates are higher than the results of the RAM and SLIMCAT calculations and add up to 0.9 ± 0.3 ppm until March 17 [Eichmann, 2002]. The difference between RAM and GOME is well within the error bars of both measurements (considering the shorter time period used for GOME), but it should be noted that a comparison is difficult due to the reasons stated above and that the cumulative loss lies at the upper end of the range of results.

The RAM and GOME cooling rates are shown in Figure 4.10. The slight differences between the cooling rates of RAM and GOME can only be due to the input data for the model. The vortex edge was chosen to be 38 PVU, which is quite extensive and should have lowered the loss rates, but this effect cannot be observed.

4.6.4 SLIMCAT

SLIMCAT is a three-dimensional chemical transport model developed at the University of Cambridge. The model is initialized in October 1991 and is forced with U. K. Meteorological Office (UKMO) temperatures and wind fields. An overview over the model can be found in [Chipperfield, 1999]. The model runs at a resolution of $5^\circ \times 7.5^\circ$ (latitude $\times$ longitude) and is computed on 24 isentropic levels from 330 K to 3000 K. Vertical transport between the levels is calculated by the MIDRAD scheme. On November 1, 1999 a high resolution integration with a resolution of $2.5^\circ \times 3.75^\circ$ is started [Sinnhuber et al., 2000]. Gas phase chemistry is calculated for over 30 species and chemical families and over 100 chemical and photochemical reactions, including all reactions given in the introduction. Heterogenous chemistry is calculated on liquid, NAT and ice particles, which are assumed to be in equilibrium instantly in all areas with $T > T_{\mathrm{NAT}}$, $T_{\mathrm{NAT}} > T > T_{\mathrm{ice}}$ and $T < T_{\mathrm{ice}}$, respectively. This simple scheme must lead to an overestimation of stratospheric cloud occurrence and chlorine activation, since not all areas below the formation temperature of the clouds are actually filled with clouds.

The denitrification scheme is based on two different schemes. In the first scheme, ice particles of 10 μm radius removing HNO_3 from the gas-phase as co-condensed NAT form below the frost point and NAT particles with 1 μm form above the frost point (number density is about 10 cm^{-3} here). Fall velocities are 1500 $\mathrm{m/day}$ and 40 $\mathrm{m/day}$. The second scheme is based on NAT rocks. NAT is assumed to form here in two modes with radii of 0.5 μm and 6.5 μm without the formation of ice particles, based on the observations of Fahey et al. [2001]. The first mode forms with a number density of 1 cm^{-3} and HNO_3 condensed in excess is assigned to the large mode. Fall velocities are 1 $\mathrm{m/day}$ and 1100 $\mathrm{m/day}$. More information about the denitrification schemes can be found in [Davies et al., 2002], where the runs are called UKICE and UKNAT, respectively.

Since the cumulative ozone loss is virtually identical for the two schemes, we will come back to the second run later when we examine the chlorine activation and denitrification, where both runs show large differences. For the comparison, the SLIMCAT model has been convoluted to the vertical resolution of the RAM and interpolated to the position of Ny-Ålesund. Thus, the vortex edge definition is the same as for the RAM method. The modeled mixing ratio at the 475 K level shows excellent agreement with the RAM measurements, as depicted in Figure 4.5 (thin line).

Ozone loss in the SLIMCAT model is determined by comparison with a passive ozone tracer, which is initialized with the modeled ozone on December 1, 1999. Figure 4.7 shows the cumulative loss obtained by the SLIMCAT model (thin line), which adds up to 1.3 ppm (46%) at the end of the winter. This agrees remarkably well with the cumulative ozone loss from RAM measurements. Even

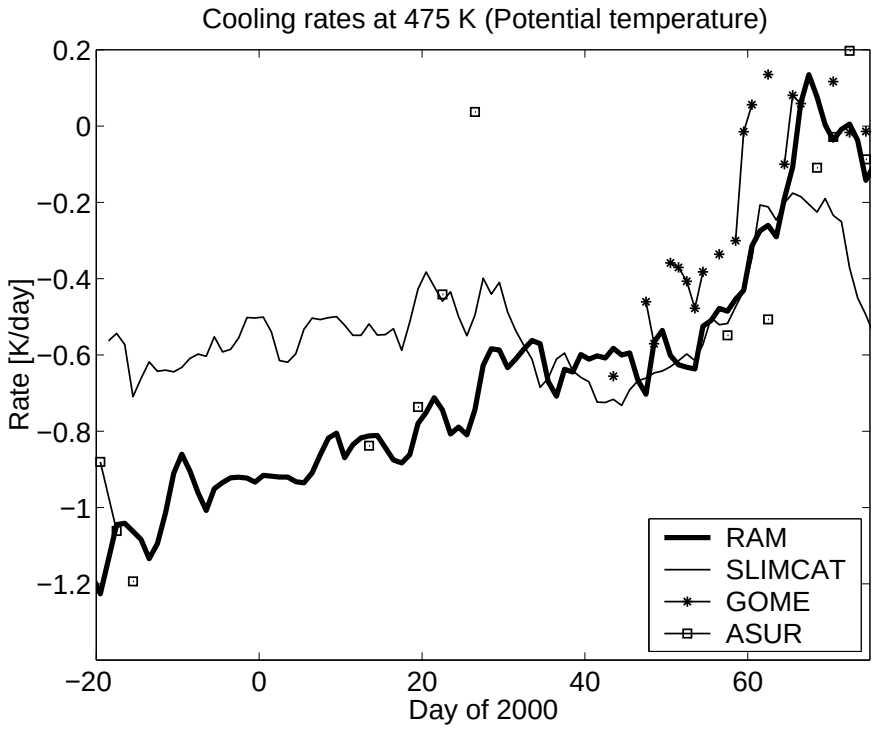

Figure 4.10: Cooling rates at the 475 K isentropic level in 1999/2000. Rates are given as potential temperature change $(\mathrm{d}\Theta/\mathrm{d}T)Q$ per day. Results are shown from the MIDRAD schemes of RAM (thick line), SLIMCAT (thin line), GOME (asterisks) and ASUR (squares).

the loss rates agree well, with relatively low loss rates up to the end of January and higher loss rates in February and March.

It is interesting to note that the derived ozone loss matches the RAM calculations, although the cooling rates used for RAM and SLIMCAT are quite different. The cooling rates for the two radiative transfer models, which are shown in Figure 4.10, differ by a factor of two until the end of January, when they converge. The larger cooling rates of the RAM model cause a stronger descent for the RAM passive ozone profile, which in turn must lead to a higher passive ozone mixing ratio for the RAM in the lower stratosphere, due to the positive gradient of the mixing ratio with respect to altitude.

Since the observed ozone mixing ratios agree well with the modeled mixing ratios (Figure 4.5), this should lead to higher ozone loss rates in the RAM calculations than in the SLIMCAT model. But as shown in Figure 4.11, higher mixing ratios in the RAM passive profile can only be observed below the 475 K level. The plot shows the RAM passive profile from March 10, 2000 (thick line), the SLIM-

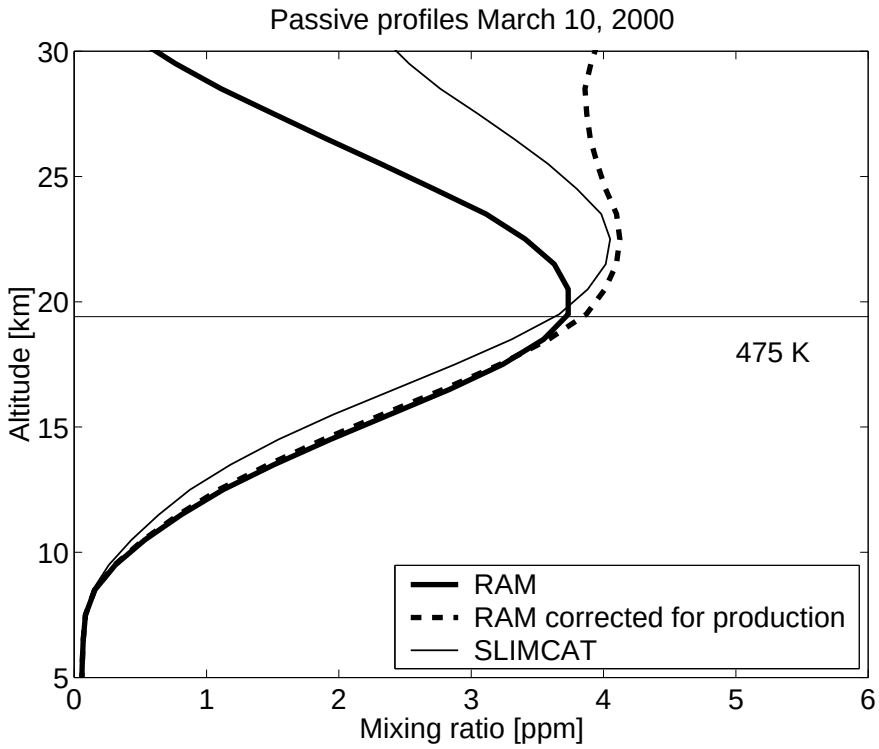

Figure 4.11: Passive profiles of the RAM ozone loss calculations (thick solid line) and the SLIMCAT calculations (thin solid line) at March 10, 2000. The dashed line shows a passive profile with simulated photochemical production (see text).

CAT passive profile of the same day (thin line) and the 475 K level. The reason for the similar mixing ratios of the passive profiles at the 475 K level is a combination of the descent rates increasing with altitude (Figure 4.4), neglected photochemical production and the convolution to the vertical resolution of the RAM. Air masses in the upper stratosphere descend considerably faster than in the lower stratosphere, and cause the ozone maximum in the passive profile to be squeezed and the maximum of the mixing ratio to descend in the course of time. Passive ozone is very effectively transported down to altitudes around 25 km, where the descent rate begins to decrease. In reality, photochemical cycles and horizontal motion fill up the profile above 35 km, because photochemical equilibrium is achieved here in some days [Sinnhuber et al., 1999]. This natural effect is not considered in the passive profiles, leading to a strong decrease in the passive ozone volume mixing ratio at altitudes around 25 km. In addition to that, horizontal motion is implicitly considered in the SLIMCAT profile, but not in the RAM profile.

Accordingly, the difference between the observed or modeled profile and the passive profile shows the net effect of missing photochemical production and chemical loss. In the course of time, the peak of the RAM passive ozone profile overtakes the peak of the SLIMCAT passive profile. In the convolution process this difference is propagated to the 475 K isentropic level and even below. At the end of the ozone loss calculation period, both profiles intersect at the 475 K level as displayed in Figure 4.11. This effect would not appear in the high resolution passive profile at 475 K, because the air masses here descent for only about 3 km in the whole winter, so that even at the beginning of the winter, the considered air masses would have been below 25 km. The impact of slight differences in the initial RAM and SLIMCAT passive profiles is negligible compared to the described effect.

A possible workaround for this problem is to simulate the natural ozone production in the passive profile. Since we can assume that transport plays no role above 50 km, we just can set the passive profile to the initial value above this altitude, regardless of the considered day. Between 35 km and 50 km, we take into account that equilibrium is achieved slower with decreasing altitude, so that only a part of the profile can be filled up before it descents to areas where the equilibrium time is longer. We take the initial passive profile here, multiply it with a factor falling from 1 at 50 km linearly to 0 at 35 km and add the resulting mixing ratio to the passive profile of every considered day. The resulting passive profile is shown in Figure 4.11 as a dashed line. If we calculate ozone depletion with the new passive profile, the cumulative loss adds up 1.4 ppm, about 0.2 ppm more than before. Figures 4.6 and 4.7 already show the corrected cumulative loss.

4.7 Accuracy of the Heating Rates

Since the descent rates are most critical for the accuracy of the determined ozone loss rates we have compared the RAM, SLIMCAT, ASUR and GOME rates to tracer observations. In Figure 4.12 we show the descent rates in km/day calculated from the cooling rates given by the radiative transfer models. The thick line represents the RAM cooling rates, while SLIMCAT is depicted by the thin line, ASUR by the squares and GOME by the asterisks. The shown SLIMCAT cooling rates are vortex averages and are not necessarily exactly the same as the ones apparent over Ny-Ålesund that were used for the SLIMCAT passive profile and ozone profile. It is assumed here that differences are sufficiently small. N_2O tracer measurements carried out with ASUR [Bremer et al., 2002] and with the Mark IV instrument on board the OMS balloon are shown as straight lines with dots marking the measurements. Note that the descent rates derived from the N_2O observations depend on very few measurements only and that a constant descent

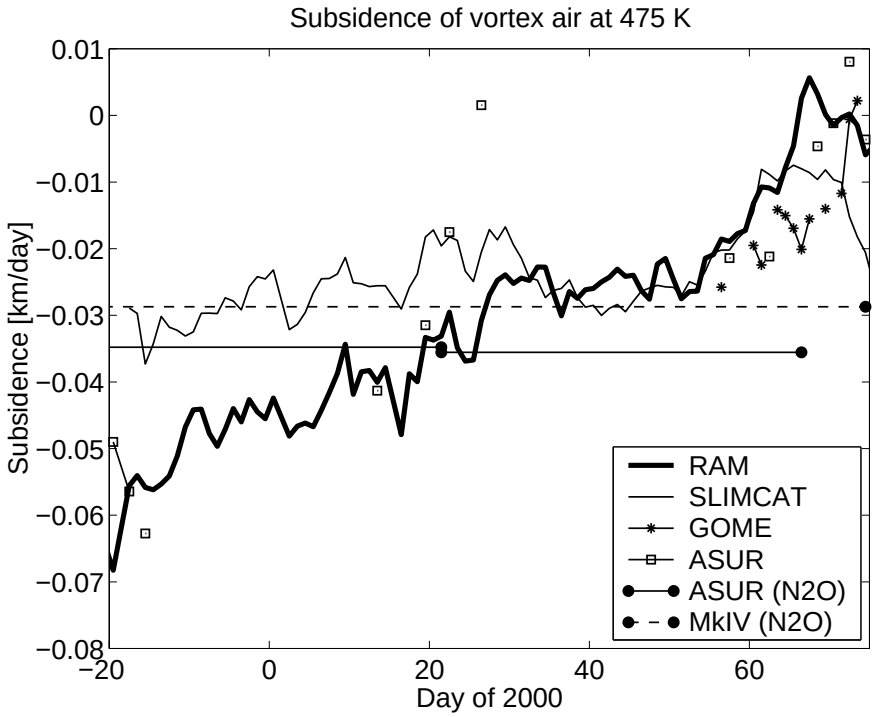

Figure 4.12: Subsidence at the 475 K isentropic level in 1999/2000. Subsidence $\mathrm{d}z/\mathrm{d}t$ inferred from the heating rates of RAM (thick solid line), SLIMCAT (thin solid line), ASUR (squares) and GOME (asterisks). Subsidence calculated from tracer measurements of N_2O (from ASUR and Mark IV) is shown for comparison.

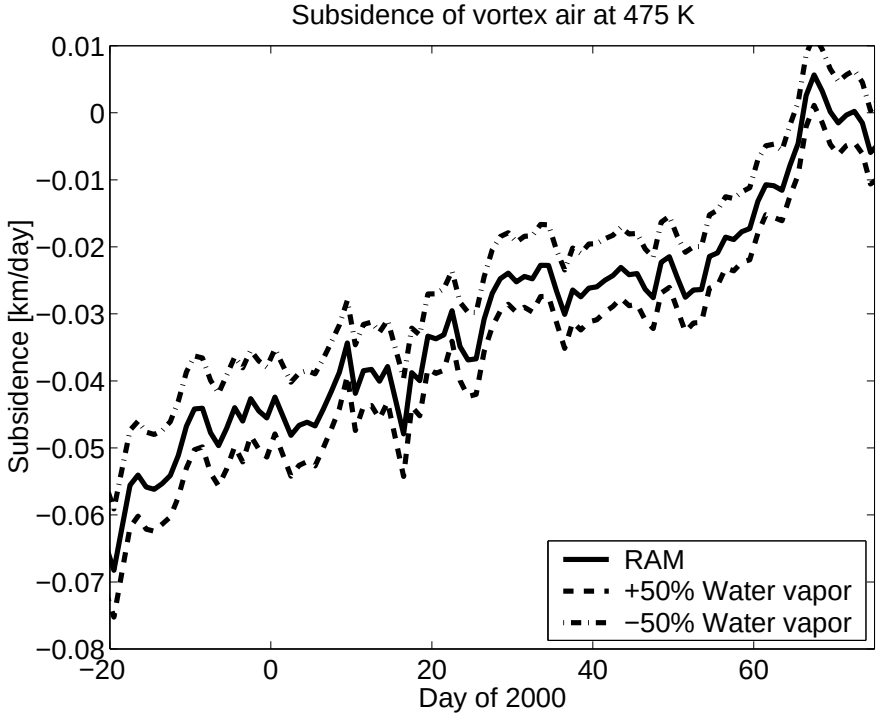

Figure 4.13: Effect of water vapor on the subsidence at the 475 K isentropic level. Subsidence $\mathrm{d}z/\mathrm{d}t$ inferred from the heating rates of RAM model without changes (solid line) and with water vapor mixing ratios increased and decreased by 50% (dashed lines).

rate was assumed in between measurements. The modeled descent rates (and thus the cooling rates) differ significantly from the measurements in some time periods. Especially, measurements indicate that the RAM cooling rates are too high in December, which would lead to an overestimation of ozone loss rates by our method. Most deviations in the models can be explained by errors in the heating rates of 0.2 K potential temperature change per day, except for the large discrepancies in December (see Figure 4.10). Thus, we have chosen an error of 0.2 K/day to calculate the error due to diabatic descent in the cumulative loss and the loss rates. The discrepancies in December are assumed to result from an unexplained systematic error. This short analysis also clearly indicates the need to provide more tracer observations inside the polar vortex.

We will now examine the reasons for the errors in the heating rates. Main error sources in all radiative transfer models are the input parameters, especially water vapor, albedo and the fact that clouds are neglected. One of the differences between the models is a global correction of the cooling rates in SLIMCAT to obtain no divergence in the mass flux. The vortex edge definitions do not play an important role as error source. Runs of the RAM calculations with fixed vortex edges gave the same result for the cumulative loss as the run with the definition of Nash.

Since water vapor is known so badly, a sensitivity analysis has been carried out. The heating rate calculations have been started with water vapor mixing ratios reduced by 50% and increased by 50% in every altitude. The resulting descent rates are shown in Figure 4.13, in the same scale as in Figure 4.12. It is evident that the discrepancies between the different measurements and models cannot solely be attributed to the uncertainty in the water vapor model.

Another approach to test the accuracy of the heating rates is to compare the actual potential vorticity change due to diabatic effects with the change indicated by the radiative transfer model. The change of the potential vorticity is in good approximation given by

$$\frac{\mathrm{d}P}{\mathrm{d}t} = P\frac{\mathrm{d}\hat{Q}}{\mathrm{d}\theta} - \hat{Q}\frac{\mathrm{d}P}{\mathrm{d}\theta} \tag{4.5}$$

where $\hat{Q} = (\mathrm{d}\Theta/\mathrm{d}T)Q$ is the heating rate in potential temperatures. Thus, the change of the vortex mean potential vorticity has been calculated with the RAM heating rates and has been compared to the mean potential vorticity from the ECMWF analysis. Results are shown in Figure 4.14, upper panel. The thin line shows the evolution of the mean potential vorticity in the vortex at the 475 K level according to ECMWF data. The thick line is the calculated evolution according to the computed heating rates. Agreement is excellent, and the resulting deviations can be explained by errors smaller than 0.2 K in the heating rates in the

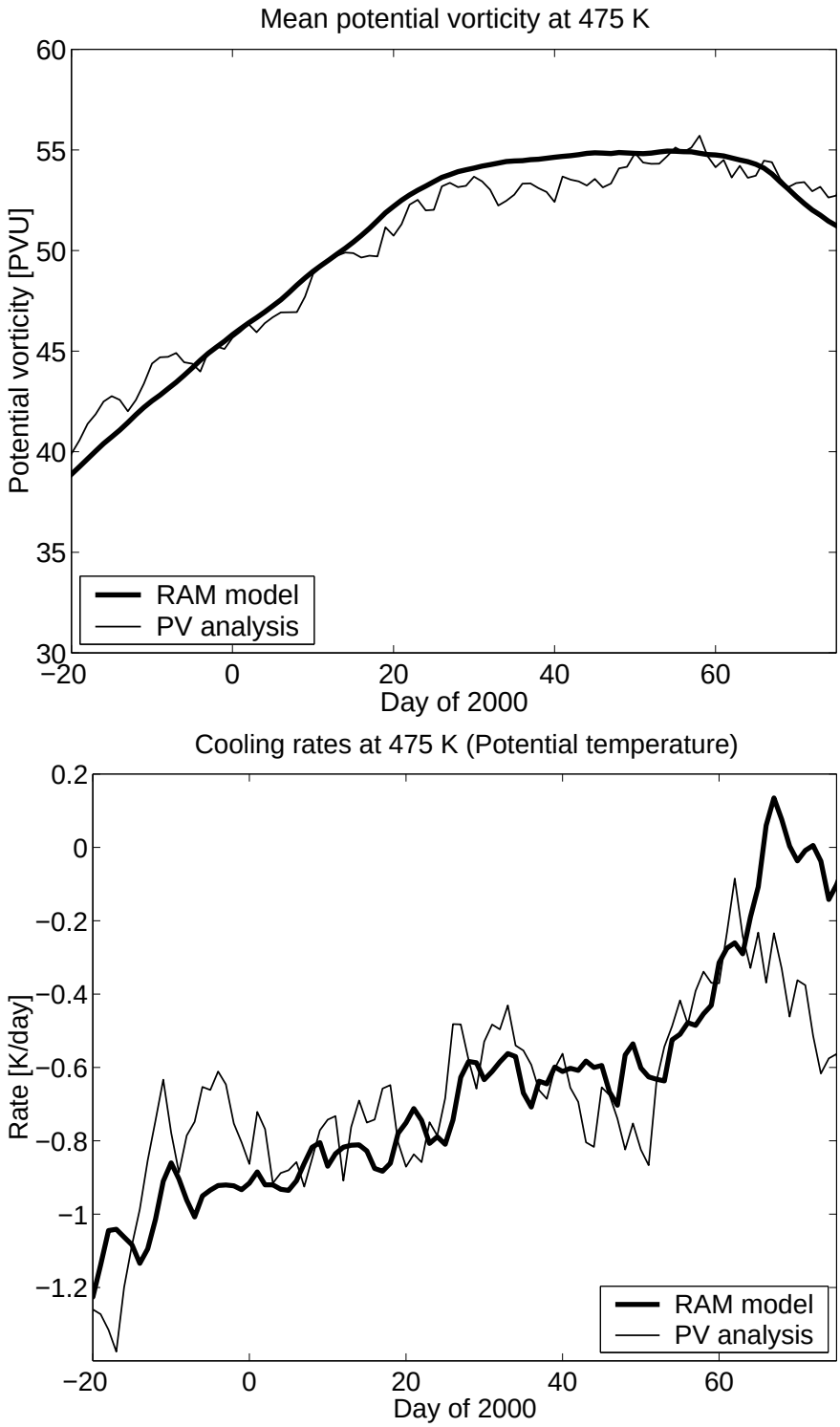

Figure 4.14: Potential vorticity evolution at the 475 K isentropic level in 1999/2000. Upper panel: Vortex mean potential vorticity calculated from the RAM heating rates (thick line) and from the ECMWF analysis (thin line). Lower panel: Heating rates (in potential temperatures) from the RAM calculations (thick line) and inferred from the ECMWF analysis (thin line).

most cases. This is shown in the lower panel, which displays the heating rates obtained from the ECMWF analysis when solving Equation 4.5 for $\hat{Q}$ (thin line) and the heating rates from the RAM model (thick line). The error range agrees well with the error range that can be deduced from the tracer measurements. Only in March a systematic deviation can be observed. Interestingly, the tracer measurements show the largest deviations in December. Thus, the deviation in March of the ECMWF analysis may be due to non-adiabatic effects like the dissipation of the vortex by waves. However, a final conclusion which heating rates are correct cannot be reached.

4.8 The General Picture

During the SOLVE/THESEO campaign many more than the studies mentioned already have been performed, providing the best opportunity yet to compare the different methods. The methods discussed in the last sections are summarized in Table 4.1. Although the investigated periods, isentropic levels and altitude resolutions are slightly different in some cases, the results should be comparable. An exception is the result of GOME, where the time period is considerably shorter. The agreement of all measurements is very well inside their error bars.

It is also very interesting to have a look at the many results that have been derived from high resolution measurements. Most studies agree that loss was occurring in a relatively narrow layer with peak loss rates at the 450 K level. Observations from 13 studies around the 475 K level are shown in Table 4.2. The results of Match and vortex averaged sonde profiles are also shown in Figure 4.15. Again, the agreement between the different methods is quite well, with results somewhere between 1.7 ppm and 1.9 ppm in the most cases. Some notable outliers are the MLS measurements (very short measurement period and large corresponding error) and the low results of MSX (sparse sampling). In addition to the citations in the table, a comparison of high resolution measurements can be found in [Harris et al., 2002] and additional results are given in [Robinson et al., 2002], [Salawitch et al., 2002] and [Grant et al., 2002].

Dataset	Period	Loss in ppm	Reference
ASUR	30.11–16.12 to 27.2–15.3	1.1 ± 0.1	Bremer et al. [2002]
GOME	13.2–17.3	0.9 ± 0.3	Eichmann [2002]
Match	5.1–16.3	1.0 ± 0.25	Rex et al. [2002]
RAM	11.12–16.3	$1.2/1.4 \pm 0.4$	Klein et al. [2002]
FTIR	22.1–3.2 to 4.3–12.3	1.1 ± 0.2	Kopp et al. [2002]
MIRA/FTIR	22.1–3.2 to 4.3–12.3	1.4 ± 0.4	Kopp et al. [2002]
HALOE/Mark IV	3.12–11/14.3	1.3 ± 0.4	Müller et al. [2002]
SLIMCAT	11.12–16.3	1.3	Sinnhuber et al. [2000] Davies et al. [2002]

Table 4.1: Ozone loss estimates with low altitude resolution, at the 475 K isentropic level.

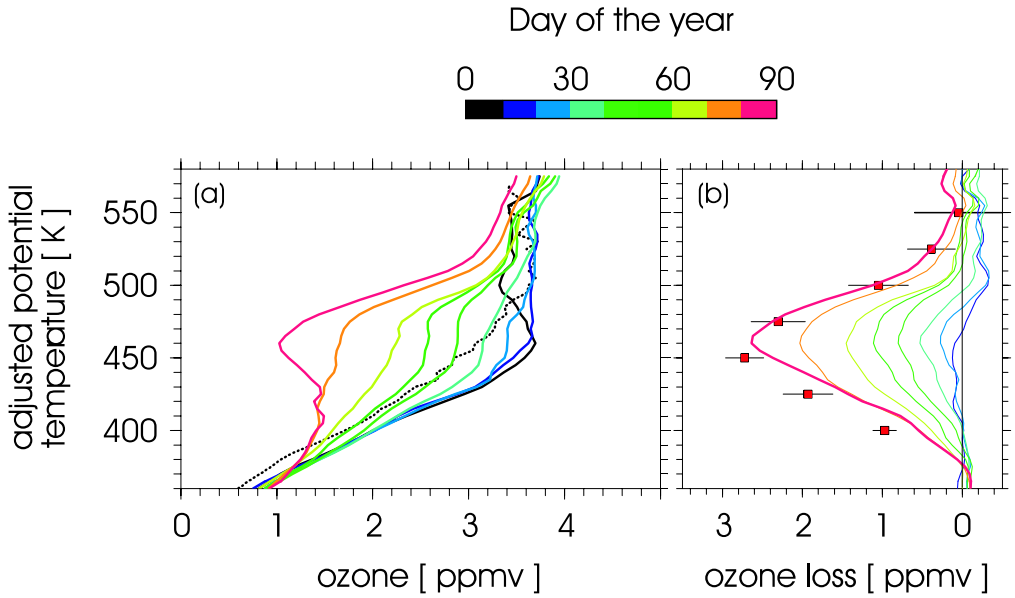

Figure 4.15: Ozone loss profiles from sondes and Match for the winter 1999/2000 between January and March. Left: Mean ozone profiles from sonde measurements, adjusted for diabatic descent. Gray scales correspond to the date given in the legend. Right: Loss profile inferred from the left panel (gray scale) and Match results for the loss profile (squares with error bars).

Method	Dataset	Isentrope	Period	Loss in ppm	Reference
Vortex average	POAM	475	1.1–15.3	1.8 ± 0.2	Hoppel et al. [2002]
Passive (Model)	POAM (REPROBUS)	475	11.1–15.3	1.9	Hoppel et al. [2002]
Vortex average	Sondes, DIAL, ARO-TEL, ER-2	470	10.1–17.3	1.74-2.01	Lait et al. [2002]
Tracer	HALOE/Mark IV	475	3.12–14.3	1.8 ± 0.4	Müller et al. [2002]
Match	Sondes	475	5.1–15.3	1.9 ± 0.3	Rex et al. [2002]
Tracer	MarkIV/ER-2	430–460	.1–5.3	1.0-1.5	Rex et al. [2002]
Tracer	MarkIV/ER-2	450	3.2–12.3	1.8 ± 0.3	Richard et al. [2001]
Vortex average	MLS	450	$2.2–13.2^{(1)}$	2.3 ± 0.6	Santee et al. [2000]
Vortex average	Sondes	475	1.12–15.3	1.3 ± 0.3	Schoeberl et al. [2002]
Vortex average	POAM III	475	1.12–15.3	1.3 ± 0.1	Schoeberl et al. [2002]
Trajectory ensemble	Sondes, POAM, DIAL, ARO-TEL, ER-2	475	1.12–15.3	1.4 ± 0.15	Schoeberl et al. [2002]
Vortex average	Sondes	450	20.1–12.3	1.7 ± 0.2	Sinnhuber et al. [2000]
Vortex average	MSX	400–500	23.1–4.3	1.0 ± 0.08	Swartz et al. [2002]

Table 4.2: Ozone loss estimates with high altitude resolution. Cumulative loss at the given isentrope and in the given period, except $^{(1)}$scaled for 52 days. All methods take diabatic descent into account. Adapted from [Newman et al., 2002] and the citations.

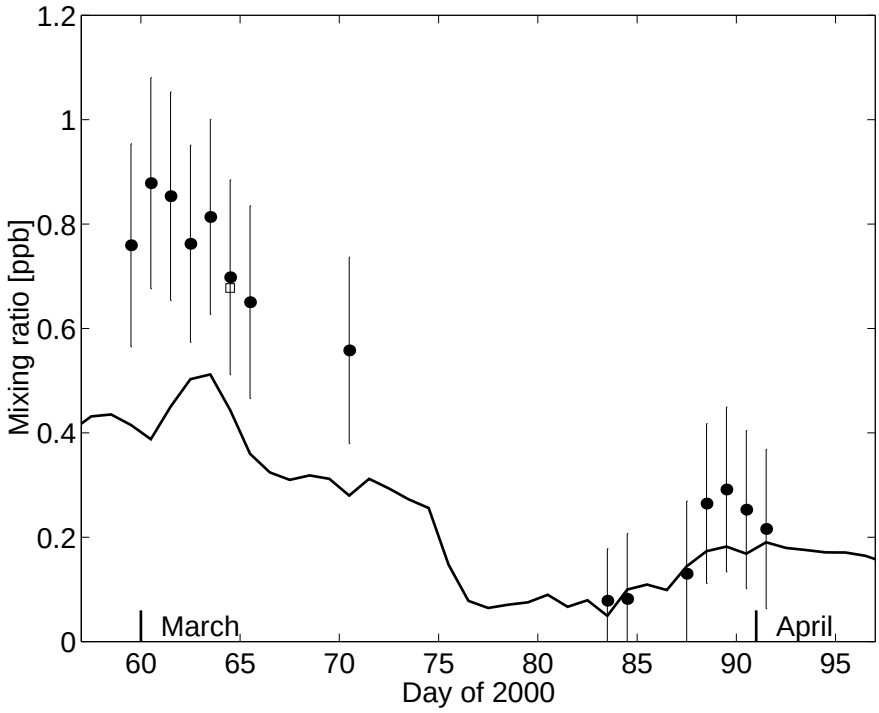

Figure 4.16: Chlorine monoxide mixing ratios at 475 K in March and April 2000. Shown are RAM measurements (dots with error bars) and an ASUR measurement (square) above Ny-Ålesund. The equilibrium chlorine monoxide mixing ratio above Ny-Ålesund calculated by SLIMCAT from the ClO_x mixing ratio is shown as a solid line for comparison.

4.9 Chlorine Activation

Ny-Ålesund is one of the very few sites where simultaneous observations of ozone and chlorine monoxide are routinely carried out. This provides a unique opportunity to validate the modeled relationship of these two species by comparison to their observed relationship. Chlorine monoxide observations in Ny-Ålesund are extremely dependent on good and constant tropospheric transmission. In a typical winter in Ny-Ålesund observations can be carried out on 10 to 20 days. In the year 2000 measurements were started on February 29. In an exceptionally long period of favorable weather conditions it was possible to obtain profiles on 7 successive days until March 6. This period was followed by bad weather until March 24 with only one observation on March 11. After March 24 uninterrupted measurements were possible until April 1 when the last data for the season were obtained.

In Figure 4.16 the chlorine monoxide volume mixing ratio at the 475 K isentropic level is shown for all days with sufficient data quality (solid black dots with

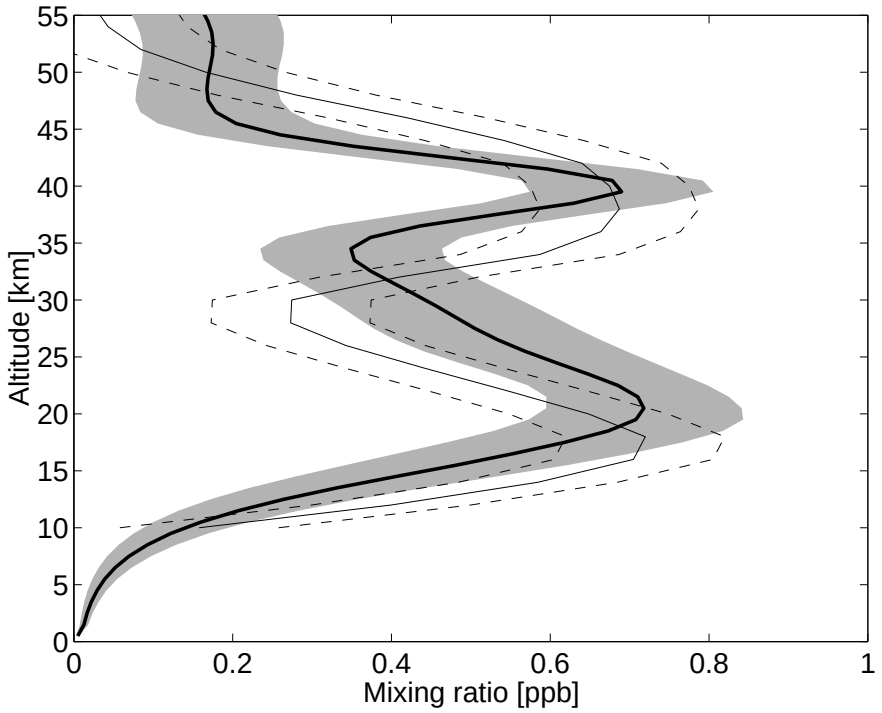

Figure 4.17: Comparison of chlorine monoxide profiles measured by RAM (thick line, shaded area denotes error bars) and by ASUR (thin line, dashed lines denote error bars) during a flight over Ny-Ålesund on March 5, 2000.

error bars). Observations started on day 59 (February 29) and reached a mixing ratio of 0.9 ppb on March 1. Between March 1 and March 11 we observed an almost linear decrease of the chlorine monoxide mixing ratio. Two weeks later chlorine monoxide showed undisturbed values. All measurements were taken inside the polar vortex or at the vortex edge, except for March 24 and 25, as shown in Figure 4.3. The period of enhanced chlorine monoxide is coincident with a period of pronounced chemical ozone loss at the 475 K level (see Figure 4.6). As the chlorine monoxide decreases between day 60 and day 70, the ozone loss rates decrease as well. However, this may be an artefact since the error bars are quite large.

Comparable chlorine monoxide profiles were observed inside the polar vortex by the ASUR radiometer [von König, 2001]. The altitude resolution of the ASUR profiles is almost the same as the RAM resolution, but systematic differences may be caused by the used a priori data. A profile measured during a flight over Ny-Ålesund on March 5 agreed within 0.2 ppb with the RAM chlorine monoxide profile, see Figure 4.17. The profile is also marked by a square in Figure 4.16.

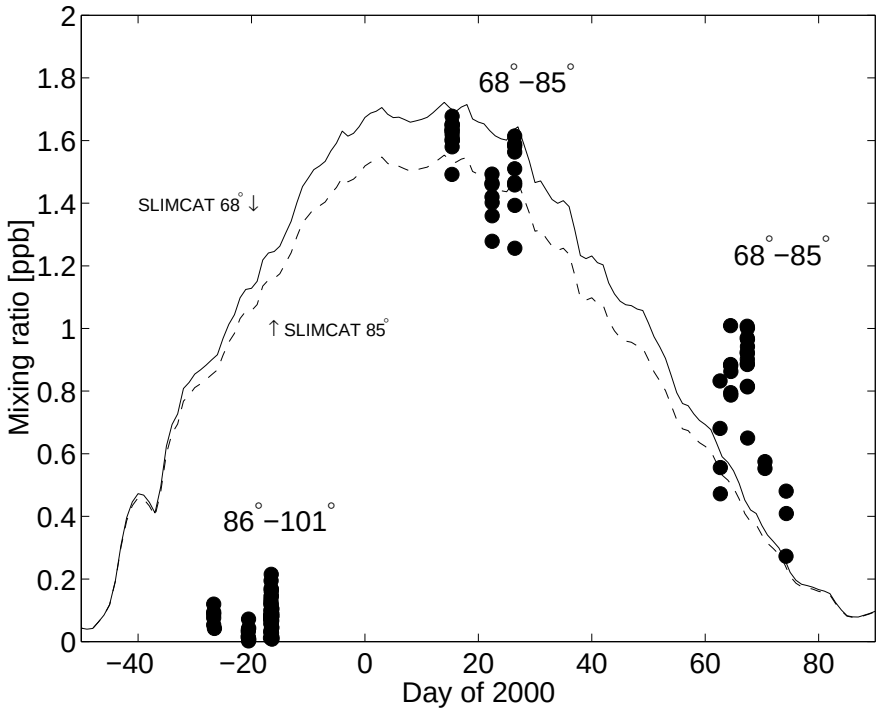

Figure 4.18: Chlorine monoxide mixing ratios at the 475 K level in the winter 1999/2000. Dots show measurements of the ASUR radiometer with an equivalent latitude greater 65° and solar zenith angles between 86°–101° (December) and equivalent latitudes greater 75° and solar zenith angles between 68°–85° (January and March). Equilibrium mixing ratios of chlorine monoxide inferred from the ClO_x value of SLIMCAT are shown for zenith angles of 68° (solid line) and 85° (dashed line).

Before we examine the RAM data in more detail, we will have a look at the general picture. In Figure 4.18, chlorine monoxide measurements for the whole winter performed by ASUR are shown. Data have only been measured during the three main phases of the SOLVE/THESEO campaign in early December, late January and late March. Unfortunately, there are almost no chlorine monoxide measurements available in between the phases from other instruments. Data from January and March have only been plotted if they had an equivalent latitude greater than 75° and a solar zenith angle between 68° and 85°. The first criterion ensures that data were measured in the vortex and the second one ensures that we only consider day measurements where photochemical equilibrium was achieved. Data from December have no constraint on the solar zenith angle, since it was too dark in this period. Here, all measurements with an equivalent latitude greater than 65° have been chosen and solar zenith angles were between 86° and 101°. Almost no

chlorine was activated in December. Since the vortex lay in almost complete darkness then and most chlorine set free from the reservoir gases should have been in the dimer (or Cl_2 and HOCl), this has to be expected. Chlorine monoxide mixing ratios peaked in January, dropped to moderate values in March and were back to almost zero in April (see the RAM measurements in Figure 4.16).

For comparison we have plotted the chlorine monoxide values of the SLIMCAT model for the same time period (Figure 4.16 and Figure 4.18, lines). The SLIMCAT results for the RAM measurements are obtained by subtracting modeled night profiles from modeled day profiles and subsequent convolution to the vertical resolution of the RAM profiles (see also Appendix 4.D). The chlorine monoxide value is calculated from the computed ClO_x value, where ClO_x is the long-lived sum of ClO and Cl_2O_2, under the assumption of photochemical equilibrium. The solar zenith angle used for the calculations is computed at noon respectively midnight at Ny-Ålesund. The SLIMCAT results for ASUR are obtained slightly different. The lines show the photochemical equilibrium value of chlorine monoxide for a solar zenith angle of 68° (solid line) and 85° (dashed line), calculated from the ClO_x value of the vortex mean.

In December, SLIMCAT predicts a pronounced chlorine activation. This is not expected due to the high solar zenith angles. Additionally, only little heterogenous processing occurred in early winter due to the warm temperatures and occasional polar stratospheric clouds. The few ASUR measurements that were not performed in complete darkness (less than 95° solar zenith angle) underestimate the SLIMCAT chlorine monoxide mixing ratios greatly. This is most probably due to an overestimation of the polar stratospheric cloud area in SLIMCAT, which in turn leads to an overestimation of the chlorine activation. As already stated, polar stratospheric clouds form instantly in SLIMCAT in all areas below T_{NAT}. In fact, polar stratospheric clouds were only observed sporadically in December in the areas that were cold enough for their formation. Additionally, the reservoir gas HCl showed no signs of activation. HCl measurements of the ASUR radiometer are compared to the SLIMCAT HCl calculations in Figure 4.20. HCl is transformed into active chlorine in the SLIMCAT model, but the measurements show undisturbed values around 1.75 ppb.

In January, the agreement between SLIMCAT and ASUR is quite well. Almost all measurements with solar zenith angles between 68° and 85° lie between the predicted equilibrium values. However, it is evident that the model underestimates the chlorine monoxide content compared to both instruments for the chlorine activation period from late February to mid March. After mid March the model is again able to reproduce the RAM measurements within their error bars.

We will also have a general look at the reservoir gases. As already stated, HCl from ASUR measurements shows undisturbed values around 1.75 ppb in December [Bremer et al., 2002], see Figure 4.20. Mixing ratios below 0.5 ppb in January

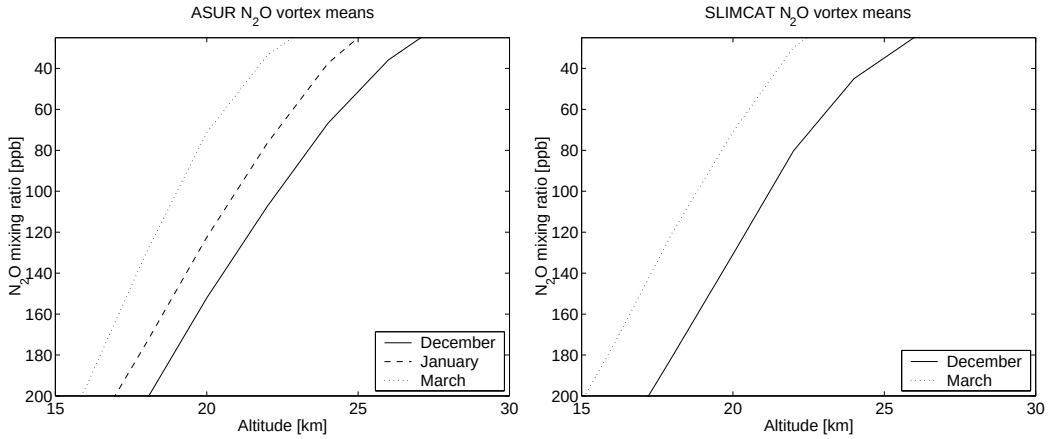

Figure 4.19: Vortex mean profiles of N_2O, used as an altitude scale in Figures 4.20, 4.21 and 4.23. Left: Vortex mean N_2O profiles measured by ASUR for December (solid line), January (dashed line) and March (dotted line). Right: The same for SLIMCAT N_2O. Adapted from [Kleinböhl et al., 2002].

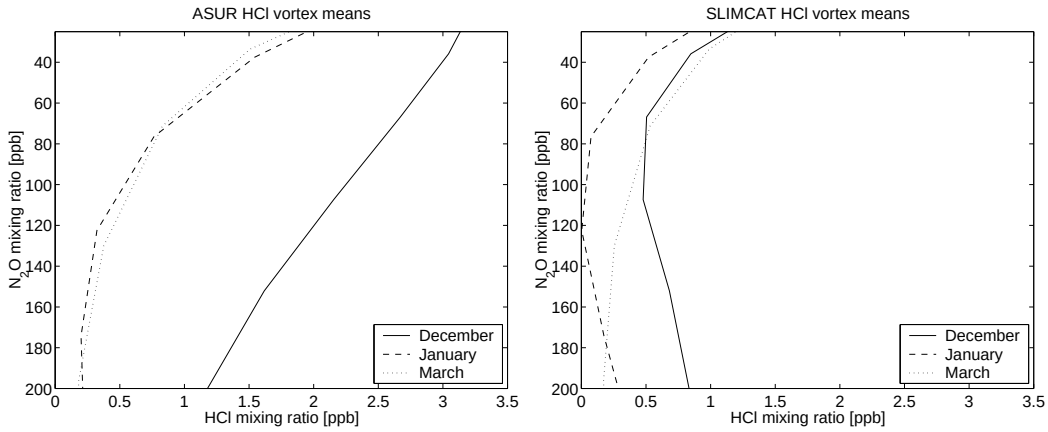

Figure 4.20: Vortex mean profiles of HCl. Left: Vortex mean HCl profiles measured by ASUR in December (solid line), January (dashed line) and March (dotted line). Profiles are plotted versus N_2O to eliminate diabatic descent. Right: The same for SLIMCAT HCl versus SLIMCAT N_2O. Adapted from [von König, 2001].

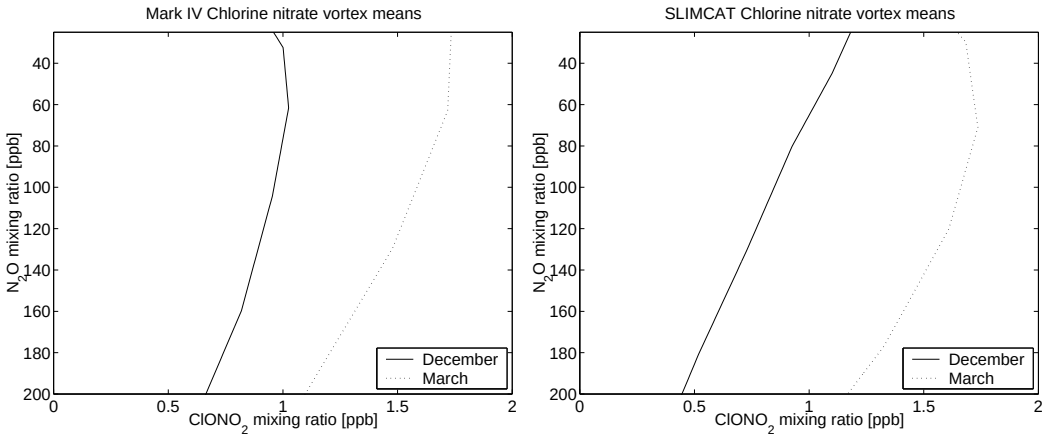

Figure 4.21: Vortex mean profiles of $ClONO_2$. Left: Vortex mean $ClONO_2$ profiles deduced from column measurements of ground based FTIR and Mark IV balloon profiles, for December (solid line) and March (dotted line). Profiles are plotted versus N_2O to eliminate diabatic descent. Right: The same for SLIMCAT $ClONO_2$ versus SLIMCAT N_2O. Adapted from Kleinböhl et al. [2002].

indicate high activation of chlorine. March mixing ratios were comparably low, which indicates deactivation first occurring into $ClONO_2$. $ClONO_2$ profiles were inferred from column measurements of the ground based Mark IV instrument in December and March [Kleinböhl et al., 2002]. In January, we examine profiles deduced from a Cl_y budget and ASUR measurements [von König, 2001]. Cl_y is the sum of all chlorine species here. Thus, the January $ClONO_2$ value is not independent of the other measurements in January. $ClONO_2$ shows undisturbed values of about 1.2 ppb in December, values of 0.75 ppb in January and more than 1.5 ppb in March, see also Figure 4.21. Increased values of $ClONO_2$ in March compared to December and low HCl values in March confirm that deactivation occurred first into $ClONO_2$. Chlorine deactivation was not completed in March. If no chlorine activation is assumed in December, Cl_y is in good approximation composed of HCl and $ClONO_2$ and adds up to about 3 ppb. In March, HCl and $ClONO_2$ do only add up to about 2 ppb, so that the remaining 1 ppb have to be activated as ClO, which is consistent with the ClO measurements of RAM and ASUR. This is a hint that the ClO measurements are correct and the model is in error here.

HNO_3, which is also measured by the ASUR instrument, decreased from 9.5 ppb in December to 6 ppb in March. Measurements that could be affected by HNO_3 removal from the gas phase by polar stratospheric clouds are already excluded [Kleinböhl et al., 2002]. The decrease is a clear sign for denitrifica-

tion, which is treated in the next section. Photolysis of HNO_3 into NO_x is not the major reason for the decline, which is also shown there. January results are inconclusive. Some HNO_3 measurements showed higher values than the December values, which is expected, since chlorine was highly activated and nitrate was set free from $ClONO_2$. Others showed first signs of denitrification.

We will now examine the reasons for the discrepancy between model and measurements in March. In contrast to the previous winter, when an overestimation by the model was found, the difference between model and measurement is apparently not caused by the atmospheric temperatures used for the model calculations [Klein et al., 2000]. The temperatures in 1998/99 were very close to the formation temperature of polar stratospheric clouds. Slightly too low temperatures used in the SLIMCAT model calculations caused a large difference in the subsequent chlorine activation. The cold bias of temperatures near the ice point in the UKMO analysis compared to sonde, NCEP or ECMWF data is a well known feature [Davies et al., 2002]. But the stratospheric temperatures during the 1999/2000 winter were clearly below the cloud formation temperatures in the model as well as in the ECMWF temperature analysis. In addition to that, the disagreement between modeled and measured chlorine monoxide would be rendered worse by the use of ECMWF temperatures.

A more detailed comparison of model and observed profiles is given in Figure 4.22. Here we present 12 of the retrieved chlorine monoxide profiles of the winter 1999/2000. Along with the profiles (thick lines with gray shaded error range) we have plotted the SLIMCAT model calculations in their original vertical resolution (dashed line) and convoluted to the RAM vertical resolution (thin line). It is evident that the narrow peak in the SLIMCAT model in the lower stratosphere is considerably broadened in the convolution process. A meaningful comparison is only possible between the RAM profiles and the convoluted model profiles. The agreement in the upper peak is not surprising, because the volume mixing ratio at these altitudes is dominated by the a priori information in both cases. However, the lower peak is underestimated by the model in all cases of enhanced chlorine monoxide, although it appears to have the same altitude as the peak in the RAM profiles at least.

The difference of the modeled profiles and the observed profiles in the lower peak might either be caused by the model underestimating the chlorine monoxide mixing ratio at the peak level or at altitudes between the peak and ~ 23 km where the differences between model and observations are largest. Both possibilities are compatible when the modeled profiles are adjusted to the RAM altitude resolution. To explore the discrepancy, further additional information is needed. The potential cloud area shown in Figure 4.2 indicates that temperatures in significant parts of the polar vortex were low enough for the formation of polar stratospheric clouds until mid March at the 475 K level (about 19.3 km at March 16) but only

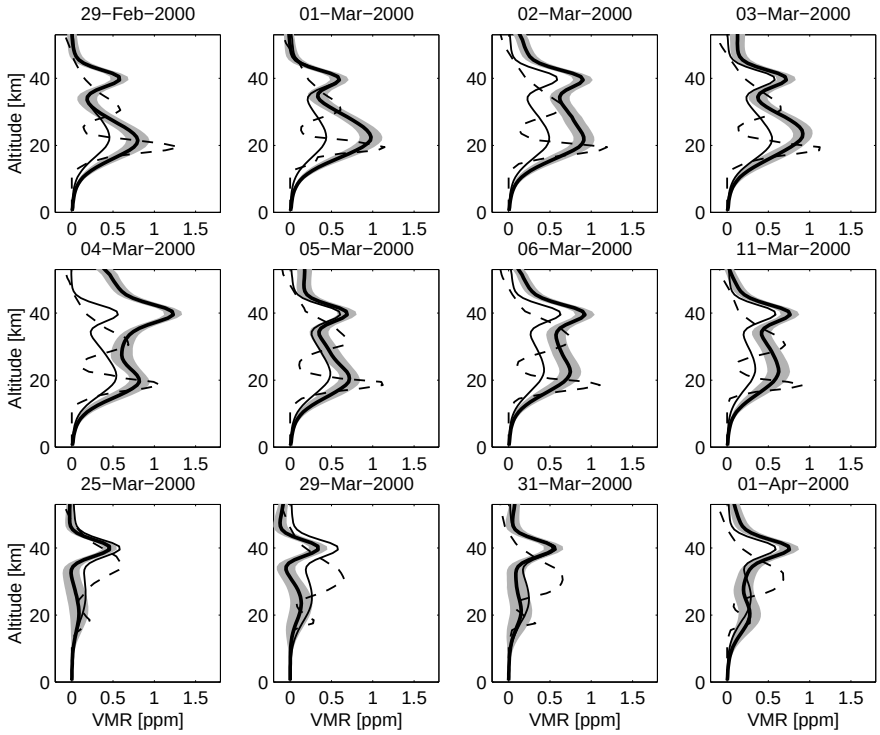

Figure 4.22: Chlorine monoxide profiles measured by the RAM in 1999/2000. Shown are 12 profiles measured at different dates (thick line, shaded area denotes the error bars) and SLIMCAT model calculations for the same date at their original resolution (thin dashed line) and convoluted to the RAM altitude resolution (thin solid line).

until the beginning of February at the 550 K level (about 22.1 km at March 16). This confirms the existence of an activated chlorine layer in the modeled profiles around 19 km and indicates that no chlorine was activated after early February around 22 km. But air masses at these altitudes were very probably denitrified by the stratospheric cloud activity seen earlier at the 550 K level (see Figure 4.2). This led to ongoing chlorine activation in March due to missing nitrogen compounds needed for the transfer of activated chlorine into the reservoir gases. Differences in denitrification between the model and measurements could account for the differences in the chlorine monoxide profiles.

4.10 Denitrification

The winter 1999/2000 showed the most severe and widespread denitrification ever observed in the Arctic stratosphere [Popp et al., 2001; Davies et al., 2002; Kleinböhl et al., 2002]. However, no significant dehydration was observed. We will have a closer look at the different studies now. Popp et al. measured denitrification by the use of data of the Mark IV instrument and of flights of the NASA ER-2 aircraft, while Kleinböhl et al. used data of the ASUR instrument and the Mark IV instrument. Davies et al. give a detailed study of the denitrification in SLIMCAT compared to the ER-2 measurements. Results of MLS [Santee et al., 2000], which were also available, are very rough estimates and not suitable for a meaningful comparison.

In the study carried out by Kleinböhl et al. [2002], denitrification is derived from combined results of ASUR measurements (HNO_3), ground based FTIR and Mark IV balloon measurements ($ClONO_2$) and model estimates of NO_x. Denitrification is inferred from the difference in NO_y between December 1999 and March 2000, where NO_y is the sum of the relevant odd nitrogen species $ClONO_2$, HNO_3 and NO_x. Subsidence is accounted for by calculation on N_2O levels.

A detailed comparison is carried out between the SLIMCAT run with UKMO temperatures and the ice denitrification scheme and the ASUR method, see Figure 4.23. SLIMCAT results have been convoluted to the altitude resolution of ASUR, which is comparable to the resolution of the RAM. Both vertical profiles of the difference in NO_y between December and March (called ΔNO_y from now on) imply that the air was denitrified until mid March at altitudes between 16 and 21 km, and that denitrification was increasing with altitude. Furthermore, the ASUR method shows a stronger denitrification than the SLIMCAT model. At the 100 ppb N_2O level (equal to the 470 K level in March), ΔNO_y shows values of about 4 ppb for ASUR and 2.5 ppb for SLIMCAT. However, the error bars of the ASUR method are so large that the result is not statistically significant. Although it is not possible to conclude with certainty from the ASUR measurements that the denitrification was more pronounced than modeled by SLIMCAT, they also do not contradict this assumption.

Results from the different SLIMCAT model runs by Davies et al. [2002] point in the same direction. The run with UKMO temperatures and the ice denitrification scheme does not agree very well with measurements of NO_y by the NASA ER-2 flights between January 14 and March 12, which imply a higher denitrification throughout the observed altitude range (this can be seen very clearly in Figure 7 of the reference. High resolution ΔNO_y is about 10 ppb at the 460 K level in the data and 8 ppb in the model). The use of ECMWF temperatures renders the agreement even worse.

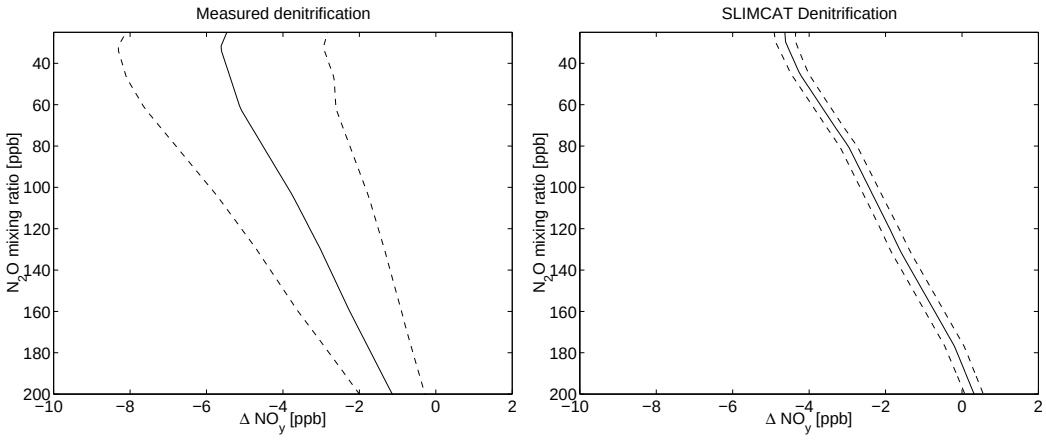

Figure 4.23: Denitrification profile. Left: Difference in NO_y between December and March inferred by the method described in [Kleinböhl et al., 2002]. The profile is plotted versus N_2O to eliminate diabatic descent. The dashed lines show the error bars. The right panels shows corresponding results from SLIMCAT.

However, the run with the simple parameterization of denitrification by large NAT particles agrees better with the observed ΔNO_y regardless of the used temperature data (ECMWF or UKMO, not shown here). This agreement is consistent with the observation that no dehydration occurred in the vortex, which would have taken place with ice particles. Denitrification first occurred in early February in both denitrification schemes, when the sunlight came back. Chlorine deactivation was delayed by about two weeks in March in comparison to 20 days for the NAT scheme. Denitrification occurring only after January would explain the agreement of ASUR and SLIMCAT in January. The rather short elongation of chlorine activation in the NAT and ice schemes may explain that the effect of different denitrification schemes on ozone loss is negligible (see below).

Interestingly, the ice denitrification scheme overestimates ClO_x in comparison with ER-2 measurements in the whole winter, which is just contradictory to our results. Unfortunately, since the ER-2 measured mainly at one altitude, no direct comparison to the RAM and ASUR data is possible due to the restricted altitude resolution. Similar discrepancies occur between $ClONO_2$ and HCl from the ER-2 and from the model, which additionally do not add up to the expected Cl_y budget. Thus, chlorine measurements yield no clear result in favor of one of the schemes, which is a pity, since the denitrification results show a quite clear picture.

Popp et al. [2001] also use results of the ER-2 to calculate denitrification, but instead of ER-2 data, Mark IV results from December 3 are used for the initial NO_y profile. However, the results are essentially the same as in [Davies et al.,

2002], and give about 10 ppb denitrification at the 475 K level. Denitrification was also calculated for the two Mark IV balloons between December 3 and March 15. Interestingly, it is significantly lower at all altitude levels than in the other studies (about 6 ppb at 475 K). This is another hint that the March 15 measurement of Mark IV may have been disturbed by extra vortex air. Popp et al. show that there was a dependence of the denitrification on equivalent latitude, which could explain the Mark IV result.

Thus, as a final conclusion, denitrification has been modeled by SLIMCAT for this winter, but the chlorine deactivation may have set in too early in the model scheme with ice denitrification.

4.11 Effect on Ozone Loss

The question remains, why the model can produce the correct ozone loss although it underestimates the chlorine monoxide significantly in March. The ozone loss rate is proportional to the square of the chlorine monoxide concentration, see for example [von König, 2001]. Thus, an underestimation of chlorine monoxide should lead to an underestimation of ozone loss. It could be argued that the ozone loss calculations correspond to vortex averages while the chlorine monoxide observations are restricted to one location only. If the chlorine monoxide observations and model calculations at Ny-Ålesund were not representative for the vortex consistency is not to be expected. But this is rather unlikely: If the measured chlorine monoxide would not be representative, it would be scattered around the chlorine monoxide model values and not be systematically higher for a period of weeks.

The answer may be that the discrepancy only lasted for a few weeks, but that ozone loss occurred from January to March. Davies et al. [2002] estimate that denitrification caused only 30% of the observed ozone decline at 460 K in the ice run. This was even true for the stronger denitrified run with the NAT scheme. Tabazadeh et al. [2000] suggest that 30% was an upper limit for the additional loss due to denitrification for a similar winter. Gao et al. [2001] obtain similar results for the loss due to denitrification based on the examination of air parcels with different denitrification histories. In any case, the effect of denitrification on ozone loss is strongly dependent on the timing of polar stratospheric cloud appearance, sunlight and denitrification. If denitrification would occur only in darkness and air masses would be renitrified later or stratospheric clouds activated all available chlorine regardless of denitrification, no additional loss is to be expected.

Considering our altitude resolution and the fact that at least a part of the denitrification was modeled by SLIMCAT, the difference may not be detectable in the ozone measurements. Replacing the ice denitrification scheme with the NAT

scheme even yields better results, since it agrees better with the chlorine measurements (not shown), but gives the same cumulative ozone loss. Discrepancies may also be caused by the different heating rates in the RAM radiative transfer model, the SLIMCAT model and reality or badly known rate constants such as that of the ClO–BrO reaction. Even the good agreement observed may be incidentally due to the large error bars connected with the ozone depletion calculations (about 30%) and chlorine measurements (about 20%) and the uncertainties in the model.

So it seems that we obtain a realistic ozone loss in SLIMCAT, although some runs underestimated chlorine monoxide. Interestingly, Davies et al. [2002] draw just the opposite conclusion. Because of the discrepancy of the ER-2 measurements and the microwave measurements of chlorine monoxide, they conclude that the run that produced the best agreement with denitrification and chlorine from ER-2 measurements (ECMWF with the NAT scheme) underestimated ozone depletion. Thus, a run with a correct ozone loss would have to overestimate chlorine (like it happened in the UKICE run in comparison to the ER-2 data). But they admit that uncertainties, caused for example by the heating rates or ER-2 measurement errors, are so large that a firm conclusion cannot be reached.

It should be noted that an underestimation of ozone depletion occurred quite often in model studies, even if chlorine was captured well, see for example [Deniel et al., 1998; Becker et al., 1998; Woyke et al., 1999]. It must be stressed here that the discrepancies can very much depend on the evolution of the winter, the model assumptions (which normally include a very crude approximation to denitrification and stratospheric cloud formation due to time constraints and a lack of better knowledge) and the accuracy of the measurements (which is not better than 20% for all known chlorine measurements). While SLIMCAT showed a general underestimation in earlier cold winters like 1994/1995, it agreed quite well with several ozone depletion calculations in 1999/2000, see for example [Sinnhuber et al., 2000]. Remarkably, this was the only winter where SLIMCAT produced significant denitrification, which may be a hint for the discrepancies.

A study similar to ours was conducted by Wu and Dessler [2001] for the Antarctic ozone depletion measured by MLS. They found a very nice agreement between modeled and measured ozone depletion for the winters of 1993 to 1995. Chlorine monoxide was constrained by measurements, so that discrepancies could be addressed to unknown chemistry, chlorine measurement errors or badly known rate constants. Dynamics are usually negligible in the Antarctic, so this error source could be excluded. The study of Wu and Dessler shows that the ozone loss cycles itself seem to be quite well understood qualitatively and quantitatively in the Antarctic. Thus, discrepancies between models and measurements in the Arctic could be due to dynamics, for example. Since chlorine monoxide was constrained in the model, no statement was made about the mechanisms setting free chlorine from the reservoir gases or denitrification. Thus, an error in the

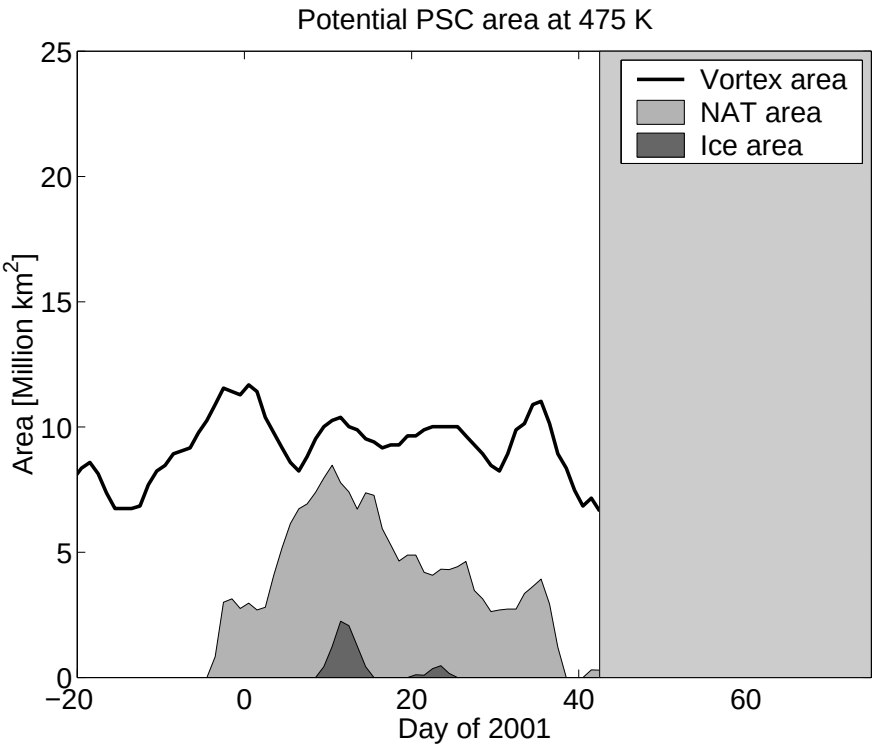

Figure 4.24: Potential PSC area in 2000/2001. Temporal evolution of the area of temperatures below the formation temperature of NAT (light gray) and ice (dark gray) at the 475 K level inside the vortex. The area of the vortex is shown for comparison.

exact modeling of denitrification in SLIMCAT, while the ozone loss cycles were modeled well, is a good explanation for the observed discrepancies in the Arctic according to Wu and Dessler [2001].

The final conclusion remains that uncertainties in measurements and models deny a firm answer in regard to the cause of the discrepancies for the time being. However, the basic mechanisms of ozone loss seem to be well understood nevertheless.

4.12 Ozone Depletion in 2000/2001

The winter of 2000/2001 was characterized by a weak vortex that only survived for little more than a month. However, for the time of its existence, temperatures were quite cold. The vortex formed in December but only gained strength at the end of the month. At the beginning of February, the vortex split up into two parts

and vanished in the next three weeks. Nevertheless, temperatures fell below the formation temperature of NAT clouds and even the formation temperature of ice clouds in large parts of the vortex, as presented in Figure 4.24. In Figure 4.25 the evolution of the vortex is shown. The vortex edge is only displayed up to February 12, because the gradient was too weak to apply the method of Nash afterwards. Ny-Ålesund was situated outside or at the edge of the vortex in the whole winter, making it somewhat difficult to obtain results. Thus, calculations have only been carried out for the period from January 1, 2001 to January 30, 2001. The observed ozone volume mixing ratio at the 475 K level remained quite constant in this period, see Figure 4.26. Subtracting the gain due to diabatic descent yields chemical loss rates of about 15 ppb/day, as can be seen in Figure 4.27. This is comparable to the loss rates of the previous winter in the same time period. However, due to the short time period, the cumulative loss is not large. The volume mixing ratio of January 1, 2001 reduced by the cumulative chemical loss is shown in Figure refpic.cumloss2001 for the 475 K level. The cumulative loss adds up to 0.4 ± 0.3 ppm (12%), which is barely significant.

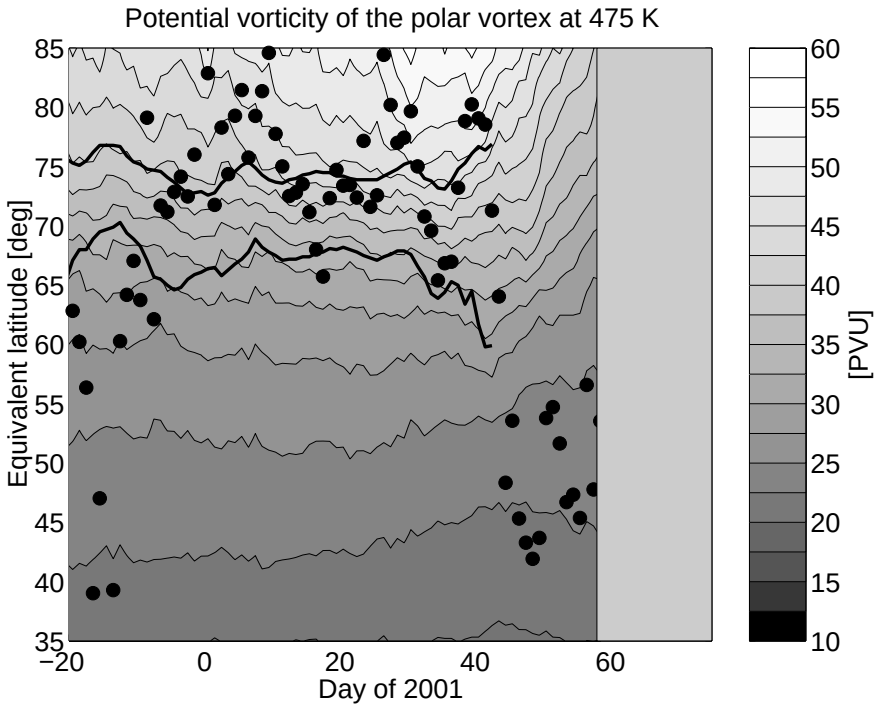

Figure 4.25: Vortex evolution in 2000/2001 at the 475 K level. Contours represent the potential vorticity at a given equivalent latitude and date. The black dots mark the position of Ny-Ålesund in terms of equivalent latitude and the thick lines denote the inner and the outer edge of the vortex.

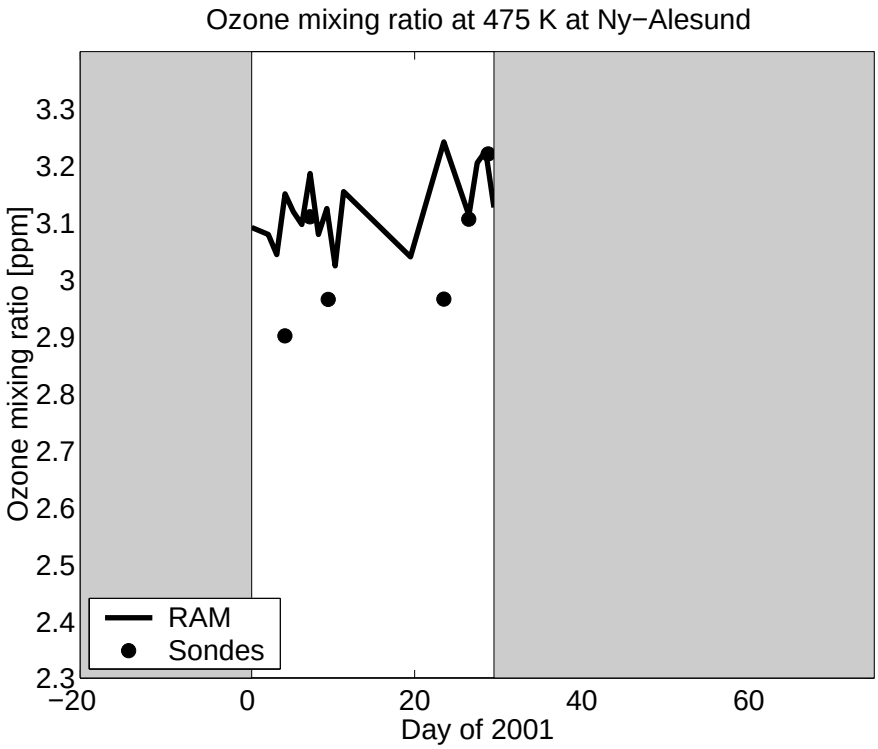

Figure 4.26: Ozone mixing ratio at the 475 K isentropic level in the winter 2000/2001. Measurements of the ozone radiometer (diurnal means, thick line) and of sondes (dots) at Ny-Ålesund.

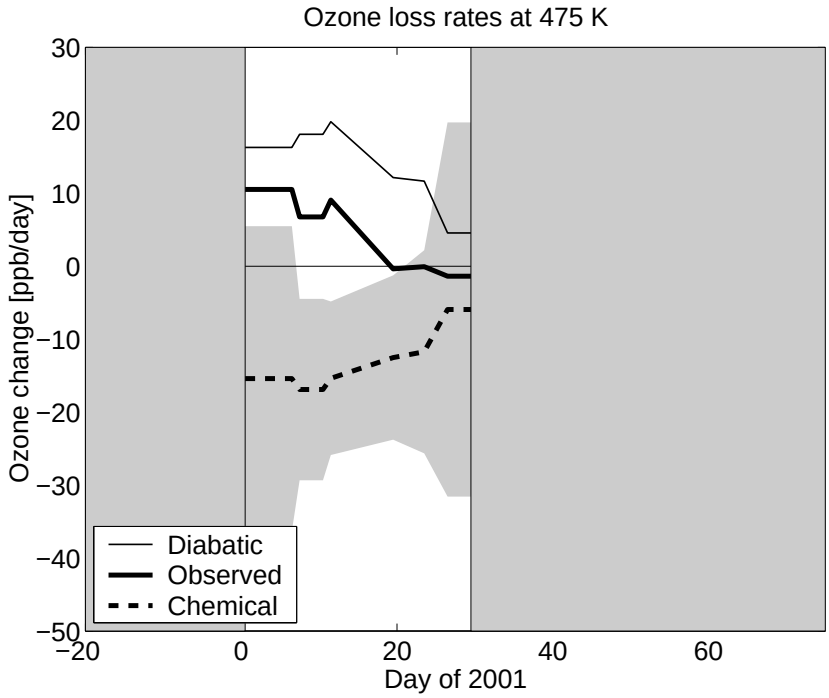

Figure 4.27: Ozone loss per day at the 475 K isentropic level in 2000/2001. The thick line shows the ozone change per day observed by the radiometer, the thin line shows the change due to diabatic descent inferred from the passive profile, the dashed line shows the chemical change (with error bars), given by the difference of the above changes. All changes are 25 day means. The passive profile has been corrected for natural ozone production.

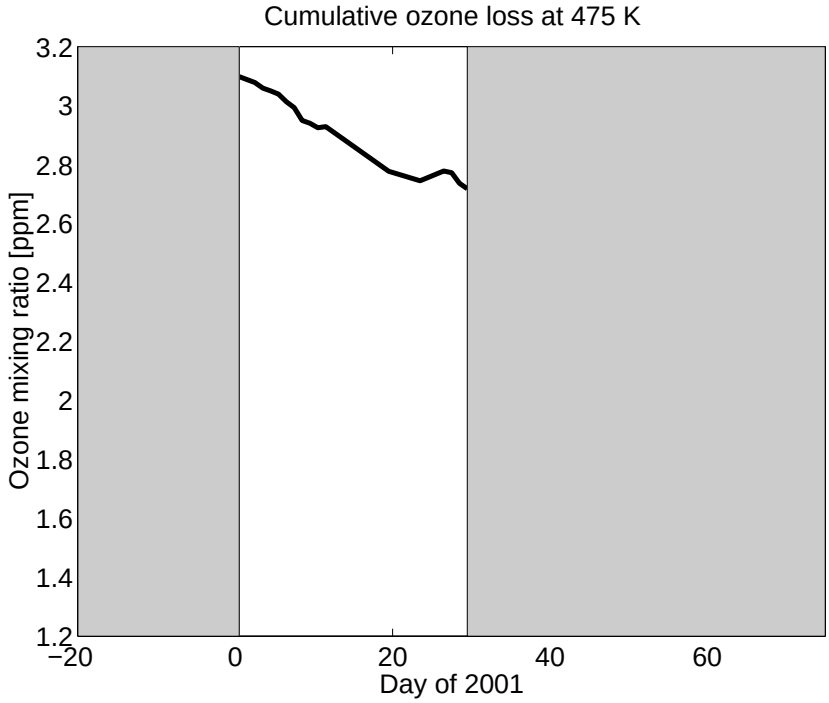

Figure 4.28: Cumulative loss at the 475 K isentropic level in 2000/2001. Shown is the volume mixing ratio of January 1, 2001 reduced by the cumulative loss obtained by the ozone radiometer. The passive profile used for the cumulative loss calculations has been corrected for natural ozone production.

4.A Integration of Loss Rates

It is shown here why Equation 4.1 cannot simply be integrated. We will call the observed profile **x**, the passive profile **p** and the chemical loss or gain profile **c** with $\mathbf{c} = \mathbf{x} - \mathbf{p}$ (loss has a negative sign and gain has a positive sign). These profiles shall be the high resolution profiles. In the passive tracer method, the low resolution passive profile $\hat{\mathbf{p}}$ and the low resolution observed profile $\hat{\mathbf{x}}$ are subtracted:

$$\begin{aligned}\hat{\mathbf{c}} &= \hat{\mathbf{x}} - \hat{\mathbf{p}} \\ &= \mathbf{A}\mathbf{x} + (\mathbf{1} - \mathbf{A})\mathbf{x_0} - [\mathbf{A}\mathbf{p} + (\mathbf{1} - \mathbf{A})\mathbf{x_0}] \\ &= \mathbf{A}\mathbf{c}\end{aligned} \tag{4.6}$$

Thus, the low resolution chemical loss is just the high resolution loss convoluted with the averaging kernels matrix, which is very illustrative. From $\mathbf{c} = \mathbf{0}$ follows $\hat{\mathbf{c}} = \mathbf{0}$, as it should be.

One may argue that it makes a difference whether a high resolution passive profile is subsided and convoluted to the altitude resolution as the last step or if a low resolution profile obtained from the high resolution profile is subsided and convoluted a second time to realign it with the altitude resolution. The first case is assumed in the above formula, while the second case is the method actually used, because the RAM passive profile is in low resolution from the beginning. However, tests with sonde profiles in high resolution and convoluted to our altitude resolution have shown that the resulting passive profiles agree very well in both cases. Differences were below 0.05 ppm throughout.

Simply integrating Equation 4.1 leads to erroneous results. The loss rates have to be integrated between t_0 and t to obtain the chemical loss $\hat{\mathbf{c}}$ here, where t_0 may be a date in December and t may be a date in March in our case:

$$\begin{aligned}\hat{\mathbf{c}} &= \hat{\mathbf{x}}(t) - \hat{\mathbf{x}}(t_0) - \int_{t_0}^{t} \frac{\partial \hat{\mathbf{x}}(t')}{\partial \Theta} \hat{Q}(t')\,\mathrm{d}t' \\ &= \mathbf{A}(\mathbf{x}(t) - \mathbf{x}(t_0)) \\ &\quad - \int_{t_0}^{t} \frac{\partial}{\partial \Theta}[\mathbf{A}\mathbf{x}(t') + (\mathbf{1} - \mathbf{A})\mathbf{x_0}]\hat{Q}(t')\,\mathrm{d}t' \\ &= \mathbf{A}(\mathbf{c}(t) + \mathbf{p}(t) - \mathbf{p}(t_0)) \\ &\quad - \int_{t_0}^{t} \frac{\partial}{\partial \Theta}[\mathbf{A}\mathbf{x}(t') + (\mathbf{1} - \mathbf{A})\mathbf{x_0}]\hat{Q}(t')\,\mathrm{d}t'\end{aligned} \tag{4.7}$$

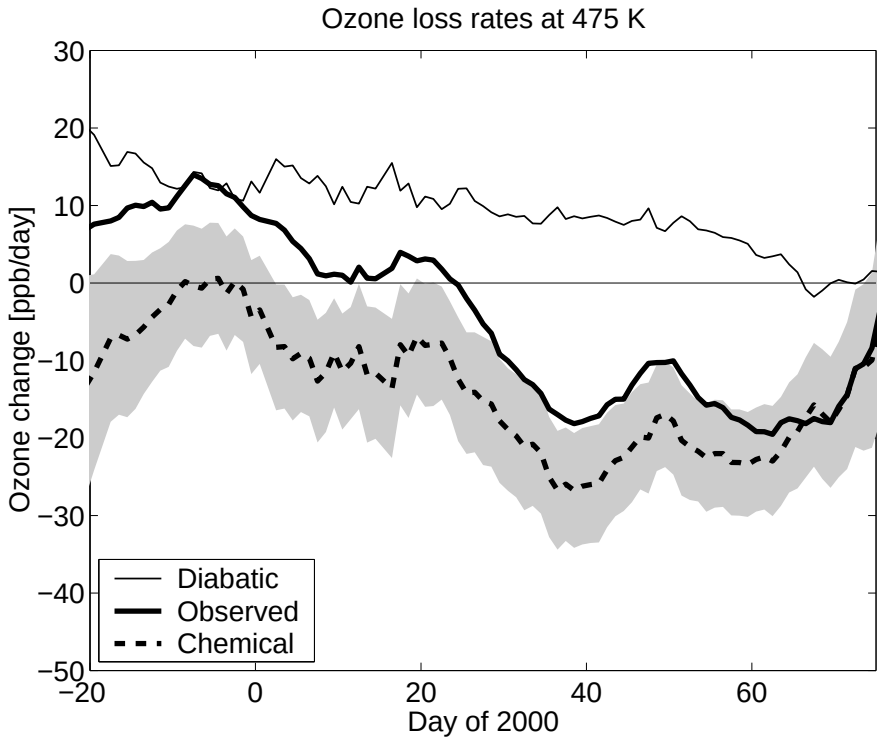

Figure 4.29: Ozone loss per day at the 475 K isentropic level inferred from Equation 4.1. Compare to Figure 4.6.

$\hat{Q}$ is the heating rate in potential temperatures and Θ is the potential temperature itself. With

$$\mathbf{p}(t) - \mathbf{p}(t_0) = \int_{t_0}^{t} \frac{\partial \mathbf{x}(t')}{\partial \Theta} \hat{Q}(t')\,\mathrm{d}t' \tag{4.8}$$

we obtain:

$$\begin{aligned} \hat{\mathbf{c}} &= \mathbf{A}\mathbf{c}(t) + \mathbf{A}\int_{t_0}^{t} \frac{\partial \mathbf{x}(t')}{\partial \Theta} \hat{Q}(t')\,\mathrm{d}t' \\ &\quad - \int_{t_0}^{t} \frac{\partial}{\partial \Theta}[\mathbf{A}\mathbf{x}(t') + (\mathbf{1}-\mathbf{A})\mathbf{x_0}]\hat{Q}(t')\,\mathrm{d}t' \end{aligned} \tag{4.9}$$

Compared to Equation 4.6, an unpleasant extra term occurs. This term is due to the fact that it makes a difference if the gradient of the profile is calculated first and

convoluted next or if the profile is convoluted first and the gradient is computed from the convoluted profile. In addition to that, $\mathbf{c} = \mathbf{0}$ does not imply $\hat{\mathbf{c}} = \mathbf{0}$, which is very annoying.

4.B Double Convolution

The low resolution passive profile of the RAM has to be convoluted for a second time after subsiding it in order to realign it with the altitude resolution. This is equivalent to the substitution of $\mathbf{A}$ by $\mathbf{A^2}$. If the result of the optimal estimation is called $\hat{\mathbf{x}}_\mathbf{1} = \mathbf{Ax} + (\mathbf{1} - \mathbf{A})\mathbf{x_0}$, the convolution yields

$$\begin{aligned}\hat{\mathbf{x}}_\mathbf{2} &= \mathbf{A}\hat{\mathbf{x}}_\mathbf{1} + (\mathbf{1} - \mathbf{A})\mathbf{x_0} \\ &= \mathbf{A}(\mathbf{Ax} + (\mathbf{1} - \mathbf{A})\mathbf{x_0}) + (\mathbf{1} - \mathbf{A})\mathbf{x_0} \\ &= \mathbf{A^2x} + (\mathbf{1} - \mathbf{A^2})\mathbf{x_0} \end{aligned} \tag{4.10}$$

Since the altitude resolution of $\mathbf{A^2}$ is similar to the altitude resolution of $\mathbf{A}$ (not shown here), this is only a little drawback.

4.C Error Analysis

The error of a single ozone profile is estimated by direct comparison with ozone sondes. The systematic error is calculated as the difference between the mean of the RAM profiles and the mean of the convoluted sonde profiles. Analogical, the statistical error is given by the standard deviation of the difference between the RAM profiles and the convoluted sonde profiles. The systematic error at the 475 K isentropic level is -0.05 ppm (less than 2%) and the statistical error is 0.14 ppm (less than 5%) for the 46 sondes launched in the time frame of the depletion calculations. This is well inside the error bars of the sondes itself [Komhyr et al., 1995].

The error of the cumulative loss is given by five different error sources. The statistical errors of the ozone profile itself and the passive profile have to be considered as well as the respective systematic errors. In addition to that, the error of the heating rates has to be taken into account. The statistical error of the chemical loss profile is given by

$$\sigma_c^2 = \sigma_x^2 + \sigma_p^2 \tag{4.11}$$

where σ_x^2 and σ_p^2 are the errors of the ozone profile and the passive profile. The error of the ozone profile, which is averaged over 5 days, is calculated from the errors of the single profiles at the 475 K level. Since the ozone measurements

are correlated with each other, we will have to use a slightly unusual approach to calculate the errors. The average can be written as

$$\bar{\mathbf{y}} = \mathbf{G}\mathbf{y} = (1/N \cdots 1/N) \begin{pmatrix} y_1 \\ y_2 \\ \vdots \\ y_N \end{pmatrix} \tag{4.12}$$

where the $y_1, \ldots, y_N$ are the N mixing ratio measurements. The corresponding covariance matrix (in this case only a number) is given by

$$\mathbf{S}_{\bar{\mathbf{y}}} = \mathbf{G}\mathbf{S}_{\mathbf{y}}\mathbf{G}^{\mathbf{T}} \tag{4.13}$$

$\mathbf{S}_{\mathbf{y}}$ is the covariance matrix of the single measurements. While the diagonal is just the measurement error of $\sigma = 0.14$ ppm, the correlation between the measurements in the off-diagnoal elements has to be considered as well. It is assumed that the covariances are given by

$$S_{y,ij} = \sigma^2 \exp(-|t_i - t_j|/\tau) \tag{4.14}$$

where $|t_i - t_j|$ is the time gap between measurements i and j and τ is a constant called correlation length. While measurements that follow shortly after each other should give almost the same result, because the ozone mixing ratio does not change so fast, measurements that are separated by a big time gap should show no correlation. The correlation length gives the point where the correlation breaks down. It can be estimated from the time series and is set to 0.5 days for this analysis. The error computed with this method is larger than the error calculated by division by $\sqrt{N}$. The reason is an effective reduction of the number of measurements due to the correlation between them.

We will now treat the remaining errors. The error of the passive profile is the error of the initial profile, subsided and convoluted to realign it with the altitude resolution. The systematic error is given by

$$\Delta c = \Delta x - \Delta p \tag{4.15}$$

where Δx and Δp are the systematic errors of the ozone profile and the passive profile. Errors are counted positive if the measured microwave profile is greater than the true profile (from sondes). Since c is negative in case of ozone depletion, the measured depletion gets smaller when we have a positive systematic error in the ozone profile, and the true depletion is greater.

The error in the heating rates is accounted for by subsiding the passive profile with heating rates Q changed by ± 0.1 K and computing the difference to the

passive profile actually used. The error is -0.32 ppm for the lower heating rates and 0.35 ppm for the higher heating rates. Here, lower heating rates mean more cooling, since the net heating rate is negative. Thus, the passive profile subsides faster than the original passive profile and the mixing ratio of the passive profile at 475 K increases. Hence, the measured c is rendered more negative than the true loss profile, and the measured depletion increases in comparison to the true depletion. Thus, the error in c is negative for lower heating rates.

The actual results for the different errors for the winter 1999/2000 are given now. The statistical error adds up to 0.05 ppm, while the systematic error is only -0.02 ppm. The absolute value of the error originating from the heating rates is 0.3 ppm for the decreased heating rates as well as for the increased heating rates. Thus, errors are clearly dominated by the error in the heating rates.

The calculation of the errors of the loss rates is quite simple. It is just the error of the both cumulative losses used to infer the loss rate divided by the number of days between them. Typical values lie about 10 ppb/day.

4.D Convolution of Independent Measurements

The several measurements and model results require different treatment if we want to convolute them to our altitude resolution. The results of Match, Mark IV and HALOE/OMS were available as a loss profile. Thus, they have been convoluted according to Equation 4.6:

$$\hat{\mathbf{c}} = \mathbf{A}\mathbf{c} \tag{4.16}$$

The altitude grid of the high resolution profiles is interpolated to the retrieval grid in order to perform the convolution. Since the loss profiles were only available on a restricted altitude range, missing values were assumed to be zero.

The results of SLIMCAT consist of a passive profile and an ozone profile. They have been convoluted first and subtracted afterwards, again to match Equation 4.6. Additionally, the profiles have been averaged over 5 days after the convolution. The results of GOME, MIRA and ASUR need not to be convoluted, because they have a similar altitude resolution.

If we want to compare independent chlorine monoxide measurements to our observations, they have to be convoluted to the altitude resolution of the RAM and day and night differences have to be used. However, it is not obvious in which order we have to perform these actions. The spectra of the RAM are subtracted before the retrieval. If we assume that the weighting functions do not change between the day and night measurements, we can take advantage of the fact that the forward model is almost linear:

$$\mathbf{K}(\mathbf{x}_{\text{day}} - \mathbf{x}_{\text{night}}) = \mathbf{y}_{\text{day}} - \mathbf{y}_{\text{night}} \tag{4.17}$$

Thus, the result of the optimal estimation method is an estimator for the difference between the day time profile and the night time profile:

$$\hat{\mathbf{x}} = \mathbf{A}(\mathbf{x}_{\text{day}} - \mathbf{x}_{\text{night}}) + (\mathbf{I} - \mathbf{A})\mathbf{x_0} \tag{4.18}$$

Hence, we have to subtract the profiles first and to convolute them next.

The convolution of the denitrification profiles is more problematic. Since the averaging kernels and the a priori profile belong to ozone or chlorine monoxide measurements, their usage in the convolution is not obvious. But if we want to get an idea of the denitrification in our altitude resolution, the only possibility is to calculate **An**, where **n** is the difference profile of the denitrification and **A** are the averaging kernels of the ozone or chlorine monoxide retrieval.

5 Water Vapor Columns

5.1 Overview

It is not only possible to derive ozone profiles from the measurements of the ozone radiometer, but also to obtain water vapor columns. In case of an atmosphere free of liquid water, there is an unique relationship between the bias of the spectrum and the water vapor column. Unfortunately, moist atmospheric conditions spoil this relationship. Additional measures have to be performed to correct the columns in this case. The water vapor column is given by the integral of the number density n_{H_2O} of water vapor above a certain point of the surface of the earth:

$$C_{H_2O} = \int_0^z n_{H_2O}(z')\,dz' \tag{5.1}$$

A common measure for the water vapor column is the precipitable water vapor. This is the height of precipitation that would be caused by all the water vapor in the column. It can be deduced from the column by

$$\frac{C_{H_2O}}{n_{liquid}} \quad \text{with} \quad n_{liquid} = \frac{\rho N_A}{m_{mol}} \tag{5.2}$$

where n_{liquid} is the number density of liquid water, ρ is the mass density of liquid water, m_{mol} is the molecular weight and N_A is Avogadro's constant.

5.2 Theory

In Figure 5.1 water vapor columns from sonde measurements are plotted versus bias measurements of the ozone radiometer performed at the same date. The relationship between water vapor columns and bias is exponential for fair weather conditions. This relationship can be derived from the radiative transfer equation under the following assumptions:

- The absorption cross section of water vapor $\alpha^*_{H_2O}$ is a constant.
- The temperature of the troposphere $T_{B,trop}$ is a constant.
- Liquid water is absent.
- No scattering occurs.

The absorption coefficient of the atmosphere is mainly composed of the absorption coefficients of oxygen and water vapor in the considered frequency range, $\alpha \approx \alpha^*_{H_2O} n_{H_2O} + \alpha^*_{O_2} n_{O_2}$. In combination with the radiative transfer equation, the result for the bias is

$$\begin{aligned} T_B &= \int_0^z \alpha(z') T_{B,trop}(z') \exp\left(- \int_0^{z'} \alpha(z'') \, dz'' \right) dz' \\ &= T_{B,trop} \left[1 - \exp(-\alpha^*_{H_2O} C_{H_2O} - K) \right] \end{aligned} \tag{5.3}$$

where K is the constant contribution of oxygen. The offset by oxygen is about 25 K at 142 GHz, as can be seen in Figure 5.1. If self absorption is negligible, the relationship is rendered linear

$$T_B = T_{B,trop}(\alpha^*_{H_2O} C_{H_2O} + K) \tag{5.4}$$

since $\exp(x) \approx 1 + x$ for $x \ll 1$.

5.3 Method

In order to obtain water vapor columns from the microwave measurements, a formula is conceived that yields the columns as a function of the bias of the spectra. Equation 5.3 is the key to the problem. We can obtain the three unknown coefficients, namely $T_{B,trop}$, $\alpha^*_{H_2O}$ and K, by fitting a curve through the measurement pairs of sonde water vapor columns and microwave bias temperatures. We introduce the opacity τ of the troposphere now to simplify the fit, given by

$$\tau = \ln\left(\frac{T_{B,trop}}{T_{B,trop} - T_B} \right) \tag{5.5}$$

Since the relationship between τ and C_{H_2O} is linear

$$\tau = \alpha^*_{H_2O} C_{H_2O} + K \tag{5.6}$$

we can get $\alpha^*_{H_2O}$ and K by a linear fit. $T_{B,trop}$ is more difficult to gain, since it is given by the bias we would see if the atmosphere would be totally opaque. Since

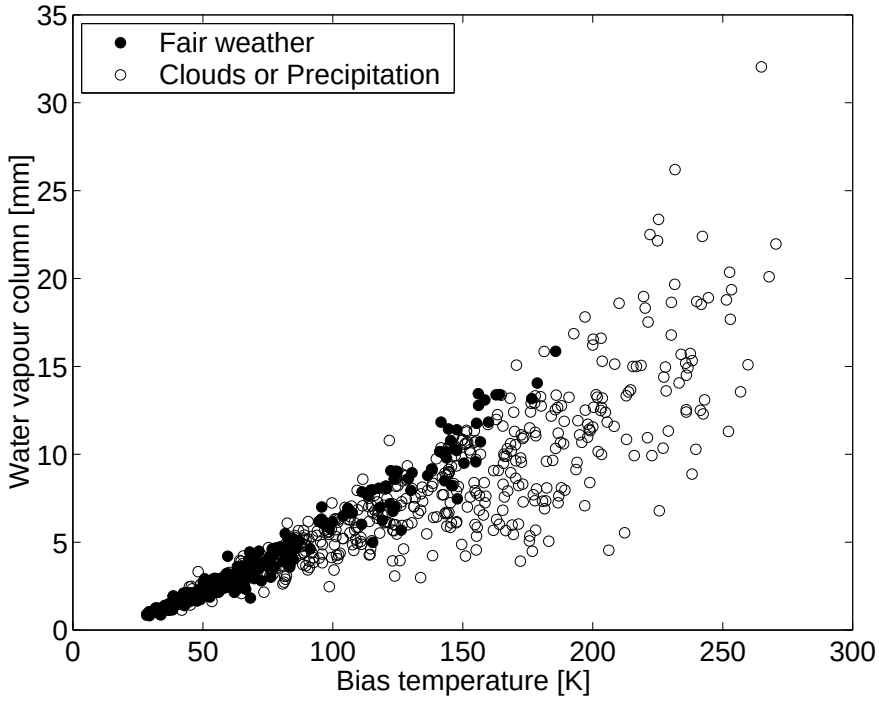

Figure 5.1: Water vapor columns from sonde measurements versus bias temperatures of radiometer measurements made at the same date. Black dots mark sonde launches at fair weather conditions, and white dots mark launches at cloudy or rainy conditions.

this is never the case, it can only be estimated. Fortunately, the value of $T_{\mathrm{B,trop}}$ is not very important for the accuracy of the measurements. We will use a value of 300 K for the time being. Solving the relationship of bias and column for the column and introducing the fitted values yields

$$C_{\mathrm{H_2O}} = \frac{\tau - K}{\alpha^*_{\mathrm{H_2O}}} = \frac{\ln(300/(300 - T_{\mathrm{B}})) - 0.0609}{0.0575} \tag{5.7}$$

Only sondes launched under fair weather conditions were used for the fit. We will also have a look at the possible error sources here. The actual errors of the method in comparison to sondes are given later in section 5.5. Statistical error sources for the columns are noise in the measurements, varying tropospheric temperatures and absorption cross sections. Systematic errors are introduced by problems with sonde measurements at very cold temperatures. Above 10 km altitude, the sonde data is considered to be unreliable. Since most of the water vapor resides in the first few kilometers of the atmosphere, this should be a minor error source.

5.4 Correction

Moist weather conditions bearing clouds or precipitation spoil the assumption that no liquid water is present. Liquid water contributes to the atmospheric spectrum by absorption, emission and scattering. Absorption dominates if the wavelength of the radiation is much greater than the radii of the cloud or rain droplets (Rayleigh regime). If the wavelength and the radii are comparable, Mie scattering occurs. Absorption and emission of radiation by droplets lead to systematically higher brightness temperatures compared to the results under the same atmospheric conditions without liquid water. Similar to the water vapor absorption, liquid water absorption can simply be described by an absorption coefficient

$$\alpha = \alpha^*_{H_2O} n_{H_2O} + \alpha^*_{O_2} n_{O_2} + \alpha^*_{liquid} n_{liquid} \tag{5.8}$$

where n_{liquid} is the number density of the liquid water. The effects of scattering are more difficult to infer, but may also have a systematic brightening effect for thin clouds. In the 140 GHz region, both effects play a dominant role. This can clearly be seen in Figure 5.1. Spectra taken under moist conditions show a systematically higher brightness temperature than spectra under fair conditions that were measured at the same water vapor column. Thus, Equation 5.7 overestimates the water vapor column under moist weather conditions.

Weather observations in Ny-Ålesund are not detailed enough to correct the columns. The standard approach to solve this problem is a second measurement at a frequency less influenced by liquid water [Ulaby et al., 1981]. The measurements of the water vapor radiometer at 22 GHz are ideally suited for this correction. Normally, the instrument is operated in reference beam mode. Thus, it is necessary to use the sky dip measurement to obtain the brightness temperature of the spectrum. Unfortunately, this measurement is only performed about once per day. A change to the total power method could solve this problem in the future.

The approach to correct the column measurements uses a system of two linear equations to obtain the two unknown variables water vapor column C_{H_2O} and liquid water column C_{liquid}. A derivation similar to the one of Equation 5.3 yields

$$\begin{aligned} \tau_{22} &= \alpha^*_{H_2O,22} C_{H_2O} + \alpha^*_{liquid,22} C_{liquid} + K_{22} \\ \tau_{142} &= \alpha^*_{H_2O,142} C_{H_2O} + \alpha^*_{liquid,142} C_{liquid} + K_{142} \end{aligned} \tag{5.9}$$

with

$$\tau_{22} = \ln\left(\frac{T_{B,trop,22}}{T_{B,trop,22} - T_{B,22}}\right) \qquad \tau_{142} = \ln\left(\frac{T_{B,trop,142}}{T_{B,trop,142} - T_{B,142}}\right) \tag{5.10}$$

when scattering is assumed to be negligible. The constants $\alpha^*_{H_2O}$, $T_{B,trop}$ and K can be deduced from measurements under fair weather conditions (for clarity we

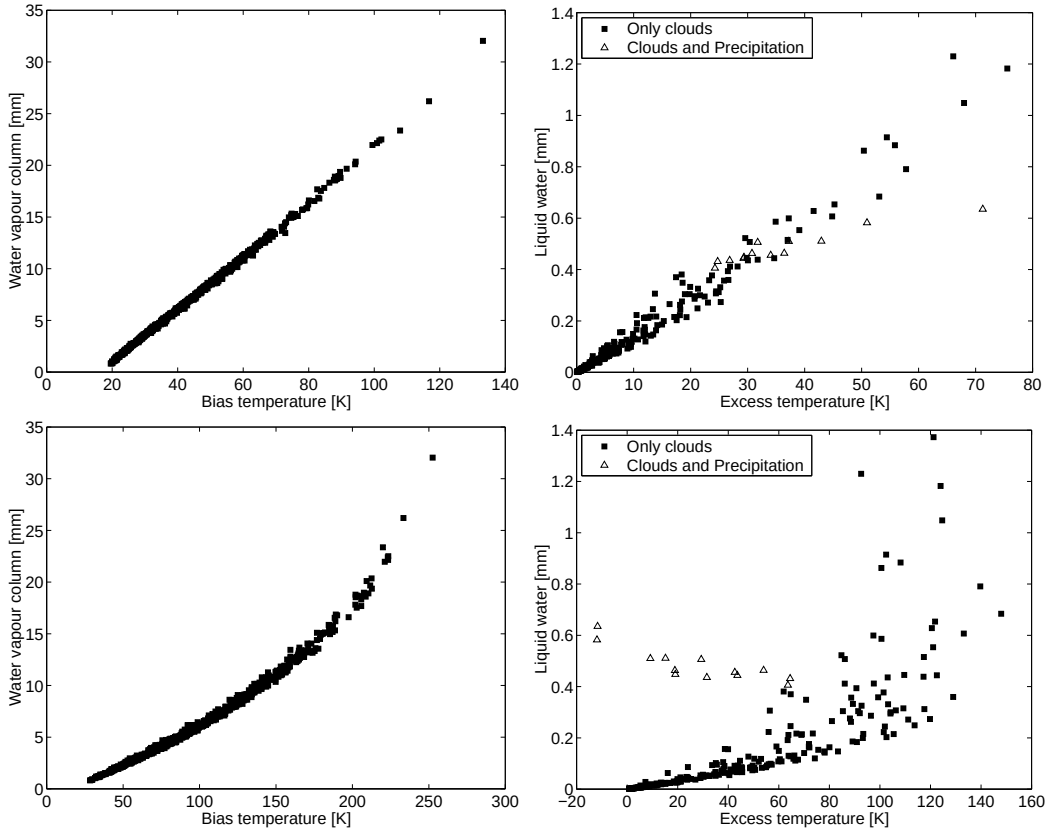

Figure 5.2: Results of the MWMOD forward model. Scatter plots of water vapor columns of sondes or calculated liquid water columns versus the computed brightness temperatures. Upper left: Water vapor columns versus brightness temperatures at 22 GHz. No clouds or precipitation were allowed. Upper right: Liquid water columns versus additional brightness temperatures due to liquid water at 22 GHz. Squares mark cloud generation by the model, triangles mark additional precipitation generation. Lower left: Water vapor columns versus brightness temperatures at 142 GHz. No clouds or precipitation were allowed. Lower right: Liquid water columns versus additional brightness temperatures due to liquid water at 142 GHz. Squares and triangles: see above.

Frequency	$T_{\mathrm{B,trop}}$	$\alpha^*_{\mathrm{H_2O}}$	$\alpha^*_{\mathrm{liquid}}$	K
22 GHz (model)	300	0.0156	0.3005	0.0509
142 GHz (model)	300	0.0570	3.6871	0.0520
142 GHz (measured)	300	0.0575	—	0.0609

Table 5.1: Parameters for water vapor column retrieval

have omitted the index 22 or 142). Since there are no measurements of rain rates or cloud liquid water contents, the constants α^*_{liquid} have to be determined by a radiative transfer model. Once the constants are known the system of equations can be inverted to yield C_{H_2O} and C_{liquid} as a function of the brightness temperatures.

All constants have been obtained by the radiative transfer model MWMOD. MWMOD was developed by the Institut für Meereskunde in Kiel and by the University of Washington. One of the strengths of this model is the proper simulation of hydrometeors, a possibility which is lacking in many other models. Some of the features of the model are the simulation of scattering and absorption at hydrometeors and the surface, automatic cloud generation and many different types of clouds and precipitation to choose from.

Temperature, pressure and humidity profiles of about 800 sondes were used in the model runs. Clouds were generated automatically by the model by a simulation of the adiabatic rise of the air parcels. Condensation occurred when the humidity exceeded 92.5%. Ice and water clouds were allowed to form, and precipitation included rain, snow and hail. The cloud drop size distributions were taken from Deirmendjian [1969] and Ulaby et al. [1981], while the rain drop size distribution was taken from Marshall and Palmer [1948]. Results are shown in Figure 5.2 and the retrieved parameters can be found in Table 5.1. The parameters inferred from the microwave measurements and sondes, which were used in Equation 5.7, are also shown. The values of $\alpha^*_{H_2O}$ and K are taken from a fit of the calculated τ to the water columns of sondes started under fair weather conditions, while the α^*_{liquid} are derived from a fit of $\tau - \alpha^*_{H_2O} C_{H_2O} - K$ to the calculated liquid water content of the model. Only model results without precipitation have been used for the second fit. The parameterization for liquid water is only valid up to columns of 0.15 mm, including about 85% of the simulated clouds. Finally, the inversion of Equation 5.9 leads to

$$\begin{pmatrix} C_{H_2O} \\ C_{\text{liquid}} \end{pmatrix} = \begin{pmatrix} 91.1612 & -7.4300 \\ -1.4087 & 0.3860 \end{pmatrix} \begin{pmatrix} \tau_{22} - K_{22} \\ \tau_{142} - K_{142} \end{pmatrix} \tag{5.11}$$

The zenith angle of the measurements has been set to 70° for both frequencies. Although the ozone radiometer is usually measuring under this angle, only two days of measurements exist for the water vapor radiometer here.

Older measurements can be corrected by a makeshift. We take advantage of the fact that measurements under moist conditions often show a column exceeding the highest column physically possible. The highest physical column is a column showing 100% relative humidity at every altitude, which can easily be calculated from the temperature profile and the saturation pressure. Columns showing more than this maximum column $C_{\max}$ are corrected by

$$C_{\text{corr}} = C_{H_2O} + 0.0073\Delta C^2 - 1.07\Delta C - 2.7384 \tag{5.12}$$

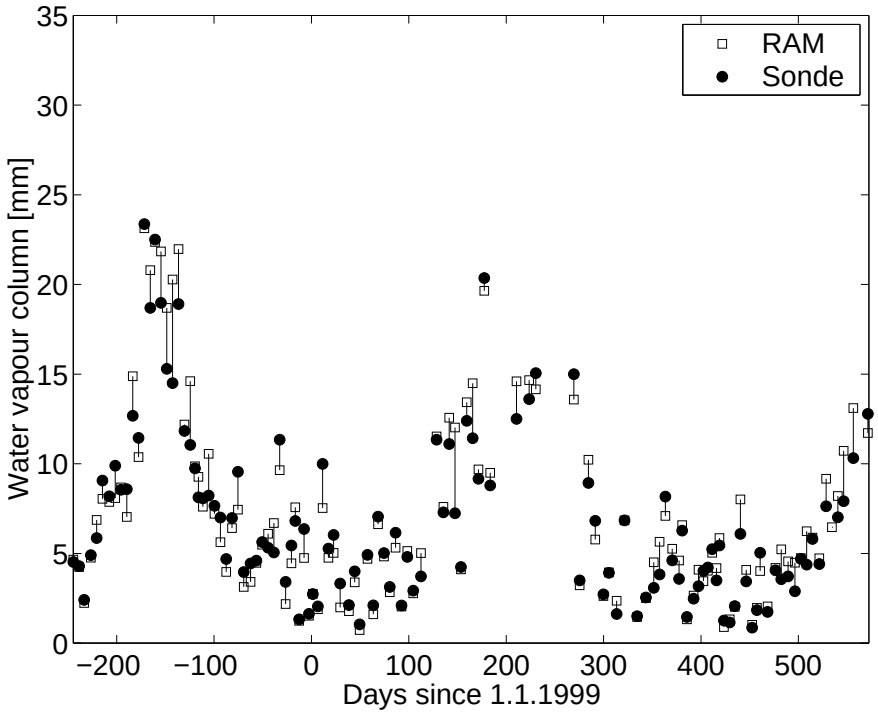

Figure 5.3: Water vapor columns versus date. White squares mark results obtained from the bias temperatures of the ozone radiometer. Black dots are corresponding sonde measurements. The difference is marked by a line. RAM measurements have been corrected for liquid water by the makeshift method (see text). For clarity, only a selection of sonde matches is shown.

where $\Delta C = C_{H_2O} - C_{max}$ is the difference column in millimeters. The formula is due to the fact that there is an empirical correlation between the error in the column and the excess of the column $C_{H_2O} - C_{max}$. Columns under fair weather conditions are automatically ignored by the method, because they never show more than 100% humidity.

5.5 Results

The results of the water vapor column measurements are shown in Figure 5.3. The white squares show the water vapor columns that were deduced from radiometer measurements, while the black dots show sonde measurements carried out at the same date. The agreement is excellent for fair weather conditions, but in some individual cases the columns differ by more than 5 mm. Statistical errors are 0.57 mm under fair conditions and 1.69 mm under moist conditions. Columns un-

der moist conditions show a systematic offset of 0.78 mm to the sondes due to the fact that some columns lie below C_{max} although they are disturbed by liquid water. The annual cycle of the water vapor content of the troposphere can be observed nicely in the plot. Typical columns lie between 5 mm and 25 mm precipitable water vapor. Compared to mid latitude values this shows the very arid conditions in the Arctic.

Conclusions

This work presented measurements of the ground based microwave Radiometer for Atmospheric Measurements (RAM), operated at the Arctic station of the Network for the Detection of Stratospheric Change (NDSC) at Ny-Ålesund, Spitsbergen (79° N, 12° E).

Chapter 3 gave a summary of the status of the retrieval software and described recent additions and changes. An introduction to the optimal estimation method was followed by a presentation of the forward models for the water vapor, ozone and chlorine monoxide radiometers. Retrieval parameters like a priori profiles and covariance matrices were described additionally. Forward model features like the treatment of the tropospheric emission, standing waves or higher side bands were discussed in detail. A new method was introduced to treat spectra measured under moist weather conditions. The new algorithm guarantees a constant signal-to-noise-ratio for all spectra and thus a constant altitude resolution.

A special focus was laid on the water vapor retrieval, which proved to be a challenging task. While it was not possible to retrieve any reliable profile information from the full spectra yet, a simple retrieval model using only the innermost 200 channels looked promising. A preliminary profile could be obtained for June 24, 2001, showing basic agreement with similar measurements. Features of the model for the full spectra include logarithmic mixing ratios, a sophisticated parameterization of the tropospheric mixing ratios and a calculation of frequency shift, self broadening and continua. Logarithmic mixing ratios led to a strong nonlinearity in the model, which resulted in convergence problems and difficulties in determining errors and a priori values. Inclusion of frequency shift, self broadening and continua considerably complicated the forward model and the calculation of the weighting functions, which were derivated analytically. In the moment, it is doubtful if the retrieval of the full spectra will eventually lead to meaningful results. Considering the results of the simplified model, it may even not be necessary to retrieve the full spectra.

Chapter 4 provided detailed insight into the chemistry and dynamics of ozone depletion in the Arctic and their current understanding. While the focus was clearly on the ozone and chlorine monoxide measurements of the RAM, the gen-

eral evolution of the winter 1999/2000 was shown in some detail by a look on other measurements and models.

A method for the determination of ozone loss rates from the measurements of the ozone radiometer was presented. A modification of this method using a passive profile was introduced, leading to more accurate results. A cumulative ozone loss of 1.2 ± 0.4 ppm for the winter 1999/2000 and of 0.5 ± 0.3 ppm for the winter 2000/2001 was derived. Loss rates reached values of 10 ppb/day in December and January and 25 ppb/day in March. Several explanations for the rather high loss rates in December were proposed, including mixing of mid latitude air, an overestimation of cooling rates or unknown chemistry. This emphasizes the importance of correct heating rates and the effects of mixing for the accuracy of the loss rates. An examination of the accuracy of the heating rates (including a comparison to tracer measurements, a PV analysis and a sensitivity analysis) resulted in an estimated accuracy of 0.1 K/day. This contributed an error of about 0.3 ppm to the cumulative loss, rendering the heating rates to the main error source. A comparison to different techniques for the determination of ozone loss (including Match, tracer methods and vortex average methods) resulted in good agreement between the results when adjusted to our altitude resolution. Remaining differences could easily be explained by differences in the methods and inherent errors, considered time periods and observed altitude levels. Comparison to the SLIMCAT model also resulted in very good agreement.

Measurements of ClO, $ClONO_2$, HCl, HNO_3 and denitrification were presented to develop a chemical scenario for the 1999/2000 winter. All of these measurements were additionally compared to SLIMCAT results. Obvious discrepancies between modeled and observed mixing ratios of ClO and HCl could be assigned to uncertainties in the understanding and modeling of denitrification and polar stratospheric cloud formation. However, it could be shown that the basic processes leading to ozone loss seem to be well understood qualitatively. Quantitative comparisons are still problematic due to large error bars in measurements and methods of ozone loss determination as well as uncertainties in the models. The negligible effect of the discrepancies in ClO on the cumulative ozone loss could be attributed to the short period of the additional ozone depletion induced by denitrification.

In Chapter 5, it was demonstrated that measurements of the RAM can be used to deduce water vapor columns and liquid water contents of the troposphere. This is a nice auxiliary data product considering that the RAM was not explicitly built to measure these quantities. While water vapor columns could be obtained with an accuracy of 0.57 mm under fair weather conditions with the current configuration, liquid water columns and accurate water vapor columns under moist weather conditions are only measurable in principle. The effects of precipitation and clouds on the accuracy of the measurements were evaluated with a radiative transfer model

and a possible method for deducing liquid water columns was shown. A makeshift method for the correction of water vapor columns under moist conditions was presented. Errors for moist conditions were about 1.69 mm.

Finally, we will have a short look into the future. There are still opportunities in the RAM data which remain unused yet. The behavior of ozone mixing ratios in summer and fall and chemistry in the upper stratosphere between 30–50 km are some examples which come to mind here. It also remains to be hoped that the RAM will continue operations for a long time, since every day of data increases the opportunity to research long term trends based on a consistent data set. Last but not least, the new instruments in Greenland and Venezuela will add a whole new dimension to the data set of the microwave instruments, for example by the first continuous measurements of the tracer N_2O in the Arctic.

Acknowledgments

I would like to thank everyone who has made this work possible. Special thanks go to:

- Prof. Klaus Künzi for being the supervisor of my thesis
- Prof. John Burrows as the second advisor of the thesis
- The many members of the RAM group I met since 1996, when I began my work here as a student help: Bernd Barry, Nicole Buschmann, Michael Hoock, Kai Lindner, Ulf Klein, Jens Langer, Uwe Raffalski, Björn-Martin Sinnhuber and Rudolf Tuckermann
- Holger Bremer, Armin Kleinböhl and Miriam von König of the ASUR group for providing the ASUR data, scientific help and discussions, especially about denitrification and water vapor retrieval
- Nicole and Miriam for proof-reading
- Stefan Bühler and his group for many useful hints for the water vapor retrieval and the forward model ARTS
- Martyn P. Chipperfield and Björn-Martin Sinnhuber, University of Leeds, for kindly providing the SLIMCAT calculations
- Keith Shine, University of Reading, for the radiative transfer routines for the ozone depletion calculations
- Markus Rex, Alfred Wegener Institute, for providing the MATCH data
- Rolf Müller, Forschungszentrum Jülich, for providing the HALOE and OMS data
- Kai-Uwe Eichmann, University of Bremen, for providing the GOME data
- Gerhard Kopp, Forschungszentrum Karlsruhe, for providing the MIRA data

- Geoffrey C. Toon, Jet Propulsion Laboratory, for providing the Mark IV measurements
- ECMWF and NCEP for providing the meteorological data and the sonde teams for the ozone sonde data
- Everyone at Ny-Ålesund for maintaining our instruments

Bibliography

Bates, D. and Nicolet, M.: The photochemistry of atmospheric water vapor. *J. Geophys. Res.*, **55**, 301–327, 1950.

Becker, G., Müller, R., McKenna, D. S., Rex, M. and Carslaw, K. S.: Ozone loss rates in the Arctic stratosphere in the winter 1991/92: Model calculations compared with Match results. *Geophys. Res. Lett.*, **25**, 23, 4325–4328, 1998.

Bevilacqua, R. M., Fromm, M. D., Alfred, J. M., Hornstein, J. S., Nedoluha, G. E., Hoppel, K. W., Lumpe, J. D., Randall, C. E., Shettle, E. P., Browell, E. V., Butler, C., Dörnbrack, A. and Strawa, A. W.: Observations and analysis of PSCs detected by POAM III during the 1999/2000 Northern hemisphere winter. *J. Geophys. Res.*, **107**, accepted, 2002.

Brasseur, G. and Solomon, S.: *Aeronomy of the Middle Atmosphere*. Second edition, D. Reidel Publishing Company, Dordrecht, 1986.

Bremer, H., von König, M., Kleinböhl, A., Küllmann, H., Künzi, K. F., Bramstedt, K., Burrows, J. P., Eichmann, K.-U. and Weber, M.: Ozone depletion observed by ASUR during the Arctic winter 1999/2000. *J. Geophys. Res.*, **107**, accepted, 2002.

Bühler, S., Eriksson, P., Haas, W., Koulev, N., Kuhn, T. and Lemke, O.: *ARTS User Guide*. Available at `www.sat.uni-bremen.de`, 2002.

Chapman, S.: A theory of upper-atmospheric ozone. *Mem. Roy. Meteorol. Soc.*, **3**, 103–125, 1930.

Chipperfield, M. P.: Multiannual simulations with a three-dimensional chemical transport model. *J. Geophys. Res.*, **104**, D1, 1781–1806, 1999.

Crutzen, P. J.: The influence of nitrogene oxide on the atmospheric ozone content. *Quart. J. Roy. Met. Soc.*, **96**, 320–325, 1970.

Crutzen, P. J. and Arnold, F.: Nitric-acid cloud formation in the cold antarctic stratosphere – A major cause for the springtime ozone hole. *Nature*, **324**, 651–655, 1986.

Cruz-Pol, S. L., Ruf, C. S. and Keihm, S. J.: Improved 20–32 GHz atmospheric absorption model. *Radio Sci.*, **33**, 1319–1333, 1998.

Davies, S., Chipperfield, M. P., Carslaw, K. S., Sinnhuber, B.-M., Anderson, J. G., Stimpfle, R. M., Wilmouth, D. M., Fahey, D. W., Popp, P. J., Richard, E. C., von der Gathen, P., Jost, H. and Webster, C. R.: Modeling the effect of denitrification on Arctic ozone depletion during winter 1999/2000. *J. Geophys. Res.*, **107**, accepted, 2002.

Deirmendjian, D.: *Electromagnetic Scattering on Spherical Polydispersions*. American Elsevier Publishing Co., Inc., New York, 1969.

Deniel, C., Bevilacqua, R. M., Pommereau, J. P. and Lefèvre, F.: Arctic chemical ozone depletion during the 1994–1995 winter deduced from POAM II satellite observations and the REPROBUS three-dimensional model. *J. Geophys. Res.*, **103**, D15, 19 231–19 244, 1998.

Drayson, S. R.: Rapid computation of the Voigt profile. *J. Quant. Spec. Rad. Trans.*, **16**, 611–614, 1976.

Drdla, K., Schoeberl, M. R. and Browell, E. V.: Microphysical modelling of the 1999–2000 Arctic winter: Polar stratospheric clouds, denitrification and dehydration. *J. Geophys. Res.*, **107**, accepted, 2002.

Eichmann, K.-U.: Ozone depletion in the northern hemisphere winter/spring period 2000 as measured by GOME. *J. Geophys. Res.*, **107**, in review, 2002.

Eichmann, K.-U., Bramstedt, K., Weber, M., Rozanov, V. V., Hoogen, R. and Burrows, J. P.: O_3 profiles from GOME satellite data – II: Observations in the Arctic spring 1997 and 1998. *Phys. Chem. Earth*, **24**, 453–457, 1999.

Fahey, D. W., Gao, R. S., Carslaw, K. S., Kettleborough, J., Popp, P. J., Northway, M. J., Holecek, J. C., Ciciora, S. C., McLaughlin, R. J., Baumgardner, D. G., Gandrud, B., Wennberg, P. O., Dhaniyala, S., McKinney, K., Peter, T., Salawitch, R. J., Bui, T. P., Elkins, J. W., Webster, C. R., Atlas, E. L., Jost, H., Wilson, J. C., Herman, R. L. and Kleinböhl, A.: The detection of large HNO_3-containing particles in the winter Arctic stratosphere. *Science*, **291**, 1026–1031, 2001.

Farman, J. C., Gardiner, B. G. and Shanklin, J. D.: Large losses of total ozone in Antarctica reveal seasonal ClO_x/NO_x interaction. *Nature*, **315**, 207–210, 1985.

Fortuin, J. P. F. and Kelder, H.: An ozone climatology based on ozone sonde and satellite measurements. *J. Geophys. Res.*, **103**, D24, 31 709–31 734, 1998.

Gao, R. S., Richard, E. C., Popp, P. J., Toon, G. C., Hurst, D. F., Newman, P. A., Holecek, J. C., Northway, M. J., Fahey, D. W., Danilin, M. Y., Sen, B., Aikin, K., Romashkin, P. A., Elkins, J. W., Webster, C. R., Schauffler, S. M., Greenblatt, J. B., McElroy, C. T., Lait, L. R., Bui, T. P. and Baumgardner, D.: Observational evidence for the role of denitrification in Arctic stratospheric ozone loss. *Geophys. Res. Lett.*, **28**, 15, 2879–2882, 2001.

Goldsmith, P. F.: *Quasi-Optical Systems. Gaussian Beam Quasioptical Propagation and Applications*. IEEE Press/Chapman & Hall Publishers, New York, 1998.

Grant, W. B., Browell, E. V., Butler, C. F., Gibson, S. C., Koi, S. A. and von der Gathen, P.: Use of ozone distributions, potential vorticity and cooling rates to estimate Arctic polar vortex ozone loss during the winter of 1999/2000. *J. Geophys. Res.*, **107**, 2002.

Hanson, D. and Mauersberger, K.: Laboratory studies of the nitric acid trihydrate: Implications for the south polar stratosphere. *Geophys. Res. Lett.*, **15**, 853–858, 1988.

Harris, N. R. P., Rex, M., Goutail, F., Knudsen, B. M., Manney, G. L., Müller, R. and von der Gathen, P.: Comparison of empirically derived ozone losses in the Arctic Vortex. *J. Geophys. Res.*, **107**, accepted, 2002.

Holton, J. R.: *An Introduction to Dynamic Meteorology*. Third edition, Academic Press, San Diego, 1992.

Holton, J. R., Haynes, P. H., McIntyre, M. E., Douglass, A. R., Rood, R. B. and Pfister, L.: Stratosphere-troposphere exchange. *Rev. Geophys.*, **33**, 403–439, 1995.

Hoock, M.: *Aufbau und Betrieb eines bodengebundenen 110 GHz Mikrowellenradiometers zur Beobachtung stratosphärischen Ozons über Bremen*. Master's thesis, Universität Bremen, 2000.

Hoogen, R., Rozanov, V. V. and Burrows, J. P.: Ozone profiles from GOME satellite data: Algorithm description and first validation. *J. Geophys. Res.*, **104**, D7, 8263–8280, 1999.

Hoppel, K. W., Bevilacqua, R. M., Nedoluha, G., Deniel, C., Lefèvre, F., Lumpe, J., Fromm, M., Randall, C., Rosenfield, J. and Rex, M.: POAM III observations of Arctic ozone loss for the 1999/2000 winter. *J. Geophys. Res.*, **107**, accepted, 2002.

Humlicek, J.: An efficient method for evaluation of the complex probability function: the Voigt function and its derivatives. *J. Quant. Spec. Rad. Trans.*, **21**, 309–313, 1979.

Janssen, M. A.: *Atmospheric Remote Sensing by Microwave Radiometry*. John Wiley & Sons, Inc., New York, 1993.

Jones, A. E. and Shanklin, J. D.: Continued decline of total ozone over Halley, Antarctica, since 1985. *Nature*, **376**, 409–411, 1995.

Klein, U.: *Aufbau und Betrieb eines breitbandigen, bodengestützten Millimeterwellen-Radiometers zur Messung atmosphärischer Spurenstoffe*. Ph.D. thesis, Universität Bremen, Verlag Shaker, 1993.

Klein, U., Lindner, K., Wohltmann, I. and Künzi, K. F.: Winter and spring observations of stratospheric chlorine monoxide from Ny-Ålesund, Spitsbergen, in the 1997/98 and 1998/99 winters. *Geophys. Res. Lett.*, **27**, 24, 4093–4097, 2000.

Klein, U., Wohltmann, I., Lindner, K. and Künzi, K. F.: Ozone depletion and chlorine activation in the Arctic winter 1999/2000 observed in Ny-Ålesund. *J. Geophys. Res.*, **107**, accepted, 2002.

Kleinböhl, A., Bremer, H., von König, M., Küllmann, H., Künzi, K. F., Goede, A. P. H., Browell, E. V., Grant, W. B., Toon, G. C., Blumenstock, T., Galle, B., Sinnhuber, B.-M. and Davies, S.: Vortexwide denitrification of the arctic polar stratosphere in winter 1999/2000 determined by remote observations. *J. Geophys. Res.*, **107**, accepted, 2002.

Komhyr, W. D., Barnes, R. A., Brothers, G. B., Lathrop, J. A. and Oppermann, D. P.: Electrochemical concentration cell ozonesonde performance during STOIC 1989. *J. Geophys. Res.*, **100**, D5, 9231–9244, 1995.

von König, M.: *Chloraktivierung und PSC-Bildung in der arktischen Stratosphäre*, volume 5 of *Berichte aus dem Institut für Umweltphysik*. Ph.D. thesis, Universität Bremen, Logos Verlag, 2001.

von König, M., Bremer, H., Eyring, V., Goede, A. P. H., Hetzheim, H., Kleipool, Q. L., Küllmann, H. and Künzi, K. F.: An airborne submm radiometer for

the observation of stratospheric trace gases. *Microw. Radiomet. Remote Sens. Earth's Surface*, 409–415, 2000.

Koop, T., Carslaw, K. S. and Peter, T.: Thermodynamic stability and phase transitions of PSC particles. *Geophys. Res. Lett.*, **24**, 17, 2199–2202, 1997.

Kopp, G., Berg, H., Blumenstock, T., Fischer, H., Hase, F., Hochschild, G., Höpfner, M., Kouker, W., Reddmann, T., Ruhnke, R., Raffalski, U. and Kondo, Y.: Evolution of ozone and ozone related species over Kiruna during the THESEO 2000–SOLVE campaign retrieved from ground-based millimeter wave and infrared observations. *J. Geophys. Res.*, **107**, in review, 2002.

Kuntz, M.: A new implementation of the Humlicek algorithm for the calculation of the Voigt profile. *J. Quant. Spec. Rad. Trans.*, **57**, 6, 819–824, 1997.

Lait, L. R., Schoeberl, M. R., Newman, P. A., McGee, T. J., Burris, J. F., Browell, E. V., Richard, E. C., Braathen, G. O., Bojkov, B. R., Goutail, F., von der Gathen, P., Kyrö, E., Vaughan, G., Kelder, H., Kirkwood, S., Woods, P., Dorokhov, V., Zaitcev, I., Litynska, Z., Kois, B., Benesova, A., Skrivankova, P., Backer, H. D., Davies, J., Jorgensen, T. and Mikkelsen, I. S.: Ozone loss from quasi-conservative coordinate mapping during the 1999–2000 SOLVE/THESEO 2000 campaign. *J. Geophys. Res.*, **107**, accepted, 2002.

Langer, J.: *Charakterisierung eines Radiometers für atmosphärenphysikalische Messungen*. Master's thesis, Universität Bremen, 1995.

Langer, J.: *Ozonmessungen in der Stratosphäre von Spitzbergen*, volume 322 of *Berichte zur Polarforschung*. Ph.D. thesis, Universität Bremen, Alfred-Wegener-Institut für Polar- und Meeresforschung, 1999.

Langer, J., Barry, B., Klein, U., Sinnhuber, B.-M., Wohltmann, I. and Künzi, K. F.: Chemical ozone depletion during Arctic winter 1997/98 derived from ground based millimeter-wave observations. *Geophys. Res. Lett.*, **26**, 5, 599–602, 1999.

Liebe, H. J.: MPM – An atmospheric millimeter-wave propagation model. *Interntl. J. Infrared & Millimeter Waves*, **10**, 6, 1989.

Liebe, H. J. and Dillon, T. A.: Accurate foreign-gas-broadening parameters of the 22-GHz H_2O line from refraction spectroscopy. *J. Chem. Phys.*, **50**, 2, 1969.

Lindner, K.: *Messung von stratosphärischem Wasserdampf und Chlormonoxid in der Arktis: Erweiterung und Optimierung des passiven Mikrowellenradiometers RAM in Ny-Ålesund, Spitzbergen*, volume in press of *Berichte aus dem Institut für Umweltphysik*. Ph.D. thesis, Universität Bremen, Logos Verlag, 2002.

Manney, G. L. and Sabutis, J. L.: Development of the polar vortex in the 1999–2000 Arctic winter stratosphere. *Geophys. Res. Lett.*, **27**, 17, 2589–2592, 2000.

Marshall, J. S. and Palmer, W. M.: The distribution of raindrops with size. *J. Meteor.*, 165–166, 1948.

Molina, J. M. and Rowland, F. S.: Stratospheric sink for chloroflouromethans: Chlorine catalyzed destruction of ozone. *Nature*, **249**, 810–812, 1974.

Molina, L. T. and Molina, M. J.: Production of Cl_2O_2 from the selfreaction of the ClO molecule. *J. Phys. Chem.*, **91**, 433–436, 1987.

Mrowinski, D.: Refraktion und Absorption in atmosphärischen Gasen in der Umgebung der 22 GHz-Wasserdampf-Rotationslinie. *Z. angew. Phys.*, **29**, 5, 1970.

Müller, R., Crutzen, P. J., Grooß, J.-U. and Brühl, C.: Chlorine activation and ozone depletion in the Arctic vortex: Observations by the Halogen Occultation Experiment on the Upper Atmosphere Research Satellite. *J. Geophys. Res.*, **101**, 12 531–12 554, 1996.

Müller, R., Tilmes, S., Grooß, J.-U., McKenna, D. S., Toon, G. C., Stachnik, R. A., Margitan, J. J., Elkins, J. W. and Russell III, J. M.: Chemical ozone loss and chlorine activation deduced from HALOE and OMS measurements in the Arctic winter 1999–2000. *J. Geophys. Res.*, **107**, in review, 2002.

Nash, E. R., Newman, P. A., Rosenfield, J. E. and Schoeberl, M. R.: An objective determination of the polar vortex using Ertel's potential vorticity. *J. Geophys. Res.*, **101**, D5, 9471–9478, 1996.

Nedoluha, G., Bevilacqua, R. M., Gomez, R. M., Thacker, D. L., Waltman, W. B. and Pauls, T. A.: Ground-based measurements of water vapor in the middle atmosphere. *J. Geophys. Res.*, **100**, D2, 2927–2939, 1995.

Newman, P. A., Gleason, J. F., McPeters, R. D. and Stolarski, R. S.: Anomalously low ozone over the Arctic. *Geophys. Res. Lett.*, **24**, 22, 2689–2692, 1997.

Newman, P. A., Harris, N. R. P., Adriani, A., Amanatidis, G. T., Anderson, J. G., Braathen, G. O., Brune, W. H., Carslaw, K. S., Craig, M. S., DeCola, P. L., Guirlet, M., Hipskind, R. S., Kurylo, M. J., Küllmann, H., Larsen, N., Mégie, G. J., Pommereau, J.-P., Poole, L. R., Schoeberl, M. R., Stroh, F., Toon, O. B., Trepte, C. R. and van Roozendael, M.: An overview of the SOLVE-THESEO 2000 campaign. *J. Geophys. Res.*, **107**, accepted, 2002.

Newman, P. A., Nash, E. R. and Rosenfield, J. E.: What controls the temperature of the Arctic stratosphere during the spring? *J. Geophys. Res.*, **106**, D17, 19 999–20 010, 2001.

Parrish, A., de Zafra, R. L., Solomon, P. M. and Barrett, J. W.: A ground based technique for millimeter wave spectroscopic observations of stratospheric trace constituents. *Radio Sci.*, **23**, 2, 106–118, 1988.

Pawson, S. and Naujokat, B.: The cold winters of the middle 1990s in the northern lower stratosphere. *J. Geophys. Res.*, **104**, D12, 14 209–14 222, 1999.

Peter, R.: Stratospheric and mesopheric latitudinal water vapor distributions obtained by an airborne millimeter-wave spectrometer. *J. Geophys. Res.*, **103**, D13, 16 275–16 290, 1998.

Pickett, H. M.: Effects of velocity averaging on the shapes of absorption lines. *J. Chem. Phys.*, **73**, 12, 6090–6094, 1980.

Plumb, R. A., Waugh, D. W. and Chipperfield, M. P.: The effects of mixing on tracer relationsships in the polar vortices. *J. Geophys. Res.*, **105**, D8, 10 047–10 062, 2000.

Popp, P. J., Northway, M. J., Holecek, J. C., Gao, R. S., Fahey, D. W., Elkins, J. W., Hurst, D. F., Romashkin, P. A., Toon, G. C., Sen, B., Schauffler, S. M., Salawitch, R. J., Webster, C. R., Herman, R. L., Jost, H., Bui, T. P., Newman, P. A. and Lait, L. R.: Severe and extensive denitrification in the 1999–2000 Arctic winter stratosphere. *Geophys. Res. Lett.*, **28**, 15, 2875–2878, 2001.

Raffalski, U.: *Messung stratosphärischer Spurengase über Ny-Ålesund, Spitzbergen, mit Hilfe eines bodengebundenen Mikrowellenradiometers*, volume 278 of *Berichte zur Polarforschung*. Ph.D. thesis, Universität Bremen, Alfred-Wegener-Institut für Polar- und Meeresforschung, 1998.

Raffalski, U., Klein, U., Franke, B., Langer, J., Sinnhuber, B.-M., Trentmann, J., Künzi, K. F. and Schrems, O.: Ground based millimeter-wave observations of Arctic chlorine activation during winter and spring 1996/97. *Geophys. Res. Lett.*, **25**, 17, 3331–3334, 1998.

Randel, W. J., Wu, F., Russell III, J. M., Roche, A. and Waters, J. W.: Seasonal cycles and QBO variations in stratospheric CH_4 and H_2O observed in UARS HALOE data. *J. Atmos. Sci.*, **55**, 163–185, 1998.

Ray, E. A., Moore, F. L., Elkins, J. W., Hurst, D. F., Romanshkin, P. A., Dutton, G. S. and Fahey, D. W.: Descent and mixing in the 1999–2000 northern

polar vortex inferred from in situ tracer measurements. *J. Geophys. Res.*, **107**, submitted, 2002.

Rex, M., von der Gathen, P., Braathen, G. O., Harris, N. R. P., Reimer, E., Beck, A., Alfier, R., Krüger-Carstensen, R., Chipperfield, M. P., Backer, H. D., Balis, D., O'Connor, F., Dier, H., Dorokhov, V., Fast, H., Gamma, A., Gil, M., Kyrö, E., Litynska, Z., Mikkelsen, I. S., Molyneux, M. J., Murphy, G., Reid, S. J., Rummukainen, M. and Zeferos, C.: Chemical ozone loss in the Arctic winter 1994/95 as determined by the Match technique. *J. Atm. Chem.*, **32**, 1, 35–39, 1999.

Rex, M., Harris, N. R. P., von der Gathen, P., Lehmann, R., Braathen, G. O., Reimer, E., Beck, A., Chipperfield, M. P., Alfier, R., Allaart, M., O'Connor, F., Dier, H., Dorokhov, V., Fast, H., Gil, M., Kyrö, E., Litynska, Z., Mikkelsen, I. S., Molyneux, M. J., Nakane, H., Notholt, J., Rummukainen, M., Viatte, P. and Wenger, J.: Prolonged stratospheric ozone loss in the 1995/96 Arctic winter. *Nature*, **389**, 835–838, 1997.

Rex, M., Salawitch, R. J., Harris, N. R. P., von der Gathen, P., Braathen, G. O., Schulz, A., Deckelmann, H., Chipperfield, M. P., Sinnhuber, B.-M., Reimer, E., Alfier, R., Bevilacqua, R. M., Hoppel, K. W., Fromm, M., Lumpe, J., Küllmann, H., Kleinböhl, A., Bremer, H., von König, M., Künzi, K. F., Toohey, D., Vömel, H., Richard, E. C., Aikin, K., Jost, H., Greenblatt, J. B. et al.: Chemical depletion of Arctic ozone in winter 1999/2000. *J. Geophys. Res.*, **107**, accepted, 2002.

Richard, E. C., Aikin, K., Andrews, A. E., Daube, B. C., Jr., Gerbig, C., Wofsy, S. C., Romashkin, P. A., Hurst, D. F., Ray, E. A., Moore, F. L., Elkins, J. W., Deshler, T. and Toon, G. C.: Severe chemical ozone loss inside the Arctic polar vortex during winter 1999–2000 inferred from in situ airborne measurements. *Geophys. Res. Lett.*, **28**, 11, 2197–2200, 2001.

Robinson, A., Cahill, G. A., Danis, F., Guirlet, M., Harris, N. R. P., Lee, A. M., McIntyre, J. D., Pyle, J. A., Garcelon, S., Hansford, G. M., Jones, R. L., Nilsson, H., Kirkwood, S., Arvelius, J., Dagnesjö, S., Toohey, D. W., Deshler, T., Gardiner, T., Howieson, I., Woods, P., Pommereau, J.-P. and Goutail, F.: Ozone loss derived from balloon-borne tracer measurements and the SLIMCAT CTM. *J. Geophys. Res.*, **107**, in review, 2002.

Rodgers, C. D.: *Inverse Methods for Atmospheric Sounding*. First edition, World Scientific Publishing Co. Pte. Ltd., Singapore, 2000.

Roedel, W.: *Physik unserer Umwelt: Die Atmosphäre*. Second edition, Springer Verlag, Heidelberg, 1994.

Salawitch, R. J., Margitan, J. J., Sen, B., Toon, G. C., Osterman, G. B., Rex, M., Elkins, J. W., Ray, E. A., Moore, F. L., Hurst, D. F., Romashkin, P. A., Bevilacqua, R. M., Hoppel, K. W., Richard, E. C. and Bui, T. P.: Chemical loss of ozone during the Arctic winter of 1999–2000: An analysis based on balloon-borne observations. *J. Geophys. Res.*, **107**, accepted, 2002.

Santee, M. L., Manney, G. L., Livesey, N. J. and Waters, J. W.: UARS microwave limb sounder observations of denitrification and ozone loss in the 2000 Arctic late winter. *Geophys. Res. Lett.*, **27**, 19, 3213–3216, 2000.

Schoeberl, M. R., Newman, P. A., Lait, L. R., McGee, T. J., Burris, J. F., Browell, E. V., Grant, W. B., Richard, E. C., von der Gathen, P., Bevilacqua, R. M., Mikkelsen, I. S. and Molyneux, M. J.: An assessment of the ozone loss during the 1999–2000 SOLVE/THESEO 2000 Arctic campaign. *J. Geophys. Res.*, **107**, accepted, 2002.

Shindell, D. T., Rind, D. and Lonergan, P.: Increased polar stratospheric ozone losses and delayed eventual recovery owing to increased greenhouse-gas concentrations. *Nature*, **392**, 589–592, 1998.

Shine, K. P.: The middle atmosphere in the absence of dynamical heat fluxes. *Quart. J. Roy. Met. Soc.*, **113**, 603–633, 1987.

Shine, K. P.: On the cause of the relative greenhouse strength of gases such as the halocarbons. *J. Atmos. Sci.*, **48**, 1513–1518, 1991.

Sinnhuber, B.-M.: *Bestimmung stratosphärischer Ozonprofile aus Spektren eines bodengebundenen Mikrowellen-Radiometers*. Master's thesis, Universität Bremen, 1995.

Sinnhuber, B.-M.: *Variabilität der arktischen Ozonschicht: Analyse und Interpretation bodengebundener Millimeterwellenmessungen*, volume 309 of *Berichte zur Polarforschung*. Ph.D. thesis, Universität Bremen, Alfred-Wegener-Institut für Polar- und Meeresforschung, 1999.

Sinnhuber, B.-M., Chipperfield, M. P., Davies, S., Burrows, J. P., Eichmann, K.-U., Weber, M., von der Gathen, P., Guirlet, M., Cahill, G. A., Lee, A. M. and Pyle, J. A.: Large loss of total ozone during the Arctic winter of 1999/2000. *Geophys. Res. Lett.*, **27**, 21, 3473–3476, 2000.

Sinnhuber, B.-M., Langer, J., Klein, U., Raffalski, U., Künzi, K. F. and Schrems, O.: Ground based millimeter-wave observations of Arctic ozone depletion during winter and spring of 1996/97. *Geophys. Res. Lett.*, **25**, 17, 3227–3330, 1998.

Sinnhuber, B.-M., Müller, R., Langer, J., Bovensmann, H., Eyring, V., Klein, U., Trentmann, J., Burrows, J. P. and Künzi, K. F.: Interpretation of mid-stratospheric Arctic ozone measurements using a photochemical box-model. *J. Atm. Chem.*, **34**, 281–290, 1999.

Sobel, A. H., Plumb, R. A. and Waugh, D. W.: On methods of calculating transport across the polar vortex edge. *J. Atmos. Sci.*, **54**, 2241–2260, 1997.

Solomon, S.: Stratospheric ozone depletion: A review of concepts and history. *Rev. Geophys.*, **37**, 3, 275–316, 1999.

Solomon, S., Garcia, R. R., Rowland, F. S. and Wuebbles, D. J.: On the depletion of Antarctic ozone. *Nature*, **321**, 755–758, 1986.

Stolarski, R. S. and Cicerone, R. J.: Stratospheric chlorine: A possible sink for ozone. *Can. J. Chem.*, **52**, 1610–1615, 1974.

Swartz, W. H., Yee, J.-H., Vervack, R. J., Jr., Lloyd, S. A. and Newman, P. A.: Photochemical ozone loss in the Arctic as determined by MSX/UVISI stellar occultation observations during the 1999–2000 winter. *J. Geophys. Res.*, **107**, accepted, 2002.

Tabazadeh, A., Santee, M. L., Danilin, M. Y., Pumphrey, H. C., Newman, P. A., Hamill, P. J. and Mergenthaler, J. L.: Quantifying denitrification and its effect on ozone recovery. *Science*, **288**, 1407–1411, 2000.

Toon, G. C.: The JPL MkIV Interferometer. *Opt. Photonics News*, **2**, 19–21, 1991.

Townes, C. H. and Schawlow, A. L.: *Microwave Spectroscopy*. Dover Publications, Inc., New York, 1975.

Tuckermann, R.: *Aufbau eines bodengebundenen Mikrowellenradiometers zur Untersuchung stratosphärischen Ozons*. Master's thesis, Universität Bonn, 1997.

Ulaby, F. T., Moore, R. K. and Fung, A. K.: *Microwave Remote Sensing: Active and Passive. Volume 1: Microwave Remote Sensing Fundamentals and Radiometry*. Artech House, Inc., Norwood, 1981.

Ulaby, F. T., Moore, R. K. and Fung, A. K.: *Microwave Remote Sensing: Active and Passive. Volume 2: Radar Remote Sensing and Surface Scattering and Emission Theory*. Artech House, Inc., Norwood, 1982.

Ulaby, F. T., Moore, R. K. and Fung, A. K.: *Microwave Remote Sensing: Active and Passive. Volume 3: From Theory to Applications*. Artech House, Inc., Norwood, 1986.

van Vleck, J. H. and Weisskopf, V. F.: On the shape of collision-broadened lines. *Revs. Mod. Phys.*, **17**, 227–236, 1945.

Wayne, R. P.: *Chemistry Of The Atmosphere*. Second edition, Clarendon Press, Oxford, 1991.

Webster, C. R., May, R. D., Toohey, D. W., Avallone, L. M., Anderson, J. G., Newman, P. A., Lait, L. R., Schoeberl, M. R., Elkins, J. W. and Chan, K. R.: Chlorine chemistry on polar stratospheric cloud particles in the Arctic winter. *Science*, **261**, 1130–1133, 1993.

WMO: *Scientific assessment of ozone depletion*. Report 44, World Meteorological Organization, 1999.

Wofsy, S. C., McElroy, M. B. and Yung, Y. L.: The chemistry of atmospheric bromine. *Geophys. Res. Lett.*, **2**, 215–218, 1975.

Wohltmann, I.: *Auswertung von Spektren des Mikrowellenradiometers RAM: Homogenisierung eines mehrjährigen Datensatzes und Erstellung von Ozonprofilen*. Master's thesis, Universität Bremen, 1999.

Woyke, T., Müller, R., Stroh, F., McKenna, D. S., Engel, A., Margitan, J. J., Rex, M. and Carslaw, K. S.: A test of our understanding of the ozone chemistry in the Arctic polar vortex based on in situ measurements of ClO, BrO and O_3 in the 1994/1995 winter. *J. Geophys. Res.*, **104**, D15, 18 755–18 768, 1999.

Wu, J. and Dessler, A. E.: Comparisons between measurements and models of Antarctic ozone loss. *J. Geophys. Res.*, **106**, D3, 3195–3201, 2001.

de Zafra, R. L., Jaramillo, M., Barrett, J. W., Emmons, L. K., Solomon, P. M. and Parrish, A.: New observations of large concentrations of ClO in the springtime lower stratosphere over Antarctica and its implications for ozone-depleting chemistry. *J. Geophys. Res.*, **94**, 11 423–11 428, 1989.

List of Tables

List of Figures